Field Line Resonance in Two and a Half Dimensions

DRAFT VERSION CREATED ON APRIL 25, 2016

Acknowledgements

TODO: · · ·

Abstract

Field line resonances — that is, Alfvén waves bouncing between the northern and southern foot points of a geomagnetic field line — serve to energize magnetospheric particles through drift-resonant interactions, carry energy from high to low altitude, induce currents in the magnetosphere, and accelerate particles into the atmosphere. Wave structure and polarization significantly impact the execution these roles. The present work showcases a new two and a half dimensional code, Tuna, ideally suited to model FLRs, with the ability to consider large-but-finite azimuthal modenumbers, coupling between the poloidal, toroidal, and compressional modes, and arbitrary harmonic structure. Using Tuna, the interplay between Joule dissipation and poloidal-to-toroidal rotation is considered for both dayside and nightside conditions. An attempt is also made to demystify giant pulsations, a class of FLR knows for its distinctive ground signatures. Numerical results are supplemented by a survey of $\sim$500 FLRs using data from the Van Allen Probes, the first such survey to characterize each event by both polarization and harmonic. The combination of numerical and observational results suggests an explanation for the disparate distributions observed in poloidal and toroidal FLR events.

Contents

List of Tables

List of Figures

Chapter 1

Introduction

1859 was a pivotal year in human history. The United States moved steadily toward the American Civil War, which would abolish slavery and consolidate the power of the federal government. A slew of conflicts in Southern Europe set the stage for the unification of Italy. The Taiping Civil War — one of the bloodiest conflicts of all time — is considered by many to mark the beginning of modern Chinese history. Origin of Species was published. The first transatlantic telegraph cable was laid.

Meanwhile, ambivalent to humanity, the Sun belched an intense burst of charged particles and magnetic energy directly toward Earth. The resulting geomagnetic storm[1] caused telegraph systems to fail across the Western hemisphere, electrocuting operators and starting fires[35, 94]. Displays of the northern lights were visible as far south as Cuba.

The Solar Storm of 1859 was perhaps the most powerful in recorded history, but by no means was it a one-time event. The Sun discharges hundreds of coronal mass ejections (CMEs) per year, of all sizes, in all directions. In fact, a comparably large CME narrowly missed Earth in 2012[70]. Had it not, it's estimated it would have caused widespread, long-term electrical outages, with a damage toll on the order of 10^{12} dollars[66].

[1] The Solar Storm of 1859 is also called the Carrington Event, after English astronomer Richard Carrington. He drew a connection between the storm's geomagnetic activity and the sunspots he had observed the day before.

The Sun's extreme — and temperamental — effect on Earth's magnetic environment makes a compelling case for the ongoing study of space weather. Such research has evolved over the past century from sunspot counts and compass readings to multi-satellite missions and supercomputer simulations. Modern methods have dramatically increased humanity's understanding of the relationship between the Sun and the Earth; however, significant uncertainty continues to surround geomagnetic storms, substorms, and the various energy transport mechanisms that make them up.

The present work focuses in particular on the phenomenon of field line resonance: Alfvén waves bouncing between the northern and southern hemispheres. Such waves play an important part in the energization of magnetospheric particles, the transport of energy from high to low altitude, the precipitation of particles into the atmosphere, and the driving of currents at the top of the atmosphere. It is these currents which give rise to potentially-catastrophic magnetic disturbances at Earth's surface.

The study of resonance in the near-Earth environment is furthermore valuable as a proxy for other (less-accessible) plasma environments. Similar waves occur in astrophysical plasmas, observation of which is limited by distance. Field line resonance is also analogous to the so-called "fishbone instability" in fusion reactors. As a plasma laboratory, the magnetosphere is unique in that it is both close enough to measure directly, and also large enough that measurements can be performed without disrupting its behavior.

1.1 Structure of the Present Work

The present work is laid out as follows.

Chapter 2 surveys the near-Earth environment. Prominent features of the magnetosphere are defined. The behavior of the magnetosphere during geomagnetic storms and substorms is summarized.

Chapter 3 introduces the field line resonance phenomenon, in terms of both the underlying physics and notable work on the topic. Jargon is introduced to clarify important elements of wave structure. Several open questions about field line resonances (FLRs) are offered as motivations for the present work.

Chapter 4 lays the groundwork for a numerical model by exploring the fundamental equations of waves in a cold, resistive plasma — such as Earth's magnetosphere. Characteristic scales are gleaned from the resulting dispersion relations.

Chapter 5 presents Tuna, a new two and a half dimensional simulation designed specifically for the realistic modeling of FLRs. Tuna's non-orthogonal geometry, height-resolved ionosphere, novel driving mechanism, and coupling to the atmosphere are justified and explained.

Chapter 6 considers the addition of electron inertial effects to Tuna, which are neglected in the core model presented in Chapter 5. These effects allow the computation of parallel currents and electric fields, which have not previously been included in global Alfvén models. The effects are shown to be instability-prone and computationally expensive, but some results are gleaned nonetheless.

Chapter 7 showcases the core numerical results of the present work, unifying several of the questions posed in Chapter 3. The interplay between compressional propagation, poloidal-to-toroidal rotation, and Joule dissipation is considered from several angles.

Chapter 8 puts the numerical results in context through the analysis of data from the Van Allen Probes mission. FLR occurrence rates are considered in terms of location, harmonic, and polarization, parameters which have been only partially addressed in past FLR surveys.

Chapter 9 briefly summarizes the results shown in the above chapters — code development, analysis of numerical results, and satellite observation — and suggests further directions.

Chapter 2

The Near-Earth Environment

From Earth's surface to a height of a hundred kilometers or so, the atmosphere is a well-behaved fluid: a collisional ensemble of neutral atoms. Higher up, its behavior changes dramatically. As altitude increases, solar ultraviolet radiation becomes more intense, which ionizes atmospheric atoms and molecules. Density also decreases, slowing collisional recombination. Whereas the neutral atmosphere is held against Earth's surface by gravity, the motion of charged particles is dominated by Earth's geomagnetic field, as well as the electromagnetic disturbances created as that field is hammered by the solar wind.

Before discussing specific interactions, it's appropriate to introduce the so-called "frozen-in condition." In a collisionless plasma, magnetic field lines are equiputential contours. Charged particles move freely along the contours, but cannot move across them. Compression of the magnetic field is synonymous with compression of the ambient plasma, as any magnetic field lines that thread a moving plasma are dragged along with it. This assumption is valid throughout most of the magnetosphere — that is, the region of space primarily governed by Earth's magnetic field — and provides an invaluable tool for understanding the large-scale motions of plasmas and fields.

2.1 The Outer Magnetosphere

Plasma behavior within Earth's magnetosphere is ultimately driven by the solar wind: a hot ($\sim$100 eV), fast-moving ($\sim$100 km/s) plasma threaded by the interplanetary magnetic field ($\sim$10 nT)[1]. The density of the solar wind is on the order of $10\,/\mathrm{cm}^3$; in a laboratory setting, this would constitute an ultra-high vacuum (atmospheric density at sea level is $\sim 10^{19}\,/\mathrm{cm}^3$), but compared to much of the magnetopause it's quite dense.

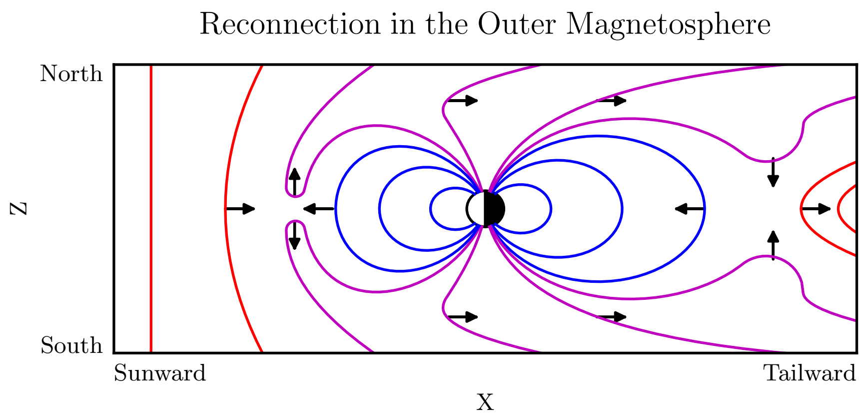

Figure 2.1: When the solar wind magnetic field (red) points southward, reconnection can occur between it and Earth's (northward) closed magnetic field lines (blue). The resulting open field lines (magenta) convect nightward over the poles, ultimately arriving in the magnetotail. There, the open field lines reconnect again. Newly closed field lines move Earthward, carrying flux across the flanks and back to the dayside. The rest are completely decoupled from Earth, and are lost to the solar wind.

The magnetosphere's outer boundary represents a balance between the solar wind dynamic pressure and the magnetic pressure of Earth's dipole field. On the dayside, the dipole is compressed, pushing this boundary to within about $10\,\mathrm{R_E}$ of Earth[2]. The nightside magnetosphere is stretched into a long tail which may exceed $50\,\mathrm{R_E}$ in width and $100\,\mathrm{R_E}$ in length.

When the interplanetary magnetic field opposes the geomagnetic field at the nose of the magnetosphere, magnetic reconnection occurs. Closed magnetospheric field lines

[1] Listed values correspond to the solar wind at Earth's orbit.

[2] Distances in the magnetosphere are typically measured in units of Earth radii: $1\,\mathrm{R_E} \equiv 6378\,\mathrm{km}$.

"break," opening up to the interplanetary magnetic field[3]. They then move tailward across the poles, dragging their frozen-in plasma with them. Reconnection in the tail allows magnetic field lines to convect back to the day side, across the flanks. This process is called the Dungey cycle[21].

Viewed from the north, the Dungey cycle involves a clockwise flow of flux and plasma on the dusk side and a counterclockwise flow on the dusk side. The motion is accompanied by a convection electric field, per Ohm's law in an ideal plasma:

$$\underline{E} + \underline{U} \times \underline{B} = 0 \tag{2.1}$$

Where $\underline{B}$, $\underline{E}$, and $\underline{U}$ are the magnetic field, electric field, and plasma velocity vectors respectively.

Consistent with Ampère's law, the interplanetary magnetic field is separated from the magnetosphere by a current sheet: the magnetopause. On the dayside, the magnetopause current flows duskward; on the nightside, it flows dawnward around the magnetotail.

Earth's dipole is significantly deformed in the magnetotail; field lines in the northern lobe of the tail points more or less Earthward, and vice versa. Plasma within the lobes is cool ($\sim$100 eV) and rarefied ($\sim 10^{-2}\,/\mathrm{cm}^3$). The two lobes are divided by the plasma sheet, which is comparably hot ($\sim 10^3$ eV) and dense ($\sim 1\,/\mathrm{cm}^3$). The plasma sheet carries a duskward current which connects to the magnetopause current.

[3] Closed field lines are more or less dipolar; one end connects to the north pole of Earth's magnetic core, and the other end to the south pole. Open field lines are tethered to Earth at one end. In principle, the other end eventually doubles back to Earth, but for practical purposes it is lost to the solar wind. The distinction is important because charged particle motion is guided by magnetic field lines, as discussed in Chapter 3.

2.2 The Inner Magnetosphere

Within $L \sim 8$ (where L is the McIlwain parameter[4]), the dipole magnetic field is not appreciably deformed by the solar wind. As a result, the structures in the inner magnetosphere follow closely from the motion of charged particles in an ideal dipole field.

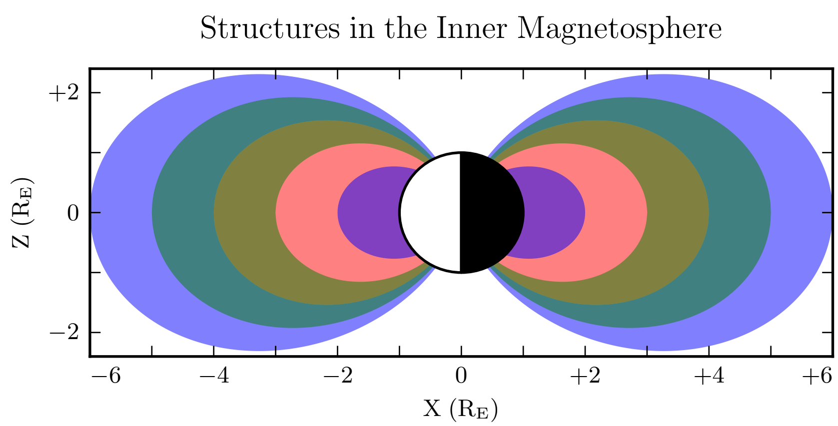

Figure 2.2: The above figure shows typical ranges in L for the plasmasphere (red, $L < 4$), ring current (green, $3 < L < 5$) and radiation belts (blue, $L < 2$ and $4 < L < 6$). These values, particularly the size of the plasmasphere, can vary significantly in response to geomagnetic activity.

The plasmasphere — a cold ($\sim$1 eV), dense ($10^2\,/\mathrm{cm}^3$ to $10^4\,/\mathrm{cm}^3$) torus of corotating plasma — is formed by the outward drift of atmospheric ions along magnetic closed field lines. Its outer boundary is thought to represent a balance between the corotation electric field (per the rotation of Earth's magnetic dipole) and the convection electric field (associated with the convection of magnetic flux during the Dungey cycle). Particle density drops sharply at the edge of the plasmasphere; the boundary is called the plasmapause. The plasmapause typically falls around $L = 4$, though during prolonged quiet times it can extend to $L = 6$ or larger.

[4] The McIlwain parameter L is used to index field lines in Earth's dipole geometry: $L \equiv \frac{r}{\sin^2\theta}$ for colatitude θ and radius r in Earth radii. For example, the $L = 5$ field line passes through the equatorial plane at a geocentric radius of $5\,\mathrm{R_E}$, then meets the Earth at a colatitude of $\arcsin\sqrt{\frac{1}{5}} \sim 27°$ (equally, a latitude of $\arccos\sqrt{\frac{1}{5}} \sim 63°$).

Energetic particles trapped within the inner magnetosphere are divided into two populations.

The Van Allen radiation belts are made up of particles with energy above 10^5 eV or so. The inner belt ($L \lesssim 2$) is primarily composed of protons, the decay remnants of neutrons freed from the atmosphere by cosmic rays. The outer belt ($L \gtrsim 4$) is primarily composed of high-energy electrons. The density of radiation belt particles is significantly affected by geomagnetic storms and substorms; a typical value is $10\,/\mathrm{cm}^3$.

Particles with energies of 10^3 eV to 10^5 eV make up the ring current, which extends from $L \sim 3$ to $L \sim 5$. Gradient-curvature drift carries ions and electrons in opposite directions; the net result is a westward current. During quiet times, the ring current causes magnetic a southward magnetic field on the order of 1 nT at Earth's equator, while during geomagnetically active times (discussed in Section 2.4) the effect may be 100 nT or more[5].

2.3 The Ionosphere

Earth's neutral atmosphere is an excellent insulator. Collisions are so frequent that charged particles quickly thermalize and recombine. The breakdown of air molecules into a conductive plasma (as happens during a lightning strike, for example) requires electric fields on the order of 10^9 mV/m.

Cold particles in the magnetosphere are likewise not conducive to currents. In the absence of collisions, electrons and ions drift alongside one another in response to an electric field, creating no net current perpendicular to the magnetic field[6]. Magnetic field lines can typically be considered as equipotential contours, devoid of field-aligned potential structures.

The ionosphere is a sweet spot between the two regimes. Collisions are frequent enough to disrupt the drift of ions, but not frequent enough to immobilize the electrons. The

[5] For comparison, Earth's dipole field points north at the equator with a magnitude over 10^4 nT.

[6] The so-called E-cross-B drift is associated with a velocity of $\underline{U} = \frac{1}{B^2}\underline{E} \times \underline{B}$, independent of a charged particle's mass or sign.

result is a finite-valued conductivity tensor. Pedersen currents (which scale with the Pedersen conductivity) flow in the direction of the perpendicular electric field. Hall currents (due to the Hall conductivity) flow in the $\underline{B} \times \underline{E}$. It is these currents — particularly the Hall current — which give rise to magnetic fields at the ground. Collisions in the ionosphere also result in a finite parallel conductivity, allowing for the formation of potential structures along the magnetic field line.

The convection electric field (associated with the Dungey cycle, Section 2.1) drives Pedersen currents in the ionosphere. Pedersen currents flow dawnward on the flanks and duskward across the poles. The currents remain divergence-free by connecting to field-aligned currents at the edges of the polar cap. The field-aligned currents, in turn, connect to the magnetopause current, the cross-tail current, and the (partial) ring current.

When electron density is low, thermal velocities may be unable to carry enough current to satisfy $\nabla \cdot \underline{J} = 0$. This leads to the formation of potential structures along geomagnetic field lines in the ionosphere. Such structures accelerate particles along magnetic field lines, leading to the precipitation of energetic particles into the atmosphere. As the particles thermalize, they excite atmospheric atoms. The resulting spontaneous emission is often in the visible spectrum, giving rise to the aurora.

2.4 Geomagnetic Storms and Substorms

The quiet geomagnetic behavior described above is periodically disturbed by transient solar phenomena such as corotating interaction regions (CIRs) and coronal mass ejections (CMEs). CMEs, such as the one that caused the Solar Storm of 1859 mentioned in Chapter 1, are bursts of unusually dense solar wind which are ejected from regions of high magnetic activity on the Sun; they are most common at the height of the eleven-year solar cycle. CIRs, on the other hand, occur when a relatively fast region of the solar wind catches up to an earlier and slower-moving pocket of solar wind, resulting in a pair of shockwaves.

During a storm, increased solar wind intensity results in enhanced magnetic reconnection on the dayside. As the newly-opened field lines are swept tailward, the convection electric field is strengthened. The plasmasphere — the outer boundary of which is set by a balance between the convection electric field and the (more or less constant) corotation electric field — sheds its outer layers[33]. A large number of energetic particles are also injected into the ring current[67].

The strength of the storm is gauged by the size of the magnetic perturbation created by the ring current[7]. A small storm has a magnitude of 50 nT to 100 nT. Large storms may reach 250 nT to 500 nT. The Carrington Event, mentioned in Chapter 1, is thought to have exceeded 1700 nT[94].

The main phase of a storm typically lasts for several hours. Storm recovery — the gradual return of the storm index to zero, and the refilling of the plasmasphere — lasts several days. Geomagnetic storms occur tens of times per year at the height of the solar cycle, and just a few times per year otherwise.

Whereas storms are prompted by large solar wind events on the dayside, geomagnetic substorms are primarily a nightside occurrence. As flux accumulates in the tail, magnetic tension builds in the stretched field lines. A substorm is an impulsive release of that tension.

At substorm onset, a burst of reconnection occurs in the tail. A jet of plasma is launched Earthward from the reconnection site (and another is launched tailward, and lost to the solar wind). The Earthward plasma injection injects particles into the ring current. The outer radiation belt is depleted, then repopulated. Energetic particles precipitate into the atmosphere, giving rise to a distinctive sequence of auroral signatures over the course of about an hour.

Concurrent with substorm onset, impulsive Alfvén waves are observed with periods of a minute or two. The precise ordering of events — whether reconnection causes the waves, or vice versa, or if they share a common cause — remains controversial.

[7] The most commonly used storm index is DST, which is computed hourly using measurements from several ground magnetometers near the equator. The Sym-H index, used in Section 5.3, is computed once per minute.

Each substorm lasts several hours, including the time it takes for the ring current to return to pre-substorm levels. Several substorms may occur per day during quiet times. During a storm, substorms become far more frequent; by the time one has ended, another may have already begun.

Chapter 3

Field Line Resonance

The motion of a charged particle in a dipole field can be described in terms of three fundamental motions.

The first is cyclotron motion. Given a uniform magnetic field line, a particle follows a helical path. It moves in a circular path in a plane normal to the magnetic field line, and keeps a constant velocity along the direction of the field. Close to Earth, where the magnetic field is strongest, the proton (electron) cyclotron timescale is on the order of $10^{-3}\,\mathrm{s}$ ($10^{-6}\,\mathrm{s}$); at $L \sim 5$, a typical value is closer to $10\,\mathrm{s}$ ($10^{4}\,\mathrm{s}$).

The second fundamental motion is bounce motion. As it moves along the magnetic field line like a bead on a wire, the particle experiences a change in magnetic field magnitude. In order to conserve its magnetic moment (also called the first adiabatic invariant), the particle's perpendicular kinetic energy increases in proportion with the magnetic field. When the perpendicular kinetic energy can no longer increase — that is, when all of the particle's kinetic energy is perpendicular — the particle bounces back. Particles undergoing bounce motion continuously move back and forth between the northern and southern hemispheres, with timescales of a few seconds to a few minutes.

Particles with more parallel kinetic energy (compared to their perpendicular kinetic energy) bounce at lower altitudes. If the particle's motion is sufficiently field-aligned, the bounce altitude drops into the atmosphere, and the particle is collisionally thermalized. This process is called precipitation.

The third fundamental motion is drift motion. Over the course of a particle's cyclotron motion, the Earthward half of the orbit experiences a slightly stronger magnetic field (and thus a slightly smaller orbit radius). The net effect, called the gradient-curvature drift, is an azimuthal motion around Earth on timescales of $\sim 10^3$ s.

Wave-particle resonance arises when a particle's periodic motion matches with the frequency of a coincident electromagnetic wave[23, 63, 72, 83]. In the particle's rest frame, the wave then appears as a net electric field. This allows a net movement of energy between the wave and the particle. The interaction is analogous to a surfer moving along with — and being accelerated by — a wave in the ocean. Such resonance can arise for any of the three fundamental motions, or even for a combination of them.

In the present work, the waves under consideration are field line resonances (FLRs). An FLR is a standing harmonic on a geomagnetic field line. It can also be envisioned as a superposition of traveling waves, reflecting back and forth between its northern and southern foot points at the conducting ionosphere.

These waves travel at the Alfvén speed, v_A, defined per

$$v_A^2 \equiv \frac{B^2}{\mu_0 \rho} \qquad \text{or, equally,} \qquad v_A^2 \equiv \frac{1}{\mu_0 \epsilon_\perp} \tag{3.1}$$

Where B is the magnetic field magnitude, ρ is the mass density, and μ_0 is the magnetic constant. The perpendicular electric constant $\epsilon_\perp$ is analogous to the electric constant ϵ_0, and arises in cases (such as the magnetosphere) where a dielectric medium exhibits a preferred direction. In the magnetosphere, mass density and magnetic field strength depend strongly on position. As a result, the Alfvén speed varies by several orders of magnitude over the length of a field line. The fundamental equations of field line resonance were presented by Dungey in 1954[20]. Since then, they have remained a topic of active study.

So-called ultra low frequency waves — of which FLRs are a subset — are categorized by morphology. Continuous (long-lived) pulsations are termed Pc, while irregular pulsations are called Pi. Within each are a number of frequency bands; see Table 3.1[44]. In practice, frequency demarcations are not strict, but rather serve as a heuristic for grouping phenomenologically similar waves[41].

Table 3.1: IAGA Magnetic Pulsation Frequency Bands

	Pc1	Pc2	Pc3	Pc4	Pc5	Pi1	Pi2
Period (s)	0.2–5	5–10	10–45	45–150	150–600	1–40	40–150
Frequency (mHz)	200–5000	100–200	22–100	7–22	2–7	25–1000	7–25

FLRs fall into the Pc3, Pc4, and Pc5 ranges. The present work focuses specifically on the Pc4 band: waves with periods of a minute or two. Frequencies in the Pc4 range typically coincide with Alfvén bounce times[1] near the plasmapause: $L \sim 4$ to $L \sim 6$[2, 16, 24, 56][2]. In fact, the large radial gradients in the Alfvén speed near the plasmapause act as an effective potential well, trapping FLRs[15, 49, 53, 54, 62, 86].

In addition to being radially localized, FLRs in the Pc4 frequency band (also called Pc4 pulsations, or just Pc4s) are localized in magnetic local time (MLT[3]). They have also been shown to occur preferrentially on the dayside, during storms or storm recovery[2, 16, 24, 52, 56, 95].

In the inner magnetosphere, the Alfvén frequency — and thus the frequency of FLRs — often coincides with integer or half-integer[4] multiples of particle drift frequencies[17]. The resulting wave-particle interactions can give rise to significant energization and radial diffusion of the particles. In some cases, the waves also include an electric field parallel to the background magnetic field, breaking the assumption that magnetic field

[1]The Alfvén frequency is the inverse of the Alfvén bounce time: $\frac{2\pi}{\omega_A} \equiv \oint \frac{dz}{v_A}$.

[2]Not coincidentally, these are the same L-shells where the Van Allen Probes spend most of their time; see Chapter 8.

[3]Noon points toward the Sun and midnight away from it, with 06:00 and 18:00 at the respective dawn and dusk flanks.

[4]See Section 3.1.

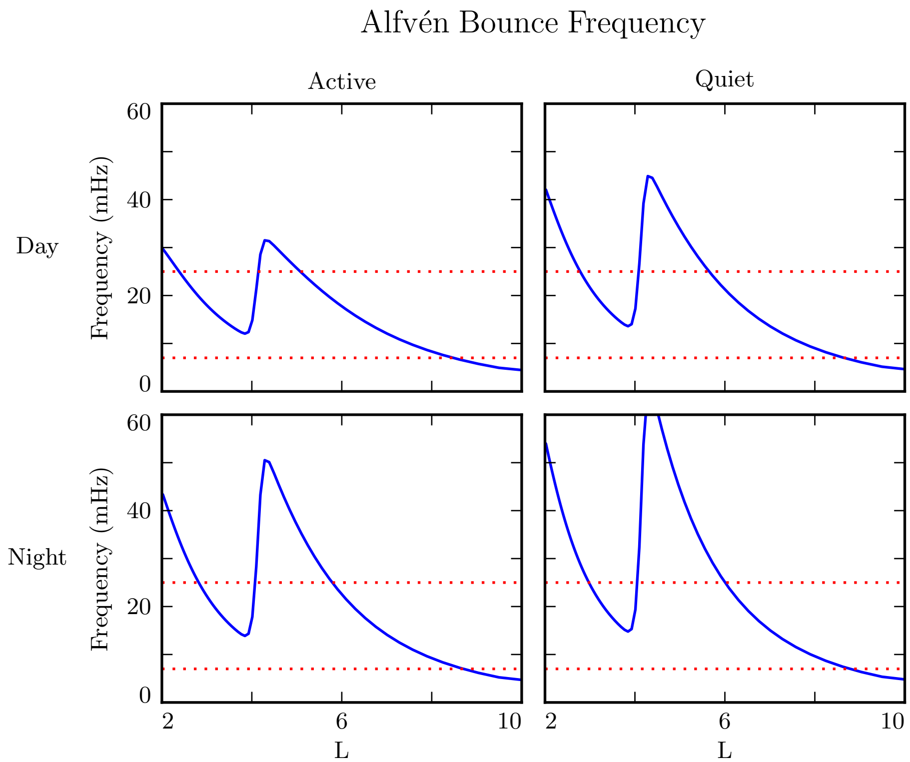

Figure 3.1: The above are bounce frequencies for an Alfvén wave moving back and forth along a geomagnetic field line. Alfvén speeds are computed based on profiles from Kelley[47], as discussed in Section 5.2. Notably, the bounce frequency depends significantly on the position of the plasmasphere, taken here to be at $L = 4$. Dotted lines indicate the Pc4 frequency range: 7 mHz to 25 mHz.

lines are equipotential contours, and contributing to the precipitation of energetic particles into the neutral atmosphere[31, 32, 92, 101].

The present chapter introduces the structural characteristics of FLRs, how those characteristics affect wave behavior, and several unresolved questions related to that behavior.

3.1 Harmonic Structure

Wave structure along a geomagnetic field line is indicated by harmonic number. The first (or fundamental) harmonic has a wavelength twice as long as the field line. The electric field perturbation is zero at the ionospheric foot points of the field line, due to the conductivity of the ionosphere. For the first harmonic, this puts an electric field antinode at the equator, along with a node in the perpendicular[5] perturbation to the magnetic field. For the second harmonic, the electric field has a third node at the equator, in addition to the two at the ionospheric foot points, which is accompanied by an antinode in the perpendicular wave magnetic field. Figure 3.2 shows a qualitative sketch of the first and second harmonics: a series of snapshots in time, in the rest frame of the wave. Perpendicular electric and magnetic field perturbations are shown in blue and red respectively.

A first-harmonic FLR that is periodic or localized in the azimuthal direction is conducive to drift-resonant wave-particle interactions[17, 73]. The particle is like a child on a swing: whenever the path of the particle (or child) gets close to the wave (parent), it gets a push, and always in the same direction. The wave fields spend half its time pointing the other direction, just as the parent must shift their weight backward to get ready for the next push, but at that point the particle (child) is far away.

Second-harmonic FLRs interact with particles through the drift-bounce resonance, which is slightly more complicated. As the particle drifts azimuthally, it also zig-zags north-south. The combination of those two periodic motions must align with the phase of the wave electric field. An example path is shown by the purple line in Figure 3.2: the particle's drift and bounce motions together ensure that it experiences a rightward electric field throughout the wave's oscillation.

The drift and drift-bounce resonance conditions is written, respectively[87]:

$$\omega - m\omega_D = 0 \qquad \text{and} \qquad \omega - m\omega_D = \omega_B \tag{3.2}$$

[5]The parallel, or compressional, wave magnetic field exhibits the same nodes and antinodes as the perpendicular electric field[76].

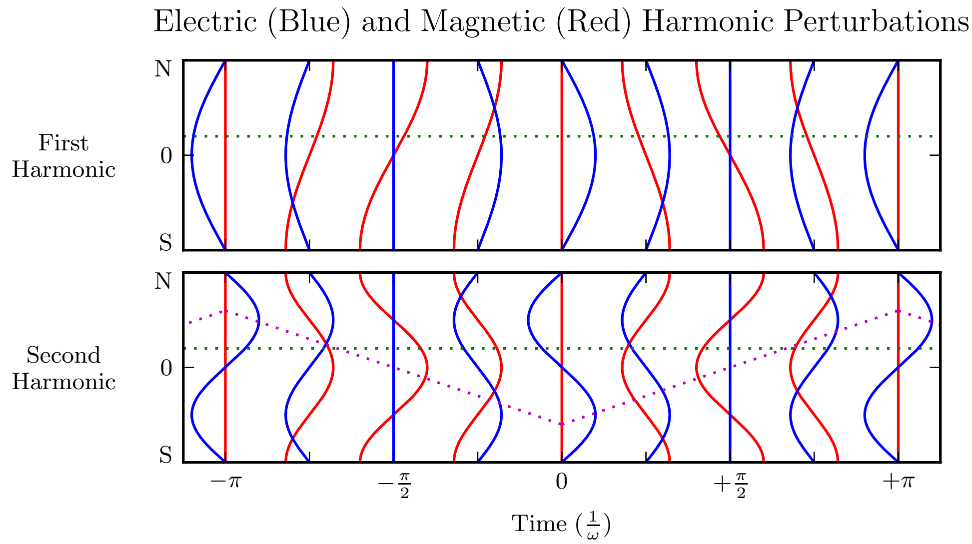

Figure 3.2: The first (or fundamental) harmonic has an an antinode in its perpendicular electric field (blue) at the equator, along with a node in its perpendicular magnetic field perturbation (red). A single satellite can identify the first harmonic by the relative phase of the electric and magnetic field perturbations: an observer north of the equator (green) will see the magnetic field perturbation lead the electric field by $\pm 90°$. The second harmonic is the opposite: it has an electric field node at the equator, and an observer north of the equator will see the magnetic field perturbation lag the electric field by $\mp 90°$. Top and bottom signs correspond to the poloidal (shown) and toroidal polarizations respectively. The purple line sketches the path of a particle in drift-bounce resonance; in the particle's rest frame, the electric field is always to the right.

Where ω is the frequency of the wave, ω_D and ω_B are the particle's drift and bounce frequencies respectively, and m is the wave's azimuthal modenumber, as discussed in Section 3.2.

In principle, the first and second harmonics can be distinguished by their frequencies, even from a single-point observation[2, 14, 34]. In practice, however, this is not a reliable approach[88]. Significant uncertainties surround the mass density profile — and thus the Alfvén speed profile — along a geomagnetic field line.

Harmonic structure can also be deduced by noting the phase offset between the wave magnetic field and its electric field (or the plasma velocity)[16, 91]. In Figure 3.2, the green line indicates an observer just north of the magnetic equator. For a wave polarized in the poloidal direction (see Section 3.3), the observer sees the electric field waveform offset from the magnetic field by a phase of $\pm 90^\circ$, where the top sign is for odd modes and the bottom sign is for even modes. The signs are flipped for toroidally-polarized waves, and again for waves observed south of the equator.

In addition to a wave's parity, the phase indicates how energy is divided between standing and traveling waves. Standing waves (phase of $\pm 90^\circ$) have a purely imaginary Poynting flux. Traveling waves (phase of 0° or 180°), on the other hand, have real Poynting flux, indicating a net movement of energy. Wave lifetimes can be estimated by comparing the energy density to the rate at which that energy is carried away by Poynting flux, as is done in Chapter 8.

Notably, the measurement of wave phase has only become viable with the advent of satellites carrying both electric and magnetic field instrumentation, such as THEMIS in 2007[3] and the Van Allen Probes (formerly RBSP, for Radiation Belt Storm Probes) in 2012[84].

Strictly speaking, the the phase offset of the electric and magnetic fields does not provide the harmonic number — only its parity. It's reasonably safe to assume that an even mode is the second harmonic; the second harmonic is by far the most commonly observed[43, 81, 89], due in part to its excitement by the antisymmetric balloon instability[9, 11, 12, 83]. However, the distinction between the first and third harmonics is not always clear[13, 34]; this issue is discussed further in Chapter 8. Higher harmonics than that are not expected in the Pc4 frequency band.

3.2 Azimuthal Modenumber

The wavelength of an FLR in the azimuthal direction is indicated by its azimuthal modenumber. A wave with modenumber m has an azimuthal wavelength that spans $\frac{24}{m}$ hours in MLT.

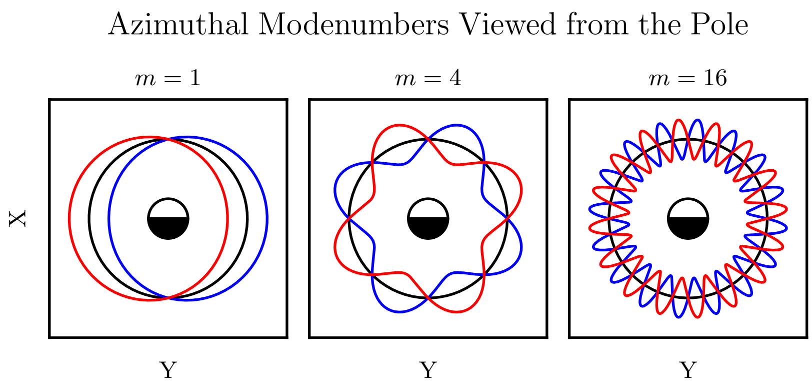

Figure 3.3: Above are qualitative sketches of waves with azimuthal modenumbers 1, 4, and 16, projected into the ecliptic plane. Black circles show unperturbed fields, while the blue and red curves show perturbations. At $m = 1$, the wave is more or less a uniform displacement, while at $m = 16$ azimuthal variations take place on spatial scales small compared to Earth's radius.

Waves with small azimuthal modenumbers ($0 < m < 10$) are typically driven by broadband energy sources at the magnetosphere's boundary, such as variations in the solar wind pressure[18, 38, 48, 104, 105], sporadic magnetic reconnection[41], or Kelvin-Helmholtz waves on the magnetopause[10, 57, 82]. In the low-m regime, the shear and compressional Alfvén waves are coupled, which allows energy to move across field lines until the driving frequency lines up with the local Alfvén frequency[59]. Because of their broadband energy source, low-m FLRs often have a mishmash of frequencies present in their spectra[16], though the spectra are coherent in terms of harmonic[25].

When the azimuthal modenumber is large (or, equally, when the azimuthal wavelength is small), compressional propagation of Alfvén waves becomes evanescent, so the movement of energy is guided by magnetic field lines[14, 76][6]. As a result, FLRs must be driven from within the magnetosphere. Proposed energy sources include phase space gradients near the plasmapause[17], particularly as the plasmasphere refills after a storm or substorm[24, 55].

[6]Equally, the strength of a wave's parallel component indicates its modenumber, a point which is revisited in Chapters 7 and 8.

The atmosphere is known to attenuate waves with small spatial extent in the perpendicular direction[42, 99, 103]. As a result, FLRs may create no signature on the ground if their azimuthal modenumber is large. For example, a recent paper by Takahashi shows a strong (2 nT at $L \sim 10$), clear resonance with $|m| \gtrsim 70$ and no corresponding ground signature[88].

Southwood[83] and Glassmeier[29] show that a low frequency wave passing through the ionosphere on its way to Earth will be attenuated per

$$\frac{B_E}{B_I} = \frac{\Sigma_H}{\Sigma_P} \exp\left(-m \frac{R_I - R_E}{R_E \sin\theta} \right) \tag{3.3}$$

Where B_E and B_I are the magnetic field strengths at R_E (Earth's surface, 6783 km geocentric) and R_I (the ionosphere, ∼6900 km geocentric) respectively. The integrated ionospheric Pedersen and Hall conductivities, Σ_P and Σ_H, are typically within a factor of two of one another. Field lines near the plasmapause can be traced to Earth at $\sin\theta \sim 0.4$. That is, by the time it reaches the ground, the magnetic field from an FLR with $m = 10$ is weaker by a factor of two; at $m = 100$, the factor is closer to 100.

3.3 Poloidal and Toroidal Polarizations

Based on polarization, each FLR can be classified as either poloidal or toroidal. The poloidal mode is a field line displacement in the meridional plane, as shown in Figure 3.4, with an accompanying electric field in the azimuthal direction. The toroidal mode's magnetic displacement is azimuthal, per Figure 3.5; the associated electric field is in the meridional plane.

Both poloidal and toroidal waves are noted for their ability to contribute to the energization and radial diffusion of trapped particles. The poloidal mode interacts more strongly, since its electric field is aligned with the trapped particles' drift motion. Poloidally-polarized waves are also more prone to creating magnetic signatures on the ground, due to ducting in the ionosphere[27, 36].

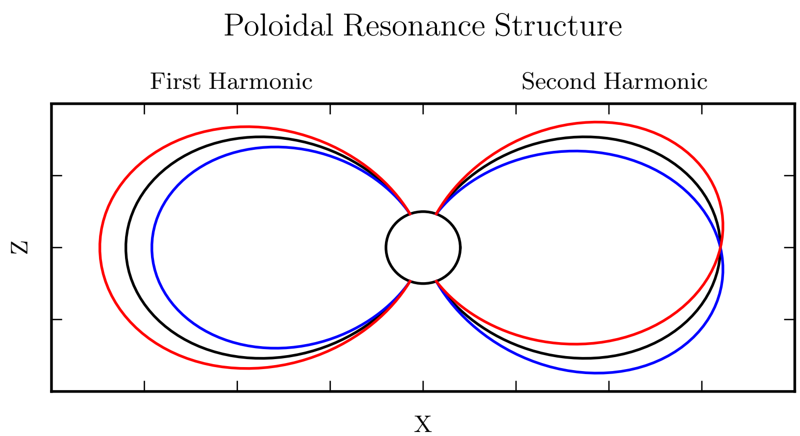

Figure 3.4: The poloidal resonance is a magnetic field in the meridional plane. The displacement is radial near the equator, and can be accompanied by enhancement in the parallel magnetic field near the ionosphere. The first harmonic is shown on the left, and the second harmonic on the right. Lines are colored red and blue only to contrast with the unperturbed black field line.

Toroidal modes have been shown to outnumber poloidal modes[2]. Perhaps not coincidentally, poloidally-polarized waves rotate asymptotically to the toroidal mode[64, 65, 76]. Poloidal waves with low azimuthal modenumber — such as those driven by broadband sources at the magnetopause — rotate on timescales comparable to their oscillation periods. The two modes are also coupled directly by the ionospheric Hall conductivity[46].

The eigenfrequencies for poloidal and toroidal FLRs are similar, though not identical[34]. It has furthermore been noted that toroidally-polarized waves exhibit a strong relationship between frequency and L-shell (or latitude), while poloidal waves at fixed frequency are spread more broadly in L[25].

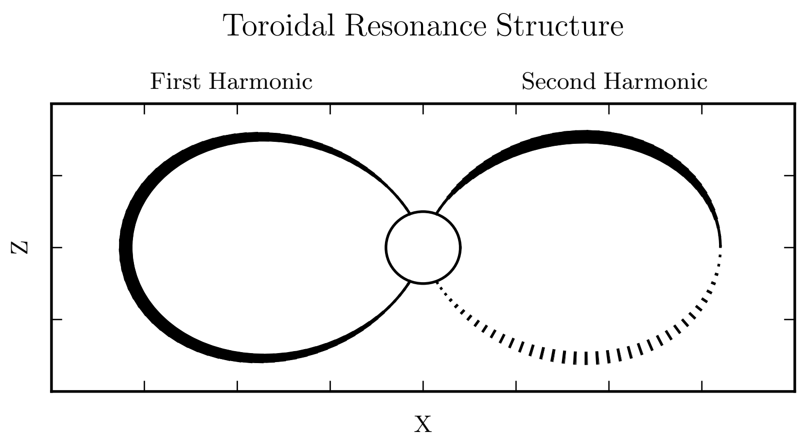

Figure 3.5: A toroidally-polarized FLR has a magnetic perturbation in the azimuthal direction, as shown. Bold lines are taken to be above the page, and dotted lines below the page, with the displacement indicated by the line's width. The first harmonic — where the entire field line oscillates in and out of the page — is shown on the left. The second harmonic is on the right, with northern and southern halves perturbed in opposite directions.

3.4 Giant Pulsations

The study of geomagnetic pulsations long predates satellites, sounding rockets, or even the word "magnetohydrodynamics"[7]. Large, regular oscillations in the magnetic field were noted as early as 1901[5]. Eventually, the term "giant pulsation," or Pg, arose to describe such pulsations.

On the ground, Pgs are notable for their strikingly sinusoidal waveforms, their eastward drifts, and their specific occurrence pattern: Pgs are typically seen pre-dawn, at latitudes of 60° to 70°. Pgs generally fall into the Pc4 frequency band[8]. Their harmonic structure was a source of controversy for decades, but recent multisatellite observations seem to be in agreement that they are odd harmonics, probably fundamental[30, 40, 51, 52, 87, 91]. They are poloidally polarized, with modenumbers $10 \lesssim m \lesssim 40$[28, 40, 73, 79, 91].

[7]The term was first used by Alfvén in the 1940s[1].

[8]The Pc4 range is periods of 45 s to 140 s, while Pgs range from 60 s to 200 s[7].

Whereas FLRs are waves in space which may produce ground signatures, "giant pulsation" refers to the ground signature specifically[9]. That is, Takahashi's satellite observation of a sinusoidal, morningside, high-m, fundamental poloidal resonance was not classified as a Pg because it did not produce a signal on the ground[88].

Due to their remarkably clear waveforms, Pgs are typically found by "visual inspection of magnetometer data"[68]. Over the course of the past century, a number of multi-year (sometimes multi-decade[7]) surveys have totaled nearly one thousand Pg events. On average, a ground magnetometer near 66° magnetic latitude observes $\sim$10 Pg events per year[7, 39, 78, 85]. Observations are not distributed uniformly; rather, giant pulsations are most common near the equinox and during times of low solar activity.

Unlike Pc4 pulsations in general, Pgs show no particular correlation with storm phase[68]. However, they do often occur as the magnetosphere recovers from a substorm[68, 79].

3.5 Motivations for the Present Work

A great deal has been learned — and continues to be learned — through observations of field line resonance. However, the cost-to-benefit ratio is climbing. As summarized in the sections above, FLR behavior depends significantly on harmonic structure, azimuthal modenumber, and polarization — not to mention frequency, spectral width, and so on. With each degree of freedom comes the necessity for an additional simultaneous observation.

Similarly, as FLRs have been shown to depend on ever-more-specific magnetospheric conditions, analytical techniques have fallen out of favor. The height-resolved ionosphere, multidimensional Alfvén speed profile, and inconvenient geometry combine to create a problem beyond the reasonable purview of pencil and paper.

That is, the topic of field line resonance is ripe for numerical modeling.

[9] Historically, the wave designations shown in Table 3.1 all referred to ground phenomena. Over time, they have come to describe satellite observations as well, including those without corresponding signatures on the ground.

Past models of the magnetosphere have been limited in their consideration of FLRs. Reasons include overly-simplified treatment of the ionospheric boundary, no consideration of the plasmapause, limited range in m, and the inability to compute ground signatures. Chapter 5 presents a model which addresses these issues, allowing the computation of field line resonance with unparalleled attention to realism.

The model allows a bird's-eye view of the structure and evolution of FLRs. As such, not only can several open questions be addressed, but their answers serve to unify a number of seemingly-disparate properties described in the sections above.

The rotation of poloidally-polarized waves to the toroidal mode is investigated. Particular attention is paid to the importance of azimuthal modenumber and ionospheric conductivity. The interplay between said rotation and the transport of energy across field lines — which also depends on azimuthal modenumber — is considered as well.

By their nature, drifting particles have the potential to spur wave-particle interactions at all MLT. However, Pc4 observations are strongly peaked on the dayside. In a 2015 paper, Dai notes, "It is not clear why noncompressional [high-m] Pc4 poloidal waves, which are presumably driven by instability within the magnetosphere, preferrentially occur on the dayside"[16]. Motoba, later that year, echoes, "It is unclear whether other generation mechanisms of fundamental standing waves ... can explain the localization of Pgs in local time"[68]. This, too, is considered numerically: to what degree is field line resonance affected by the (day-night asymmetric) conditions of the ionosphere?

An attempt is also made to demystify giant pulsations. It's been shown that toroidal Pc4s outnumber poloidal ones, and that most poloidal Pc4s are even, so perhaps it should come as no surprise that (poloidal, odd) Pgs are rare. Is it truly the case that Pgs are only "a small subset of fundamental poloidal waves"[88], set apart from the rest by their distinctive properties? Or, said another way, to what degree do the properties associated with Pgs arise in fundamental poloidal waves overall?

Chapter 4

Waves in Cold Resistive Plasma

Before delving into the implementation of the numerical model, it's instructive to consider the fundamental equations of waves in a cold, resistive plasma. Specifically, the present chapter is concerned with waves much slower than the electron cyclotron frequency. High-frequency waves such as the L and R modes are beyond the scope of the present work — and, in fact, beyond the limits of the model described in Chapter 5.

The evolution of electric and magnetic fields is governed by Ampère's law and Faraday's law. Notably, the present work takes the linearized versions of Maxwell's equations; the vectors $\underline{E}$ and $\underline{B}$ indicate perturbations above the zeroth-order magnetic field.

$$\underline{\underline{\epsilon}} \cdot \frac{\partial}{\partial t}\underline{E} = \frac{1}{\mu_0}\nabla \times \underline{B} - \underline{J} \qquad\qquad \frac{\partial}{\partial t}\underline{B} = -\nabla \times \underline{E} \tag{4.1}$$

Current follows Ohm's law. For currents perpendicular to the background magnetic field, Kirchhoff's formulation is sufficient. Conductivity is much higher along the magnetic field lines[1], so it's appropriate to also include the electron inertial term[2].

$$0 = \underline{\underline{\sigma}}_\perp \cdot \underline{E}_\perp - \underline{J}_\perp \qquad\qquad \frac{1}{\nu}\frac{\partial}{\partial t}J_z = \sigma_0 E_z - J_z \tag{4.2}$$

[1] The dipole coordinate system is defined rigorously in Section 5.1; at present, it's sufficient to take $\hat{z}$ parallel to the zeroth-order magnetic field, and $\hat{x}$ and $\hat{y}$ perpendicular to $\hat{z}$ (and to each other).

[2] Electron inertial effects are not included in the model described in Chapter 5, or in the results in Chapter 7; however, their implementation and impact are explored in Chapter 6.

Derivatives in Equations (4.1) and (4.2) can be evaluated by performing a Fourier transform. They can then be combined, eliminating the magnetic field and current terms.

$$\begin{aligned} 0 &= \underline{E}_\perp + \frac{v_A^2}{\omega^2}\left(\underline{k}\times\underline{k}\times\underline{E}\right)_\perp + \frac{i}{\epsilon_\perp\omega}\underline{\underline{\sigma}}_\perp\cdot \quad \underline{E}_\perp \\ 0 &= E_z \ + \frac{c^2}{\omega^2}\left(\underline{k}\times\underline{k}\times\underline{E}\right)_z \ + \frac{i\omega_P^2}{\omega\left(\nu - i\omega\right)}E_z \end{aligned} \tag{4.3}$$

The speed of light, Alfvén speed (including the displacement current correction), plasma frequency, and parallel conductivity are defined in the usual way:

$$c^2 \equiv \frac{1}{\mu_0\epsilon_0} \qquad v_A^2 \equiv \frac{1}{\mu_0\epsilon_\perp} \qquad \omega_P^2 \equiv \frac{ne^2}{m_e\epsilon_0} \qquad \sigma_0 \equiv \frac{ne^2}{m_e\nu} \tag{4.4}$$

Where the perpendicular dielectric constant $\epsilon_\perp$ is analogous to the electric constant ϵ_0, but for electric fields which are perpendicular to the preferred direction of the dielectric medium. As noted in Equation (3.1), $\epsilon_\perp \equiv \frac{\rho}{B^2}$ where ρ is the mass density and B is the magnitude of the (zeroth-order) magnetic field.

Using the vector identity $\underline{k}\times\underline{k}\times\underline{E} = \underline{k}\,\underline{k}\cdot\underline{E} - k^2\underline{E}$, Equation (4.3) can be reassembled into a single expression,

$$0 = \left(\underline{\underline{\mathbb{I}}} + \frac{1}{\omega^2}\underline{\underline{V}}^2\cdot\underline{k}\,\underline{k} - \frac{k^2}{\omega^2}\underline{\underline{V}}^2 + \frac{i}{\omega}\underline{\underline{\Omega}}\right)\cdot\underline{E} \tag{4.5}$$

Where $\underline{\underline{\mathbb{I}}}$ is the identity tensor and in x-y-z coordinates,

$$\underline{\underline{V}}^2 \equiv \begin{bmatrix} v_A^2 & 0 & 0 \\ 0 & v_A^2 & 0 \\ 0 & 0 & c^2 \end{bmatrix} \qquad \text{and} \qquad \underline{\underline{\Omega}} \equiv \begin{bmatrix} \frac{\sigma_P}{\epsilon_\perp} & \frac{-\sigma_H}{\epsilon_\perp} & 0 \\ \frac{\sigma_H}{\epsilon_\perp} & \frac{\sigma_P}{\epsilon_\perp} & 0 \\ 0 & 0 & \frac{\omega_P^2}{(\nu - i\omega)} \end{bmatrix} \tag{4.6}$$

The parenthetical expression in Equation (4.5) is the dispersion tensor. Nontrivial solutions exist only when its determinant is zero. This gives rise to a seventh-order polynomial in ω, so rather than a direct solution it's necessary to consider limits of specific interest.

In these limits, as explored in the sections below, the wave vector $\underline{k}$ is taken — without loss of generality — to lie in the x-z plane (that is, k_y is taken to be zero). The distinction between the two perpendicular components (k_x and k_y) is discussed in Section 4.4.

4.1 Guided Propagation

The wave vector of a field line resonance aligns closely to the background magnetic field. By supposing that the two align exactly (that is, taking $k_x = 0$), the parallel and perpendicular components of the dispersion relation are decoupled.

The parallel-polarized component ($E_x = E_y = 0$) is quadratic, and thus can be solved directly.

$$0 = \omega^2 + i\nu\omega - \omega_P^2 \qquad \text{so} \qquad \omega = -\frac{i\nu}{2} \pm \sqrt{\omega_P^2 - \frac{\nu^2}{4}} \tag{4.7}$$

It bears noting that the plasma frequency is large — not just compared to Pc4 frequencies, but even compared to the collision frequencies in the ionosphere[3]. Expanding Equation (4.7) with respect to large ω_P, the dispersion relation becomes

$$\omega^2 = \omega_P^2 \pm i\nu\omega_P + ... \tag{4.8}$$

Equation (4.8) can hardly be called a wave, as it does not depend on the wave vector $\underline{k}$. Rather, it is the plasma oscillation[4]: electrons vibrating in response to a charge separation along the background magnetic field.

The plasma oscillation is not specifically relevant to the study of field line resonance. The two phenomena are separated by six orders of magnitude in frequency. The topic is revisited in Chapter 6 insomuch as it is inseparable from the electron inertial effects in Ohm's law, but it is otherwise not relevant to the work at hand.

[3]The collision frequency may match or exceed the plasma frequency for a thin slice at the bottom of the ionosphere, where the density of neutral atoms is large; however, it falls off quickly. Above an altitude of 200 km, conservatively[71], the plasma frequency exceeds the collision frequency by an order of magnitude or more.

[4]The plasma oscillation is also called the Langmuir wave.

The perpendicular ($E_z = 0$) components of the dispersion relation give an expression quartic in ω.

$$0 = \omega^4 + 2i\frac{\sigma_P}{\epsilon_\perp}\omega^3 - \left(2k_z^2 v_A^2 + \frac{\sigma_P^2 + \sigma_H^2}{\epsilon_\perp^2}\right)\omega^2 - 2ik_z^2 v_A^2 \frac{\sigma_P}{\epsilon_\perp}\omega + k_z^4 v_A^4 \tag{4.9}$$

Like the parallel-polarized component above, Equation (4.9) can be solved directly. Noting that $\pm$ and $\bigoplus$ are independent,

$$\omega = \left(\frac{\pm\sigma_H - i\sigma_P}{2\epsilon_\perp}\right) \bigoplus \sqrt{k_z^2 v_A^2 + \left(\frac{\pm\sigma_H - i\sigma_P}{2\epsilon_\perp}\right)^2} \tag{4.10}$$

Also like the parallel-polarized component, the exact solution is less useful than its Taylor expansion. The Pedersen and Hall conductivities are large near the ionospheric boundary, but fall off quickly; for the vast majority of the field line, the ratios $\frac{\sigma_P}{\epsilon_\perp}$ and $\frac{\sigma_H}{\epsilon_\perp}$ are small compared to field line resonance frequencies. Expanding with respect to small conductivity gives

$$\omega^2 = k_z^2 v_A^2 \bigoplus k_z v_A \frac{\sigma_H \pm i\sigma_P}{\epsilon_\perp} + ... \tag{4.11}$$

This is the shear Alfvén wave, with a shift in its frequency proportional to the characteristic conductivity of the ionosphere[5]. The wave travels along the background magnetic field like a bead on a string, with electric and magnetic field perturbations perpendicular to the magnetic field line (and to one another).

4.2 Compressional Propagation

The partner to guided motion is compressional motion; in order for energy to move across field lines, the wave vector must have a component perpendicular to $\hat{z}$. If the

[5] Admittedly, it's difficult to say what constitutes a chatacteristic conductivity. The Pedersen and Hall conductivities vary by several orders of magnitude within the ionosphere, then drop essentially to zero at large radial distance.

wave vector is completely perpendicular to the magnetic field line ($k_z = 0$), the parallel and perpendicular components of the dispersion relation decouple, as in Section 4.1.

The parallel-polarized ($E_x = E_y = 0$) component of the dispersion relation is

$$0 = \omega^3 + i\nu\omega^2 - \left(k_x^2 c^2 + \omega_P^2\right)\omega - ik_x^2 c^2 \nu \tag{4.12}$$

Equation (4.12) can be solved directly, though its solution (as a cubic) is far too long to be useful. Expanding with respect to the large plasma frequency, gives

$$\omega^2 = k^2 c^2 + \omega_P^2 - i\nu\omega_P + ... \tag{4.13}$$

This is the O mode, a compressional wave with an electric field perturbation along the background magnetic field. Like the plasma oscillation discussed in Section 4.1, its frequency is very large compared to that of a field line resonance, putting it beyond the concern of the present work.

The perpendicular-polarized ($E_z = 0$) component of the compressional dispersion relation is also cubic.

$$0 = \omega^3 + 2i\frac{\sigma_P}{\epsilon_\perp}\omega^2 - \left(2k_x^2 v_A^2 + \frac{\sigma_P^2 + \sigma_H^2}{\epsilon_\perp^2}\right)\omega - ik_x^2 v_A^2 \frac{\sigma_P}{\epsilon_\perp} \tag{4.14}$$

A wave moving across magnetic field lines near the ionospheric boundary will encounter large $\frac{\sigma_P}{\epsilon_\perp}$ and $\frac{\sigma_H}{\epsilon_\perp}$, while at moderate to high altitudes those ratios will be small. Solving Equation (4.14) in those two limits respectively gives:

$$\omega^2 = k_x^2 v_A^2 \pm ik_x v_A \frac{\sigma_P}{\epsilon_\perp} + ... \qquad \text{and} \qquad \omega^2 = k_x^2 v_A^2 + \left(\frac{\sigma_H \pm i\sigma_P}{\epsilon_\perp}\right)^2 + ... \tag{4.15}$$

At first glance, both limits of Equation (4.15) appear to describe compressional Alfvén waves. The magnetic perturbation is along the background magnetic field — indicating compression of the frozen-in plasma — while the electric field perturbation is perpendicular to both the magnetic field and the wave vector.

However, in the high-conductivity limit, the parenthetical term actually dominates the Alfvén term, taking values as large as $\sim 10^6$ Hz. Waves at such frequencies are beyond the scope of the present work. As a matter of interest, however, it bears noting that — as long as $\nu \ll 10^6$ Hz — $\frac{\sigma_H}{\epsilon_\perp}$ reduces to the electron cyclotron frequency, $\frac{eB}{m_e}$.

4.3 High Altitude Limit

In the limit of large radial distance, it's reasonable to take the collision frequency to zero; doing so also neglects the Pedersen and Hall conductivities.

Whereas in Sections 4.1 and 4.2 it was the parallel-polarized component of the dispersion relation that factored out from the other two, the high altitude limit decouples the component polarized out of the x-z plane. The y-polarized ($E_x = E_z = 0$) dispersion relation is simply:

$$\omega^2 = k^2 v_A^2 \tag{4.16}$$

Equation (4.16) describes an Alfvén wave with an arbitrary angle of propagation. Depending on the angle between the wave vector and the background magnetic field, it could be guided, compressional, or somewhere in between. Regardless of propagation angle, the electric field perturbation is perpendicular to both the direction of propagation and the magnetic field perturbation.

The other two components (from $E_y = 0$) of the high altitude dispersion tensor give an expression quadratic in ω^2:

$$0 = \omega^4 - \left(k_x^2 c^2 + k_z^2 v_A^2 + \omega_P^2\right) \omega^2 + k_z^2 v_A^2 \omega_P^2 \tag{4.17}$$

Which can be solved for

$$\omega^2 = \frac{1}{2}\left(k_x^2 c^2 + k_z^2 v_A^2 + \omega_P^2\right) \pm \sqrt{\frac{1}{4}\left(k_x^2 c^2 + k_z^2 v_A^2 + \omega_P^2\right)^2 - k_z^2 v_A^2 \omega_P^2} \tag{4.18}$$

Noting again that ω_P is very large, the two roots can be expanded to

$$\omega^2 = k_z^2 v_A^2 \left(\frac{\omega_P^2}{\omega_P^2 + k_x^2 c^2 + k_z^2 v_A^2} \right) + ... \quad \text{and} \quad \omega^2 = k_x^2 c^2 + k_z^2 v_A^2 + \omega_P^2 + ... \tag{4.19}$$

The first solution of Equation (4.19) is a shear Alfvén wave — in the limit of present interest, ω_P is large, so the parenthetical quantity is close to unity. The inertial limit, where frequencies are close to the plasma frequency, is beyond the scope of the present work. For that same reason, the second solution (which describes an oscillation faster than the plasma frequency) is not further considered.

4.4 Implications to the Present Work

The present section's findings carry three implications of particular significance to the present work.

First — with the exception of the plasma oscillation and similar modes, which are revisited in Chapter 6 — waves propagate at the Alfvén speed. This, in combination with the grid configuration, constrains the time step that can be used to model them numerically. The time step must be sufficiently small that information traveling at the Alfvén speed cannot "skip over" entire grid cells[6].

Second, the results of the present section allow an estimate of the magnitude of parallel electric field that might be expected from a field line resonance compared to its perpendicular electric field. Between the full dispersion tensor form in Equation (4.5) and the Alfvén wave described by Equation (4.19),

$$\left| \frac{E_z}{E_x} \right| = \frac{k_x k_z c^2}{\omega^2 - k_x^2 c^2 - \omega_P^2} \sim \frac{k^2 c^2}{\omega_P^2} \tag{4.20}$$

In essence, the relative magnitudes of the parallel and perpendicular electric fields should scale quadratically with the ratio of the electron inertial length ($\frac{c}{\omega_P} \sim 1\,\text{km}$ to $100\,\text{km}$)

[6] As is the convention, the time step is scaled down from the smallest Alfvén zone crossing time by a Courant factor, typically 0.1, meaning that it takes at least ten time steps to cross a grid cell.

and the FLR wavelength ($\frac{1}{k} \sim 10^5\,\text{km}$). That is, parallel electric fields should be smaller than perpendicular ones by at least six orders of magnitude.

Finally, the dispersion relations shown above indicate how the behavior of a field line resonance should behave as the azimuthal modenumber becomes large.

Whereas the shear Alfvén wave's dispersion relation depends only on the parallel component of the wave vector, the compressional Alfvén wave depends on its magnitude: $\omega^2 = k^2 v_A^2$. If the frequency is smaller than $k v_A$, the wave will become evanescent. The wave vector's magnitude can be no smaller than its smallest component, however, and the azimuthal component scales with the azimuthal modenumber: $k_y \sim \frac{m}{2\pi r}$.

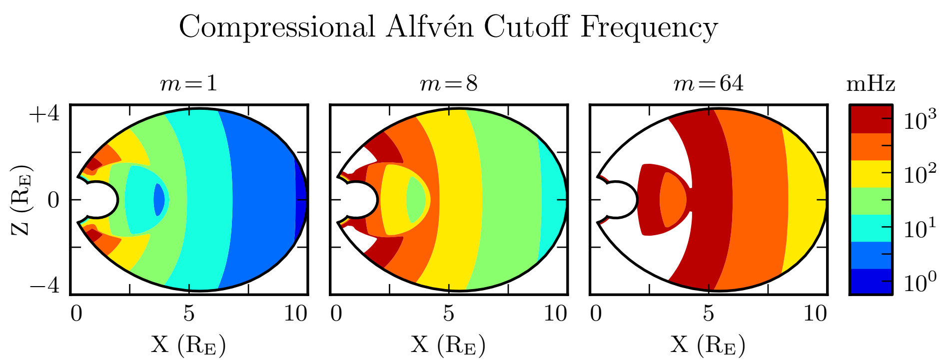

Figure 4.1: Taking $k_y \sim \frac{m}{2\pi r}$ as a lower bound for the magnitude of the wave vector, the above figure demonstrates the lowest frequency at which compressional Alfvén waves may propagate as a function of position and m. Regions shown in white are off the color scale — they have a lower bound on the order of $10^4\,\text{mHz}$ or more. The above Alfvén frequency profile is from Kelley[47], for quiet dayside conditions, as discussed in Section 5.2.

This imposes a frequency cutoff on compressional Alfvén waves which scales with the azimuthal modenumber, as shown in Figure 4.1. At small values of m, most of the magnetosphere is conducive to compressional Alfvén waves in the Pc4 frequency range. As m increases, and the wave vector with it, the inner magnetosphere becomes increasingly inaccessible to them.

Chapter 5

"Tuna Half" Dimensional Model

The present section describes the implementation of Tuna, a new two and a half dimensional Alfvén wave code based largely on work by Lysak[58, 61].

The half-integer dimensionality refers to the fact that Tuna's spatial grid resolves a two-dimensional slice of the magnetosphere, but that electric and magnetic fields — as well as their curls — are three-dimensional vectors. This apparent contradiction is reconciled by the use of a fixed azimuthal modenumber, m. Electric and magnetic fields are taken to be complex-valued, varying azimuthally per $\exp(im\phi)$; derivatives with respect to ϕ are then replaced by a factor of im.

Unlike a fully three-dimensional code, Tuna cannot resolve the evolution of wave structures in the azimuthal direction. Furthermore, the model does not allow coupling between the dayside and nightside magnetospheres. What Tuna does offer is efficiency. The model's economical geometry allows it to include a realistic Earthward boundary: grid spacing on the order of 10 km, a height-resolved ionospheric conductivity tensor, and even the computation of magnetic field signatures at the ground. Such features would pose a prohibitive computational expense in a large global code.

Tuna was developed with field line resonance in mind. As discussed in Chapter 3, such waves extend over just a few hours MLT, minimizing the importance of Tuna's missing half dimension. Moreover, because field line resonances are known to be affected by both the ionosphere and the plasmasphere, a faithful treatment of the inner magnetosphere is a crucial part of studying them numerically.

Perhaps the most exciting feature of Tuna is its novel driving mechanism: ring current perturbation. Codes similar to Tuna have traditionally been driven using compressional pulses at the outer boundary[58, 61, 97, 98]. This has precluded the investigation of waves with large azimuthal modenumber — such as giant pulsations — which are guided, and thus must be driven from within the magnetosphere.

Tuna's source code, written in Fortran, is publicly available at `https://github.com/UMN-Space-Physics`. The repository also includes a pair of Python scripts: a test harness — which automates programming environment setup, compilation, and interfacing with the supercomputer queue — and a plotter.

5.1 Coordinate System

Field line resonance has traditionally been modeled by straightening the field lines into a rectangular configuration[20, 64], by unrolling the azimuthal coordinate into a cylindrical coordinate system[76], or through the use of dipole coordinates[75][1]:

$$x \equiv -\frac{\sin^2\theta}{r} \qquad\qquad y \equiv \phi \qquad\qquad z \equiv \frac{\cos\theta}{r^2} \tag{5.1}$$

Where r, θ, and ϕ take on their usual spherical meanings of radial distance, colatitude, and azimuthal angle respectively.

The dipole coordinate x is constant over each L-shell[2], y is azimuthal angle, and z indexes each field line from south to north. The unit vectors $\hat{x}$, $\hat{y}$, and $\hat{z}$ point in the crosswise[3] (radially outward at the equator), azimuthal (eastward), and parallel (northward at the equator) directions respectively.

[1]The dipole coordinates x, y, and z are sometimes named ν, ϕ, and μ respectively.

[2]In fact, x is inversely proportional to L.

[3]In the context of in situ measurements taken near the equatorial plane, $\hat{x}$ is referred to as the radial direction; however, the present work extends the dipole grid to low altitudes, where $\hat{x}$ is often more horizontal than vertical. The term "crosswise" is meant to indicate that $\hat{x}$ is defined by the cross product of $\hat{y}$ and $\hat{z}$.

Notably, the dipole coordinates in Equation (5.1) are normal to one another. While mathematically convenient, they do not readily accommodate a fixed-altitude boundary at the ionosphere, nor do they allow the dipole magnetic field to intersect the boundary at an oblique angle, as Earth's field does. As a solution, a nonorthogonal set of dipole coordinates was developed numerically by Proehl[74], then formalized analytically by Lysak[58] in terms of their contravariant components:

$$u^1 = -\frac{R_I}{r}\sin^2\theta \qquad\qquad u^2 = \phi \qquad\qquad u^3 = \frac{R_I^2}{r^2}\frac{\cos\theta}{\cos\theta_0} \tag{5.2}$$

Above, R_I is the position of the ionosphere relative to Earth's center; it's typically taken to be $1\,\mathrm{R_E} + 100\,\mathrm{km}$.

Like the dipole coordinates x, y, and z, Lysak's coordinates u^1, u^2, and u^3 correspond to L-shell, azimuthal angle, and position along a field line respectively. However, compared to z, u^3 has been renormalized using the invariant colatitude[4] θ_0. As a result, u^3 takes the value $+1$ at the northern ionospheric boundary and -1 at the southern ionospheric boundary for all field lines.

Because Lysak's coordinate system is not orthogonal — that is, because curves of constant u^1 and curves of constant u^3 can intersect at non-right angles — it's necessary to consider covariant and contravariant basis vectors separately.

$$\hat{e}_i \equiv \frac{\partial}{\partial u^i}\underline{x} \qquad\qquad \hat{e}^i \equiv \frac{\partial}{\partial \underline{x}}u^i \tag{5.3}$$

Covariant basis vectors $\hat{e}_i$ are normal to the curve defined by constant u^i, while contravariant basis vectors $\hat{e}^i$ are tangent to the coordinate curve (equivalently, $\hat{e}^i$ is normal to the plane defined by constant u^j for all $j \neq i$). These vectors are reciprocal to one another, and can be combined to give components of the metric tensor $\underline{\underline{g}}$[19].

$$\hat{e}^i \cdot \hat{e}_j = \delta^i_j \qquad\qquad g_{ij} \equiv \hat{e}_i \cdot \hat{e}_j \qquad\qquad g^{ij} \equiv \hat{e}^i \cdot \hat{e}^j \tag{5.4}$$

[4] The invariant colatitude is the colatitude θ at which a field line intersects the ionosphere. It is related to the McIlwain parameter by $\cos\theta_0 \equiv \sqrt{1 - \frac{R_I}{L}}$.

The symbol δ^i_j is the Kronecker delta; the present work also makes use of the Levi-Civita symbol ε^{ijk} and Einstein's convention of implied summation over repeated indeces[22].

The metric tensor allows rotation between covariant and contravariant representations of vectors.

$$A_i = g_{ij} A^j \qquad \text{and} \qquad A^i = g^{ij} A_j \qquad \text{where} \qquad A_i \equiv \underline{A} \cdot \hat{e}_i \qquad \text{and} \qquad A^i \equiv \underline{A} \cdot \hat{e}^i \tag{5.5}$$

In addition, the determinant of the metric tensor is used to define cross products and curls[5].

$$\left(\underline{A} \times \underline{B}\right)^i = \frac{\varepsilon^{ijk}}{\sqrt{g}} A_j B_k \qquad \text{and} \qquad \left(\nabla \times \underline{A}\right)^i = \frac{\varepsilon^{ijk}}{\sqrt{g}} \frac{\partial}{\partial u^j} A_k \qquad \text{where} \qquad g \equiv \det \underline{\underline{g}} \tag{5.6}$$

Explicit forms of the basis vectors and metric tensor can be found in the appendix of Lysak's 2004 paper[58]. At present, it's sufficient to note the mapping between Lysak's basis vectors and the usual dipole unit vectors.

$$\hat{x} = \frac{1}{\sqrt{g^{11}}} \hat{e}^1 \qquad \qquad \hat{y} = \frac{1}{\sqrt{g^{22}}} \hat{e}^2 \qquad \qquad \hat{z} = \frac{1}{\sqrt{g_{33}}} \hat{e}_3 \tag{5.7}$$

The basis vectors can also be mapped to the spherical unit vectors, though Equation (5.8) is valid only at the ionospheric boundary.

$$\hat{\theta} = \frac{1}{\sqrt{g_{11}}} \hat{e}_1 \qquad \qquad \hat{\phi} = \frac{1}{\sqrt{g_{22}}} \hat{e}_2 \qquad \qquad \hat{r} = \frac{1}{\sqrt{g^{33}}} \hat{e}^3 \tag{5.8}$$

The coordinates converge at the equatorial ionosphere, so an inner boundary is necessary to maintain finite grid spacing. It's typically placed at $L = 2$. The outer boundary is at $L = 10$. The dipole approximation of Earth's magnetic field is tenuous at the outer boundary; however, in practice, wave activity is localized inside $L \sim 7$. The grid is spaced uniformly in u^1, which gives finer resolution close to Earth and coarser resolution at large distances.

[5]The square root of the determinant of the metric tensor is called the Jacobian. It's sometimes denoted using the letter J, which is reserved for current in the present work.

Spacing in u^3 is set by placing grid points along the outermost field line. The points are closest together at the ionosphere, and grow towards the equator. The spacing increases in a geometric fashion, typically by $3\,\%$.

Typically, Tuna uses a grid 150 points in u^1 by 350 points in u^3. The result is a resolution on the order of $10\,\text{km}$ at the ionosphere, which increases to the order of $10^3\,\text{km}$ at the midpoint of the outermost field line.

There are no grid points in u^2 due to the two-and-a-half-dimensional nature of the model. Fields are assumed to vary as $\exp\left(imu^2\right)$ — equally, $\exp(im\phi)$ — so derivatives with respect to u^2 are equivalent to a factor of im. In effect, the real component of each field is azimuthally in phase with the (purely real) driving, while imaginary values represent behavior that is azimuthally offset. Azimuthal modenumbers span the range $1 \lesssim m \lesssim 100$, consistent with observations of Pc4 and Pg events[16, 17, 68, 88].

The simulation's time step is set based on the grid spacing. As is the convention, δt is set to match the smallest Alfvén zone crossing time, scaled down by a Courant factor (typically 0.1). It bears noting that the smallest crossing time need not correspond to the smallest zone; the Alfvén speed peaks several thousand kilometers above Earth's surface, in the ionospheric Alfvén resonator[61]. A typical time step is on the order of $10^{-5}\,\text{s}$.

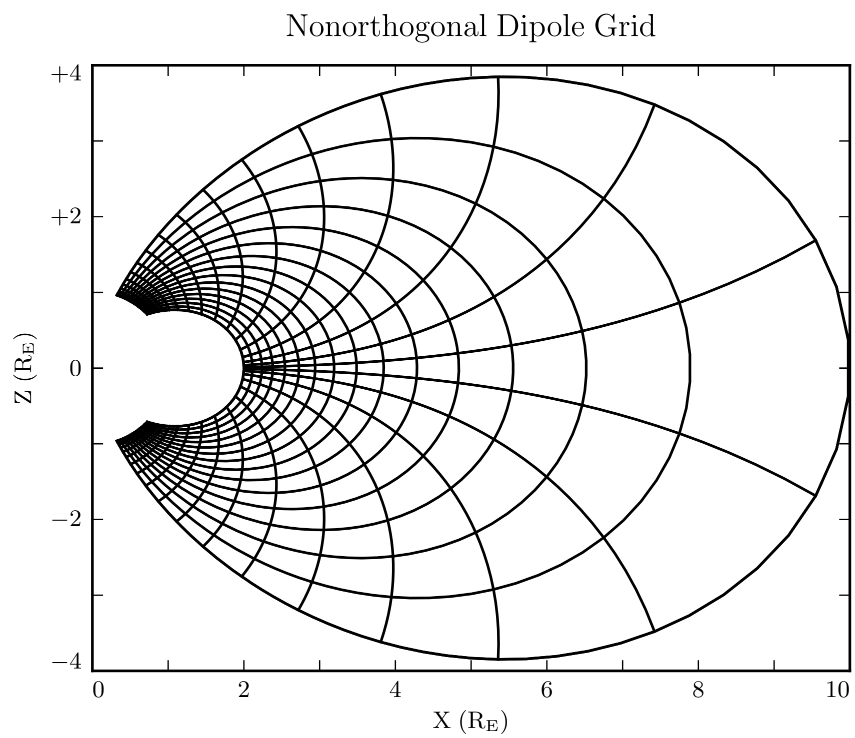

Figure 5.1: The model's nonorthorthogonal dipole grid. Every fifth point is shown in each direction. The high concentration of grid points near Earth's equator is a consequence of the coordinate system, which converges at the equatorial ionosphere. Earth (not shown) is centered at the origin with unit radius.

5.2 Physical Parameter Profiles

Tuna models Earth's magnetic field to be an ideal dipole, so the zeroth-order field strength is written in the usual form:

$$\underline{B}_0 = 3.1 \times 10^4 \,\mathrm{nT} \left(\frac{R_E}{r}\right)^3 \left(2\cos\theta\,\hat{r} - \sin\theta\,\hat{\theta}\right) \tag{5.9}$$

Number density is taken to be the sum of an inverse-radial-dependent auroral profile and a plasmaspheric profile dependent on the L-shell[61]:

$$n = n_{AZ}\frac{r_{AZ}}{r} + n_{PS}\exp\left(\frac{-L}{L_{PS}}\right)\left(\frac{1}{2} - \frac{1}{2}\tanh\frac{L - L_{PP}}{\delta L_{PP}}\right) \tag{5.10}$$

Where typical values are shown in Table 5.1.

Table 5.1: Typical Parameters for the Tuna Density Profile

Variable	Value	Description
L_{PS}	1.1	Scale L of the plasmasphere.
L_{PP}	4.0	Location of the plasmapause.
δL_{PP}	0.1	Thickness of the plasmapause.
n_{AZ}	10 /cm^3	Number density at the base of the auroral zone.
n_{PS}	10^4 /cm^3	Number density at the base of the plasmasphere.
r_{AZ}	1 $\mathrm{R_E}$	Scale height of the auroral density distribution.

The perpendicular component of the electric tensor, $\epsilon_\perp$, is computed based on Kelley's[47] tabulated low-density values, ϵ_K, which are adjusted to take into account the effects of high density in the plasmapause.

$$\epsilon_\perp = \epsilon_K + \frac{Mn}{B_0^2} \tag{5.11}$$

Where M is the mean molecular mass, which is large (~28 u) at 100 km altitude, then drops quickly (down to 1 u by ~1000 km)[61].

The Alfvén speed profile is computed from the perpendicular electric constant in the usual way, $v_A^2 \equiv \frac{1}{\mu_0\epsilon_\perp}$. This form takes into account the effect of the displacement current, which becomes important in regions where the Alfvén speed approaches the speed of light.

While the density profile is held constant for all runs discussed in the present work, the Alfvén speed profile is not. Four different profiles are used for the low-density

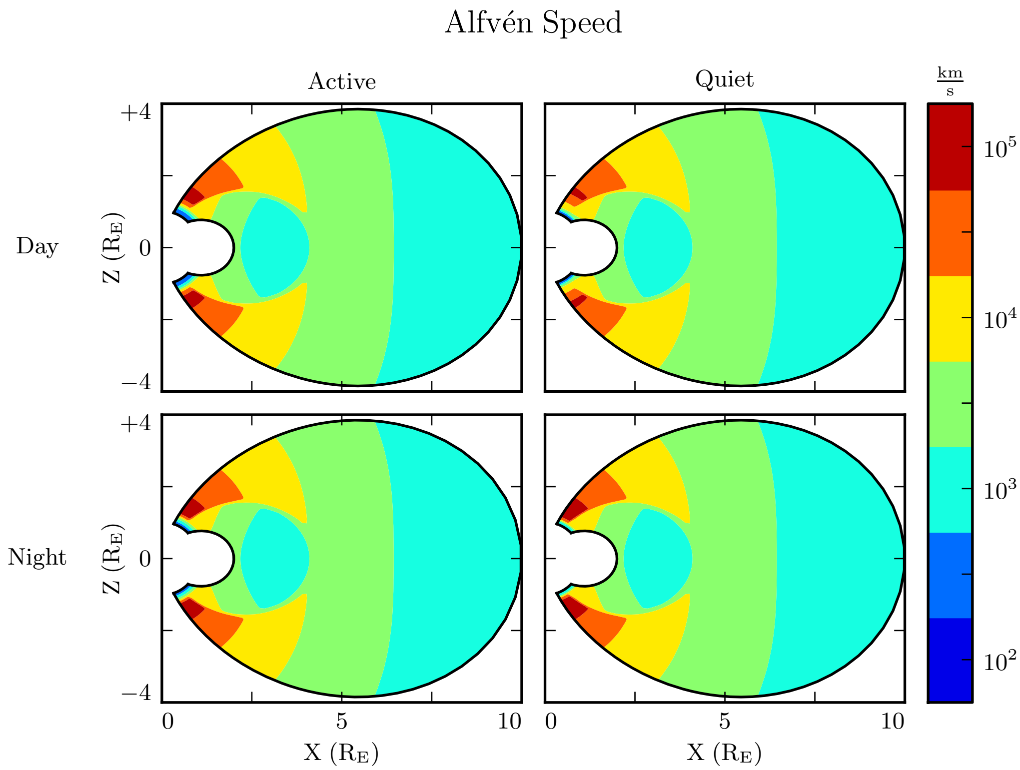

Figure 5.2: Alfvén speed profiles are based on low-density values tabulated by Kelley[47]. They are adjusted to take into account the density of the plasmapause and mass loading near the Earthward boundary.

perpendicular electric constant ϵ_K, corresponding to the differing ionospheric conditions between the dayside and the nightside, and between the high and low points in the solar cycle. These differences are visible in Figure 5.2, particularly in the size of the ionospheric Alfvén resonator (the peak in Alfvén speed in the high-latitude ionosphere).

Ionospheric conductivity profiles are also based on values tabulated by Kelley, adjusted by Lysak[61] to take into account the abundance of heavy ions near the Earthward boundary. Pedersen, Hall, and parallel conductivities are each resolved by altitude, as shown in Figure 5.3.

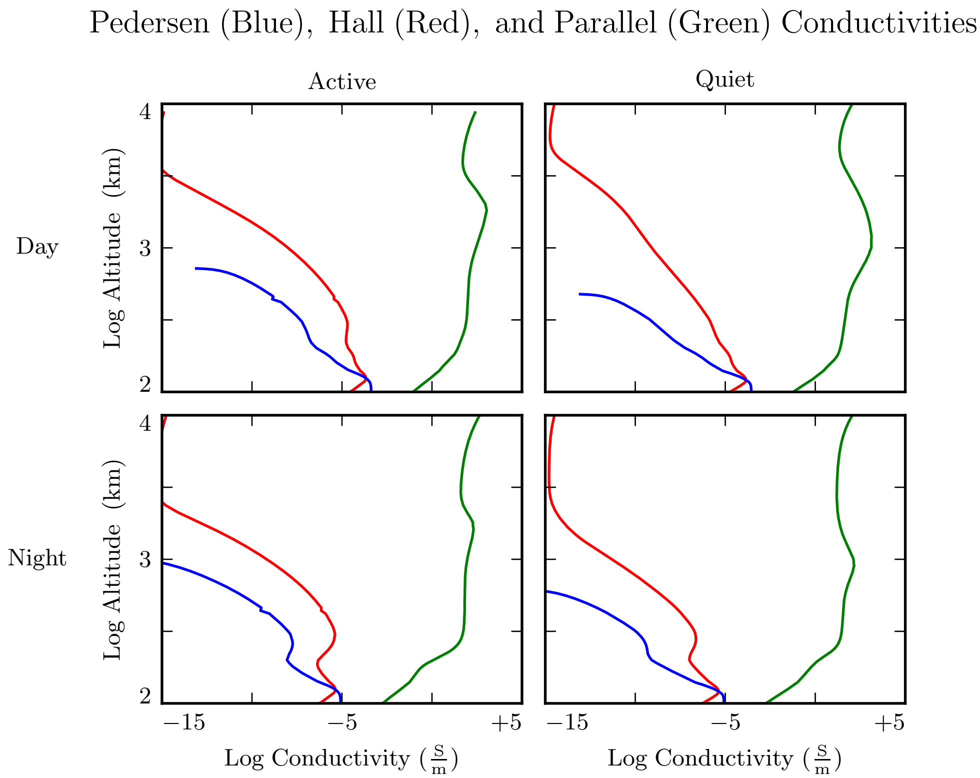

Figure 5.3: Ionospheric conductivity profiles are adapted by Lysak[61] from Kelley's tabulated values[47], in order to take into account the effects of heavy ions at low altitudes. These profiles allow Tuna to simulate magnetosphere-ionosphere coupling under a variety of conditions.

Tuna's physical parameter profiles are static over the course of each run. Even so-called ultra low frequency waves like Pc4 pulsations are fast compared to convective timescales in the magnetosphere.

5.3 Driving

Models similar to Tuna have traditionally been driven using compression at the outer boundary[58, 61, 97, 98]. Such driving acts as a proxy for solar wind compression, Kelvin-Helmholtz effects at the magnetopause, and so on. However, because of the guided nature of high-modenumber Alfvén waves, simulations driven from the outer boundary are constrained to the consideration of waves with low azimuthal modenumber (equivalently, large azimuthal wavelength).

This issue is demonstrated in Figure 5.4. At low modenumber, energy delivered at the outer boundary propagates across field lines in order to stimulate resonances in the inner magnetosphere. However, as modenumber increases, Alfvén waves become increasingly guided, and the inner magnetosphere is unaffected by perturbations at the outer boundary.

In order to simulate high-modenumber Alfvén waves in the inner magnetosphere — such as giant pulsations — a new driving mechanism is necessary. Perturbation of the ring current is a natural choice, as Alfvén waves in the Pc4 range are known to interact with ring current particles through drift and drift-bounce resonances. The ring current is a dynamic region, particularly during and after geomagnetic storms and substorms; it's easy to imagine the formation of localized inhomogeneities.

In order to estimate an appropriate magnitude for perturbations of the ring current, the Sym-H storm index[6] is used. The index is measured once per minute, and so cannot directly detect ring current modulations in the Pc4 frequency range. Instead, the index is transformed into the frequency domain, allowing a fit of its pink noise[7].

As shown in Figure 5.5, a Fourier transform of the Sym-H index (taken here from the June 2013 storm) suggests that magnetic field perturbations at Earth's surface due to ring current activity in the Pc4 frequency range could be up to the order of $10^{-2}\,\mathrm{nT}$. Supposing that the ring current is centered around $5\,\mathrm{R_E}$ geocentric, that corresponds to a current on the order of $0.1\,\mathrm{MA}$. Tuna's driving is spread using a Gaussian profile in u^1 (typically centered at $L = 5$) and u^3 (typically centered just off the equator), with a characteristic area of $1\,\mathrm{R_E}^2$; this gives a current density on the order of $10^{-4}\,\mathrm{\mu A/m^2}$.

Admittedly, Sym-H is an imperfect tool for estimating the magnitude of localized perturbations to the ring current, particularly those with high modenumber. As a global

[6] Sym-H is analogous to DST, and the two match each other closely[96]. The crucial difference in this case is that Sym-H is recorded at a higher frequency.

[7] Pink noise, also called $\frac{1}{f}$ noise, refers to the power law decay present in the Fourier transforms of all manner of physical signals.

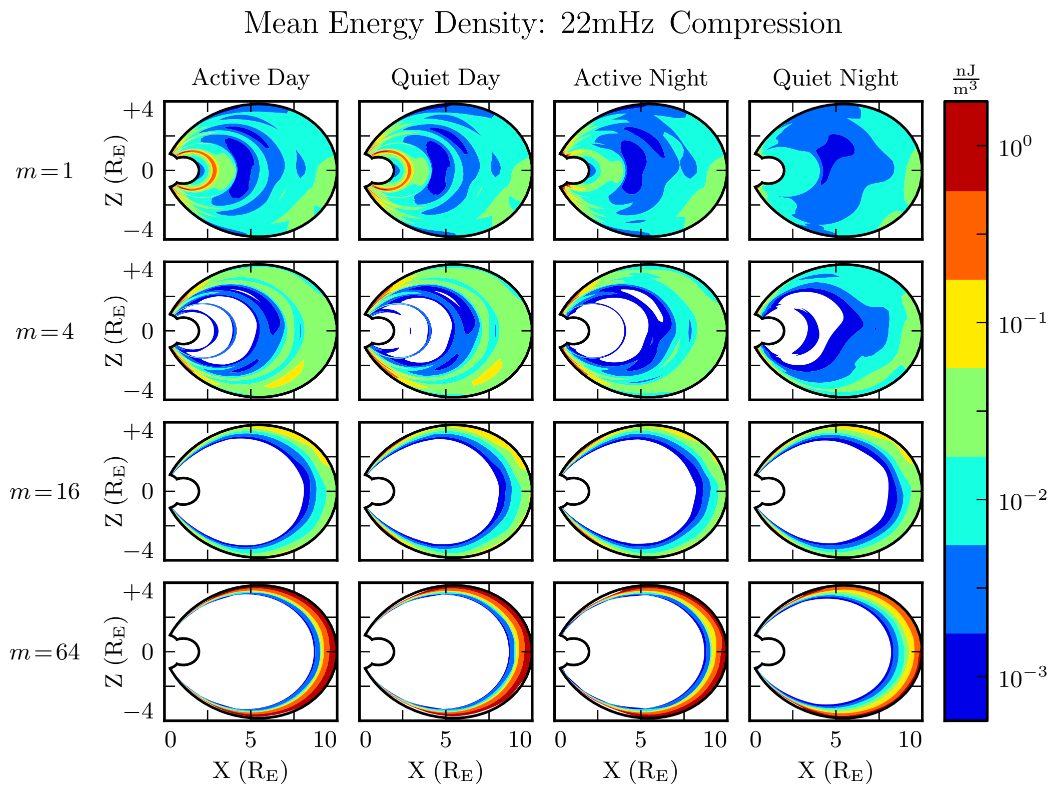

Figure 5.4: Each cell presents the mean energy density over the course of a 300 s run, as a function of position, due to compressional driving at the outer boundary. Azimuthal modenumber varies by row, and ionospheric conditions vary by column. For runs with small azimuthal modenumber, it's clear that energy is able to propagate across field lines and stimulate wave activity in the inner magnetosphere. When the modenumber is large, energy is unable to penetrate to the inner magnetosphere. Notably, the large values on the bottom row should be taken with a grain of salt; it's not clear that the model's results are reliable when waves are continuously forced against the boundary.

index, its values are effectively averaged around Earth. Unlike in situ measurements, however, this method has the advantage of estimating total driving current (and thus total energy input).

In the results shown in Chapters 6 and 7, the driving current is sinusoidal, and delivered purely in the azimuthal direction (representing a perturbation to the magnitude of the

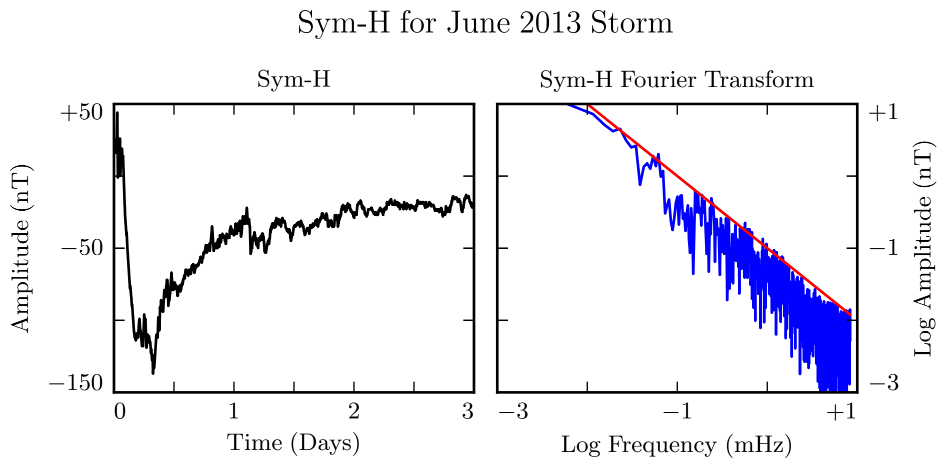

Figure 5.5: The Sym-H storm index[69] measures magnetic perturbations on Earth's surface due to ring current activity. The amplitude of oscillations in the Pc4 range is estimated by fitting the pink noise in its Fourier transform.

ring current, but not to its direction). Tuna also allows several other driving waveforms, and the direction of the current could be modified with trivial modifications to the code.

5.4 Maxwell's Equations

Tuna simulates the evolution of electromagnetic waves in accordance with Ampère's law and Faraday's law. Computation is carried out on a Yee grid[102]: electric fields and magnetic fields are offset by half a time step, and each field component is defined on either odd or even grid points in each dimension to ensure that curls are computed using centered differences.

The Ohmic current in Ampère's law is replaced with $\underline{\underline{\sigma}} \cdot \underline{E}$ per Kirchhoff's formulation of Ohm's law. Then, taking $\underline{J}$ to represent the driving current discussed in Section 5.3, Maxwell's equations are written

$$\frac{\partial}{\partial t}\underline{B} = -\nabla \times \underline{E} \qquad\qquad \underline{\underline{\epsilon}} \cdot \frac{\partial}{\partial t}\underline{E} = \frac{1}{\mu_0}\nabla \times \underline{B} - \underline{J} - \underline{\underline{\sigma}} \cdot \underline{E} \tag{5.12}$$

It is convenient to introduce shorthand for the curl of each field: $\underline{C} \equiv \nabla \times \underline{E}$ and $\underline{F} \equiv \nabla \times \underline{B} - \mu_0 \underline{J}$. Or, recalling Equation (5.6),

$$C^i = \frac{\varepsilon^{ijk}}{\sqrt{g}} \frac{\partial}{\partial u^j} E_k \qquad\qquad F^i = \frac{\varepsilon^{ijk}}{\sqrt{g}} \frac{\partial}{\partial u^j} B_k - J^i \tag{5.13}$$

In these terms, Faraday's law can simply be written:

$$\frac{\partial}{\partial t} B^i = -C^i \tag{5.14}$$

Writing each component out explicitly, and using the metric tensor (per Equation (5.5)) to eliminate contravariant magnetic field components[8], Equation (5.14) becomes:

$$\begin{aligned} B_1 &\leftarrow B_1 - g_{11}\,\delta t\, C^1 - g_{13}\,\delta t\, C^3 \\ B_2 &\leftarrow B_2 - g_{22}\,\delta t\, C^2 \\ B_3 &\leftarrow B_3 - g_{31}\,\delta t\, C^1 - g_{33}\,\delta t\, C^3 \end{aligned} \tag{5.15}$$

Note that the $\leftarrow$ operator is used in Equation (5.15) to indicate assignment, rather than equality. Terms on the left are new, while those on the right are old.

Unlike Faraday's law, Ampère's law cannot be trivially solved. Not only does the time derivative of $\underline{E}$ depend on its own future value, but the crosswise and azimuthal components of the equation are coupled by the Hall terms in the conductivity tensor. Fortunately, the electric tensor can be inverted, allowing a solution by integrating factors:

$$\underline{\underline{\epsilon}} \cdot \frac{\partial}{\partial t} \underline{E} = \frac{1}{\mu_0} \underline{F} - \underline{\underline{\sigma}} \cdot \underline{E} \qquad \text{becomes} \qquad \left(\underline{\underline{\Omega}} + \underline{\underline{\mathbb{I}}} \frac{\partial}{\partial t} \right) \cdot \underline{E} = \underline{\underline{V}}^2 \cdot \underline{F} \tag{5.16}$$

[8]Fields are stored only in terms of their covariant components, and curls in terms of their contravariant components. This reduces Tuna's memory footprint (since each field need not be stored twice) as well as its computational cost (since time need not be spent rotating between bases). As a result, Tuna's solutions to Maxwell's equations are linear expressions whose coefficients are a mishmash of physical constants and geometric factors. To save time, each coefficient is computed once and stored, rather than being multiplied out from scratch with each time step.

Where $\underline{\underline{\mathbb{I}}}$ is the identity tensor and in x-y-z coordinates[9],

$$\underline{\underline{V}}^2 \equiv \frac{1}{\mu_0}\underline{\underline{\epsilon}}^{-1} = \begin{bmatrix} v_A^2 & 0 & 0 \\ 0 & v_A^2 & 0 \\ 0 & 0 & c^2 \end{bmatrix} \quad \text{and} \quad \underline{\underline{\Omega}} \equiv \underline{\underline{\epsilon}}^{-1} \cdot \underline{\underline{\sigma}} = \begin{bmatrix} \frac{\sigma_P}{\epsilon_\perp} & \frac{-\sigma_H}{\epsilon_\perp} & 0 \\ \frac{\sigma_H}{\epsilon_\perp} & \frac{\sigma_P}{\epsilon_\perp} & 0 \\ 0 & 0 & \frac{\sigma_0}{\epsilon_0} \end{bmatrix} \tag{5.17}$$

Multiplying through by $\exp\big(\underline{\underline{\Omega}}\,t\big)$ and applying the product rule, Equation (5.16) becomes[10]

$$\frac{\partial}{\partial t}\Big(\exp\big(\underline{\underline{\Omega}}\,t\big) \cdot \underline{E}\Big) = \exp\big(\underline{\underline{\Omega}}\,t\big) \cdot \underline{\underline{V}}^2 \cdot \underline{F} \tag{5.18}$$

Equation (5.18) can then be integrated over a small time step δt and expressed in terms of the assignment operator introduced in Equation (5.15).

$$\underline{E} \leftarrow \exp\big(-\underline{\underline{\Omega}}\,\delta t\big) \cdot \underline{E} + \delta t\, \exp\big(-\underline{\underline{\Omega}}\,\tfrac{\delta t}{2}\big) \cdot \underline{\underline{V}}^2 \cdot \underline{F} \tag{5.19}$$

The tensor exponential is evaluated by splitting $\underline{\underline{\Omega}}$ into the sum of its diagonal and Hall components[11]. The Hall exponential condenses into sines and cosines, giving a rotation around the magnetic field line:

$$\underline{E} \leftarrow \exp\big(-\underline{\underline{\Omega}}'\,\delta t\big) \cdot \underline{\underline{R}}_z\Big(\tfrac{-\sigma_H \delta t}{\epsilon_\perp}\Big) \cdot \underline{E} + \delta t\, \exp\big(-\underline{\underline{\Omega}}'\,\tfrac{\delta t}{2}\big) \cdot \underline{\underline{R}}_z\Big(\tfrac{-\sigma_H \delta t}{2\epsilon_\perp}\Big) \cdot \underline{\underline{V}}^2 \cdot \underline{F} \tag{5.20}$$

Where

$$\underline{\underline{R}}_z(\theta) = \begin{bmatrix} \cos\theta & -\sin\theta & 0 \\ \sin\theta & \cos\theta & 0 \\ 0 & 0 & 1 \end{bmatrix} \quad \text{and} \quad \underline{\underline{\Omega}}' \equiv \begin{bmatrix} \frac{\sigma_P}{\epsilon_\perp} & 0 & 0 \\ 0 & \frac{\sigma_P}{\epsilon_\perp} & 0 \\ 0 & 0 & \frac{\sigma_0}{\epsilon_0} \end{bmatrix} \tag{5.21}$$

[9] Note the parallel component of the present definition of $\underline{\underline{\Omega}}$ differs slightly from that used in Chapter 4, due to the present chapter's neglect of inertial effects; see Chapter 6.

[10] Tensor exponentiation is analogous to scalar exponentiation[37]: $\exp\Big(\underline{\underline{T}}\Big) \equiv \sum_n \frac{1}{n!}\underline{\underline{T}}^n$.

[11] For tensors, $\exp\Big(\underline{\underline{S}} + \underline{\underline{T}}\Big) = \exp\Big(\underline{\underline{S}}\Big)\exp\Big(\underline{\underline{T}}\Big)$ as long as $\underline{\underline{S}} \cdot \underline{\underline{T}} = \underline{\underline{T}} \cdot \underline{\underline{S}}$.

The parallel component of term of Equation (5.20) is simply

$$E_z \leftarrow E_z \exp\left(\frac{-\sigma_0 \delta t}{\epsilon_0}\right) + c^2 \delta t F_z \exp\left(\frac{-\sigma_0 \delta t}{2\epsilon_0}\right) \tag{5.22}$$

Or, using Equation (5.7) to map to the covariant basis,

$$E_3 \leftarrow E_3 \exp\left(\frac{-\sigma_0 \delta t}{\epsilon_0}\right) + c^2 \delta t \left(g_{31} F^1 + g_{33} F^3\right) \exp\left(\frac{-\sigma_0 \delta t}{2\epsilon_0}\right) \tag{5.23}$$

Tuna's conductivity profile gives a minimum value of $\frac{\sigma_0 \delta t}{\epsilon_0}$ on the order of 10^3, making $\exp\left(\frac{-\sigma_0 \delta t}{\epsilon_0}\right)$ far too small to be stored in a double precision variable[12]. That is, this model takes E_3 (and, proportionally, E_z) to be uniformly zero. This issue is revisited in Chapter 6.

The perpendicular components of Equation (5.20) give the expressions:

$$\begin{aligned}
E_1 + \frac{g^{13}}{g^{11}} E_3 \leftarrow \quad & E_1 \cos\left(\frac{-\sigma_H \delta t}{\epsilon_\perp}\right) \exp\left(\frac{-\sigma_P \delta t}{\epsilon_\perp}\right) \\
& + E_2 \sin\left(\frac{-\sigma_H \delta t}{\epsilon_\perp}\right) \exp\left(\frac{-\sigma_P \delta t}{\epsilon_\perp}\right) \sqrt{\frac{g^{22}}{g^{11}}} \\
& + E_3 \cos\left(\frac{-\sigma_H \delta t}{\epsilon_\perp}\right) \exp\left(\frac{-\sigma_P \delta t}{\epsilon_\perp}\right) \frac{g^{13}}{g^{11}} \\
& + F^1 \cos\left(\frac{-\sigma_H \delta t}{2\epsilon_\perp}\right) \exp\left(\frac{-\sigma_P \delta t}{2\epsilon_\perp}\right) \frac{v_A^2 \delta t}{g^{11}} \\
& + F^2 \sin\left(\frac{-\sigma_H \delta t}{2\epsilon_\perp}\right) \exp\left(\frac{-\sigma_P \delta t}{2\epsilon_\perp}\right) \frac{v_A^2 \delta t}{\sqrt{g^{11} g^{22}}}
\end{aligned} \tag{5.24}$$

[12] Not coincidentally, $\frac{\sigma_0}{\epsilon_0}$ can also be written $\frac{\omega_P^2}{\nu}$. At the ionosphere, the collision frequency ν is fast compared to field line resonance timescales, but it's still slow compared to the plasma frequency.

and

$$
\begin{aligned}
E_2 \leftarrow & -E_1 \sin\left(\tfrac{-\sigma_H \delta t}{\epsilon_\perp}\right) \exp\left(\tfrac{-\sigma_P \delta t}{\epsilon_\perp}\right) \sqrt{\frac{g^{11}}{g^{22}}} \\
& + E_2 \cos\left(\tfrac{-\sigma_H \delta t}{\epsilon_\perp}\right) \exp\left(\tfrac{-\sigma_P \delta t}{\epsilon_\perp}\right) \\
& - E_3 \sin\left(\tfrac{-\sigma_H \delta t}{\epsilon_\perp}\right) \exp\left(\tfrac{-\sigma_P \delta t}{\epsilon_\perp}\right) \frac{g^{13}}{\sqrt{g^{11} g^{22}}} \\
& - F^1 \sin\left(\tfrac{-\sigma_H \delta t}{2\epsilon_\perp}\right) \exp\left(\tfrac{-\sigma_P \delta t}{2\epsilon_\perp}\right) \frac{v_A^2 \delta t}{\sqrt{g^{11} g^{22}}} \\
& + F^2 \cos\left(\tfrac{-\sigma_H \delta t}{2\epsilon_\perp}\right) \exp\left(\tfrac{-\sigma_P \delta t}{2\epsilon_\perp}\right) \frac{v_A^2 \delta t}{g^{22}}
\end{aligned}
\tag{5.25}
$$

The E_3 terms in Equations (5.24) and (5.25) can be ignored at present. They are revisited in Chapter 6.

It bears recalling that the driving current is defined as part of $\underline{F}$, per Equation (5.13). When the driving current is purely azimuthal ($J^1 = J^3 = 0$), the driving is in principle applied to both the poloidal and the toroidal electric fields through F^2. However, in practice, the driving applied to the toroidal electric field is vanishingly small. The driving current J^2 is localized around $5\,\mathrm{R_E}$ geocentric, and $\exp\left(\frac{-\sigma_P \delta t}{2\epsilon_\perp}\right)$ drops off quickly with altitude.

5.5 Boundary Conditions

Dirichlet and Neumann boundary conditions are applied to the electric field components and magnetic field components respectively. That is, electric fields are zero at the inner and outer boundaries, and magnetic fields normal to the inner and outer boundaries are zero.

These boundary conditions can in principle cause nonphysical reflections at the boundary[13]. In practice, however (with a noted exception in Chapter 7), wave activity is concentrated well within the simulation domain. Simulation results are robust under

[13] See, for example, the bottom row of Figure 5.4.

an exchange of Dirichlet and Neumann boundary conditions, though a self-inconsistent set of boundary condidtions (such as applying Neumann conditions to B_1 but Dirichlet conditions to B_3) quickly causes instability.

The Earthward boundary conditions are as follows.

Between the top of the neutral atmosphere and the bottom of the ionosphere, the model includes a thin, horizontal current sheet representing the ionosphere's E layer[58]. By integrating Ampère's law over the layer, it can be shown[27] that the horizontal electric field values at the edge of the grid are determined by the jump in the horizontal magnetic fields:

$$\underline{\underline{\Sigma}} \cdot \underline{E} = \frac{1}{\mu_0} \lim_{\delta r \to 0} \left[\hat{r} \times \underline{B} \right|_{R_I - \delta r}^{R_I + \delta r} \tag{5.26}$$

The integrated conductivity tensor $\underline{\underline{\Sigma}}$ is written in θ-ϕ coordinates as[58]:

$$\underline{\underline{\Sigma}} \equiv \begin{bmatrix} \frac{\Sigma_0 \Sigma_P}{\Sigma_0 \cos^2 \alpha + \Sigma_P \sin^2 \alpha} & \frac{-\Sigma_0 \Sigma_H}{\Sigma_0 \cos^2 \alpha + \Sigma_P \sin^2 \alpha} \\ \frac{\Sigma_0 \Sigma_H}{\Sigma_0 \cos^2 \alpha + \Sigma_P \sin^2 \alpha} & \Sigma_P + \frac{\Sigma_H^2 \sin^2 \alpha}{\Sigma_0 \cos^2 \alpha + \Sigma_P \sin^2 \alpha} \end{bmatrix} \tag{5.27}$$

Where α is the angle between the magnetic field and the vertical direction, given by $\cos\alpha \equiv \frac{-2\cos\theta}{\sqrt{1+3\cos^2\theta}}$, and Σ_P, Σ_H, and Σ_0 are the height-integrated Pedersen, Hall, and parallel conductivities respectively. Their values are determined by integrating Kelley's[47] conductivity profiles from Earth's surface to the ionospheric boundary; values are shown in Table 5.2.

Table 5.2: Integrated Atmospheric Conductivity (S)

	Σ_0	Σ_P	Σ_H
Active Day	424	0.65	6.03
Quiet Day	284	0.44	4.02
Active Night	9	0.01	0.12
Quiet Night	9	0.01	0.12

The atmospheric conductivities of the two nightside profiles are the same, though the profiles differ significantly at higher altitudes, as shown in Section 5.2.

An expression for the horizontal electric fields at the boundary is obtained by inverting Equation (5.26). After mapping to covariant coordinates per Equation (5.8), and taking $\Sigma \equiv \det \underline{\underline{\Sigma}}$,

$$\begin{aligned} E_1 &\leftarrow \frac{1}{\mu_0 \Sigma} \lim_{\delta r \to 0} \left[\qquad -\Sigma_{\theta\phi} B_1 - \sqrt{\frac{g_{11}}{g_{22}}} \Sigma_{\phi\phi} B_2 \right|_{R_I - \delta r}^{R_I + \delta r} \\ E_2 &\leftarrow \frac{1}{\mu_0 \Sigma} \lim_{\delta r \to 0} \left[\sqrt{\frac{g_{22}}{g_{11}}} \Sigma_{\theta\theta} B_1 + \qquad \Sigma_{\phi\theta} B_2 \right|_{R_I - \delta r}^{R_I + \delta r} \end{aligned} \tag{5.28}$$

The atmospheric field is computed in terms of a scalar magnetic potential, Ψ, such that $\underline{B} = \nabla \Psi$. The neutral atmosphere is considered to be a perfect insulator, giving $\nabla \times \underline{B} = 0$. Combined with $\nabla \cdot \underline{B} = 0$ (per Maxwell's equations), this ensures that Ψ satisfies Laplace's equation, $\nabla^2 \Psi = 0$, and thus can be written as a sum of harmonics.

Laplace's equation can be solved analytically; however, a numerical solution is preferrable to ensure orthonormality on a discrete and incomplete[14] grid. After separating out the radial and azimuthal dependence in the usual way, the latitudinal component of Laplace's equation is written in terms of $s \equiv -\sin^2 \theta$:

$$\left(4s^2 + 4s\right) \frac{d^2}{ds^2} Y_\ell + (4 + 6s) \frac{d}{ds} Y_\ell - \frac{m^2}{s} Y_\ell = \ell \left(\ell + 1\right) Y_\ell \tag{5.29}$$

Using centered differences to linearize the derivatives, Equation (5.29) becomes a system of coupled linear equations, one per field line. It is then solved numerically for eigenvalues $\ell \left(\ell + 1\right)$ and eigenfunctions Y_ℓ[15]. In terms of the harmonics Y_ℓ, the magnetic potential between the Earth's surface and the top of the atmosphere is written using

[14] As discussed in Section 5.1, the grid is constrained to finite L, which excludes the equator as well as the poles.

[15] Solving Laplace's equation analytically results in spherical harmonics indexed by both ℓ and m, the separation constants for θ and ϕ respectively. In two and a half dimensions, ϕ is not explicitly resolved, so m is set manually.

coefficients a_ℓ and b_ℓ:

$$\Psi = \sum_\ell \left(a_\ell \, r^\ell + b_\ell \, r^{-\ell-1} \right) Y_\ell \tag{5.30}$$

As a boundary condition for Ψ, Earth is assumed to be a perfect conductor. This forces the magnetic field at Earth's surface to be horizontal; that is, $B_r = \frac{\partial}{\partial r}\Psi = 0$. Noting that solutions to Laplace's equation are orthonormal, each element of the sum in Equation (5.30) must be independently zero at R_E. This allows the coefficients a_ℓ and b_ℓ to be expressed in terms of one another.

$$b_\ell = \frac{\ell}{\ell + 1} R_E^{2\ell+1} a_\ell \tag{5.31}$$

The current sheet at the top of the atmosphere is assumed to be horizontal, so the radial component of the magnetic field must be the same just above and just below it. Taking the radial derivative of Equation (5.30) at the top of the atmosphere, and eliminating b_ℓ with Equation (5.31), gives

$$B_r = \sum_\ell \ell \, a_\ell \, R_I^{\ell-1} \left(1 - \lambda^{2\ell+1} \right) Y_\ell \qquad \text{where} \qquad \lambda \equiv \frac{R_E}{R_I} \sim 0.975 \tag{5.32}$$

The summation is collapsed by "integrating" over a harmonic[16]. Inverse harmonics are obtained by inverting the eigenvector matrix. Then $Y_\ell \cdot Y_{\ell'}^{-1} = \delta_{\ell\ell'}$ by construction.

$$a_\ell = \frac{1}{\ell \, R_I^{\ell-1}} \frac{B_r \cdot Y_\ell^{-1}}{1 - \lambda^{2\ell+1}} \tag{5.33}$$

Combining Equations (5.30), (5.31), and (5.33) allows the expression of Ψ at the top and bottom of the atmosphere as a linear combination of radial magnetic field components

[16] Because the functions are defined on a discrete grid, their inner product is not an integral, but a sum: $B_r \cdot Y_\ell^{-1} \equiv \sum_i B_r[i] \, Y_\ell^{-1}[i]$.

at the bottom of the ionosphere.

$$\begin{aligned}
\Psi_E &= \sum_\ell Y_\ell \, \frac{R_I}{\ell\,(\ell-1)} \frac{(2\ell-1)\,\lambda^\ell}{1-\lambda^{2\ell+1}} B_r \cdot Y_\ell^{-1} \\
\Psi_I &= \sum_\ell Y_\ell \, \frac{R_I}{\ell\,(\ell-1)} \frac{(\ell-1)+\ell\,\lambda^{2\ell+1}}{1-\lambda^{2\ell+1}} B_r \cdot Y_\ell^{-1}
\end{aligned} \tag{5.34}$$

Horizontal magnetic fields are obtained by taking derivatives of Ψ.

$$B_1 = \frac{\partial}{\partial u^1}\Psi \qquad\qquad B_2 = \frac{\partial}{\partial u^2}\Psi \tag{5.35}$$

Horizontal magnetic field values at the top of the atmosphere are used to impose boundary conditions on the electric fields at the bottom of the ionosphere, per Equation (5.28). Those at Earth's surface are valuable because they allow a direct comparison between model output and ground magnetometer data, after being mapped to physical coordinates per Equation (5.8).

Chapter 6

Electron Inertial Effects

As laid out in Chapter 5, Tuna resolves neither currents nor electric fields parallel to the background magnetic field. This is unfortunate; parallel electric fields generated by kinetic and inertial Alfvén waves (including fundamental field line resonances[77, 93]) are a topic of particular interest in the study of auroral particle precipitation.

Parallel currents and electric fields can be added to Tuna through the consideration of electron inertial effects in Ohm's law:

$$0 = \sigma_0 E_z - J_z \qquad \text{becomes} \qquad \frac{1}{\nu}\frac{\partial}{\partial t} J_z = \sigma_0 E_z - J_z \tag{6.1}$$

With the addition of the electron inertial term, it is necessary to track the parallel current independent of the parallel electric field[1]. Solving by integrating factors[2] gives

$$J_3 \leftarrow J_3 \, \exp(-\nu\delta t) + \delta t \, \frac{ne^2}{m_e} E_3 \, \exp\!\left(-\nu \tfrac{\delta t}{2}\right) \tag{6.2}$$

[1]The parallel current J_z is defined on the same points of the Yee grid as E_z. It is offset in time by half of a time step.

[2]The integrating factors technique is laid out explicitly for Ampère's law in Section 5.4.

From there, the parallel electric field can be updated directly; Equation (5.23) is replaced by the following:

$$E_3 \leftarrow E_3 + c^2 \delta t \, \left(g_{31} F^1 + g_{33} F^3 \right) - \frac{\delta t}{\epsilon_0} J_3 \tag{6.3}$$

The present section explores the complications that arise from the addition of the electron inertial term to Ohm's law, as well as a few results that may be gleaned despite those complications. Notably — for reasons discussed in Section 6.3 — the results presented in Chapter 7 do not make use of the effects of electron inertia.

Inertial effects have been considered in previous numerical work, such as by Lysak and Song in 2001[60], but never at the global scale. That work considered waves in the ionospheric Alfvén resonator, with frequencies of hundreds of mHz, and did not account for the effects of the dipolar geometry. In fact, in that work, circular polarization (essentially a superposition of poloidal and toroidal modes) was noted to be a promising avenue for future work.

6.1 The Boris Factor

With the addition of the electron inertial term, a cyclical dependence appears between Ampère's law and Ohm's law:

$$\frac{\partial}{\partial t} E_z \sim -\frac{1}{\epsilon_0} J_z \qquad \text{and} \qquad \frac{\partial}{\partial t} J_z \sim \frac{n e^2}{m_e} E_z \qquad \text{so} \qquad \frac{\partial^2}{\partial t^2} E_z \sim -\omega_P^2 E_z \tag{6.4}$$

That is, electron inertial effects come hand in hand with the plasma oscillation.

As mentioned in Chapter 4 and shown in Figure 6.1, plasma oscillation is quite fast — several orders of magnitude smaller than Tuna's time step as determined in Section 5.1 ($\sim$10 µs). This poses a conundrum. At Tuna's usual time step, the plasma oscillation becomes unstable within seconds[3]. On the other hand, reducing the time step by three

[3] For stability, $\omega_P \delta t < 1$ is necessary.

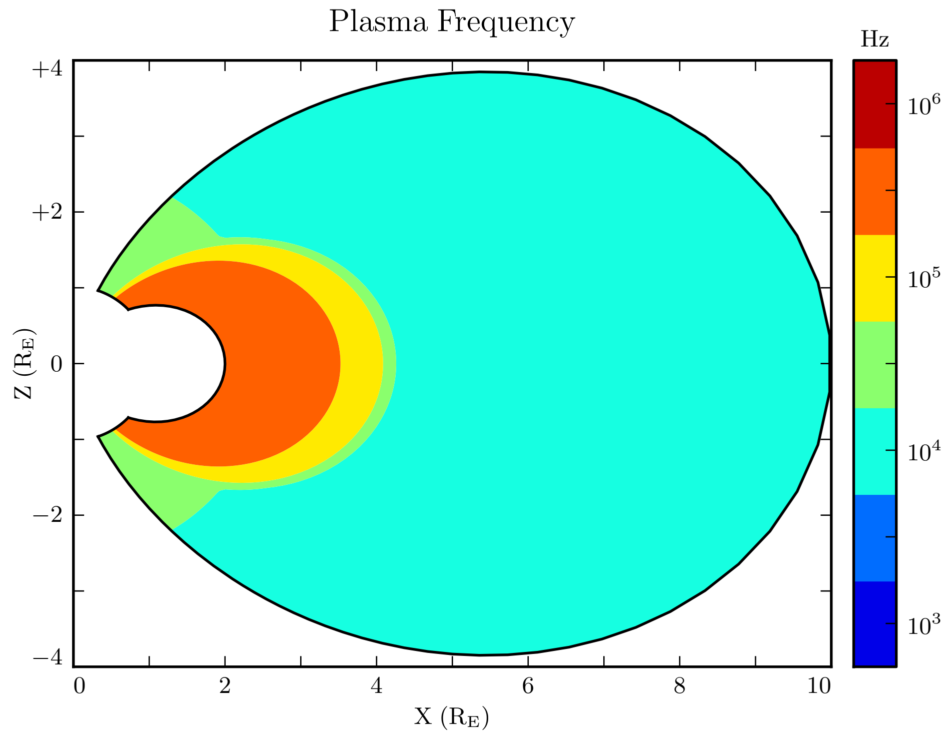

Figure 6.1: The plasma frequency reaches a peak value just under 10^6 Hz near the equator. Outside the plasmasphere, its value is closer to 10^4 Hz, which is still not well-resolved by Tuna's usual time step.

orders of magnitude to resolve the plasma oscillation is computationally infeasible; a run slated for an hour would require six weeks to complete.

As it happens, this problem can be solved by artificially increasing the parallel electric constant above its usual value of ϵ_0. Doing so lowers both the speed of light and the plasma frequency within the simulation. This technique — and others like it — has been widespread in numerical modeling since it was presented by Boris in 1970[6]. The following paraphrases an argument by Lysak and Song[60], outlining its validity specifically in the case of electron inertial effects.

Supposing that the current and electric field are oscillating at frequency ω, the parallel components of Ampère's law and Ohm's law can be written

$$-i\omega\epsilon_0 E_z = \frac{1}{\mu_0}\left(\nabla\times\underline{B}\right)_z - J_z \qquad\qquad -\frac{i\omega}{\nu}J_z = \sigma_0 E_z - J_z \tag{6.5}$$

Then, eliminating the current, the parallel electric field can be related to the curl of the magnetic field by[4]

$$\left(1 - \frac{\omega^2 - i\nu\omega}{\omega_P^2}\right)E_z = \frac{c^2}{\omega_P^2}\left(\nu - i\omega\right)\left(\nabla\times\underline{B}\right)_z \tag{6.6}$$

In Equation (6.6), $\frac{c}{\omega_P}$ is the electron inertial length. While the speed of light and the plasma frequency each depend on ϵ_0, their ratio does not. This allows an estimation of how much the model should be affected by an artificially-large electric constant (and thus an artificially-small plasma frequency). So long as $\frac{\omega^2 - i\nu\omega}{\omega_P^2}$ remains small compared to unity, the model should behave physically.

For waves with periods of a minute or so, even perhaps-implausibly large Boris factors are allowed; for example, increasing ϵ_0 by a factor of 10^6 gives $\left|\frac{\omega^2 + i\omega\nu}{\omega_P^2}\right| \lesssim 0.01$.

6.2 Parallel Currents and Electric Fields

As discussed in Section 4.4, parallel electric fields in this regime are expected to be at least six orders of magnitude smaller than the perpendicular electric fields. Numerical results show general agreement: in Figure 6.2, the parallel electric field appears comparable to its perpendicular counterparts only after its been scaled up by a factor of 10^6.

As such, the inclusion of electron inertial effects does not appreciably impact the simulation's gross behavior. In Faraday's law, $\nabla\times\underline{E}$ is unaffected, to the extent that side-by-side magnetic field snapshots with and without electron inertial effects are not visibly distinguishable (not shown). In a sense, this is reassuring. It ensures that the

[4]From Equation (4.4), $c^2 \equiv \frac{1}{\mu_0\epsilon_0}$ and $\sigma_0 \equiv \frac{ne^2}{m_e\nu}$ and $\omega_P^2 \equiv \frac{ne^2}{m_e\epsilon_0}$.

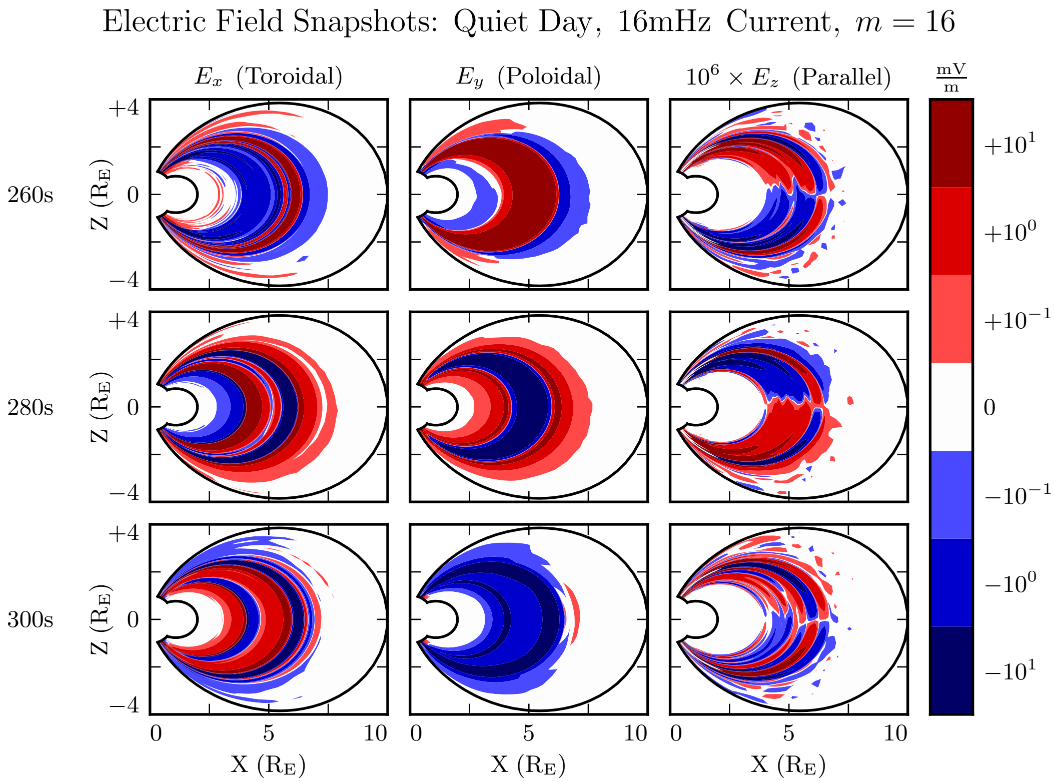

Figure 6.2: Parallel electric fields are smaller than perpendicular electric fields by about six orders of magnitude. As a result, parallel electric fields do not contribute significantly to $\nabla \times \underline{E}$ in Faraday's law.

present section does not cast doubt on the results presented in Chapter 7, where electron inertial effects are neglected.

Even if there is no significant feedback through Faraday's law, it's informative to consider the structures that arise in parallel currents and electric fields driven by perturbations in the ring current. For example, in Figure 6.2, the parallel electric field perturbation (with maxima near the ionosphere) exhibits the opposite harmonic structure to the perpendicular electric field components (which peak near the equator).

Figure 6.3 shows how parallel currents lines up with the Poynting flux over time. Four runs are shown, one per row. The horizontal axis is time, and the vertical axis is latitude. The real and imaginary components of the parallel current are shown in the first and third columns respectively, while the second and fourth columns show the poloidal and toroidal Poynting flux. Values are taken at an altitude of 1000 km.

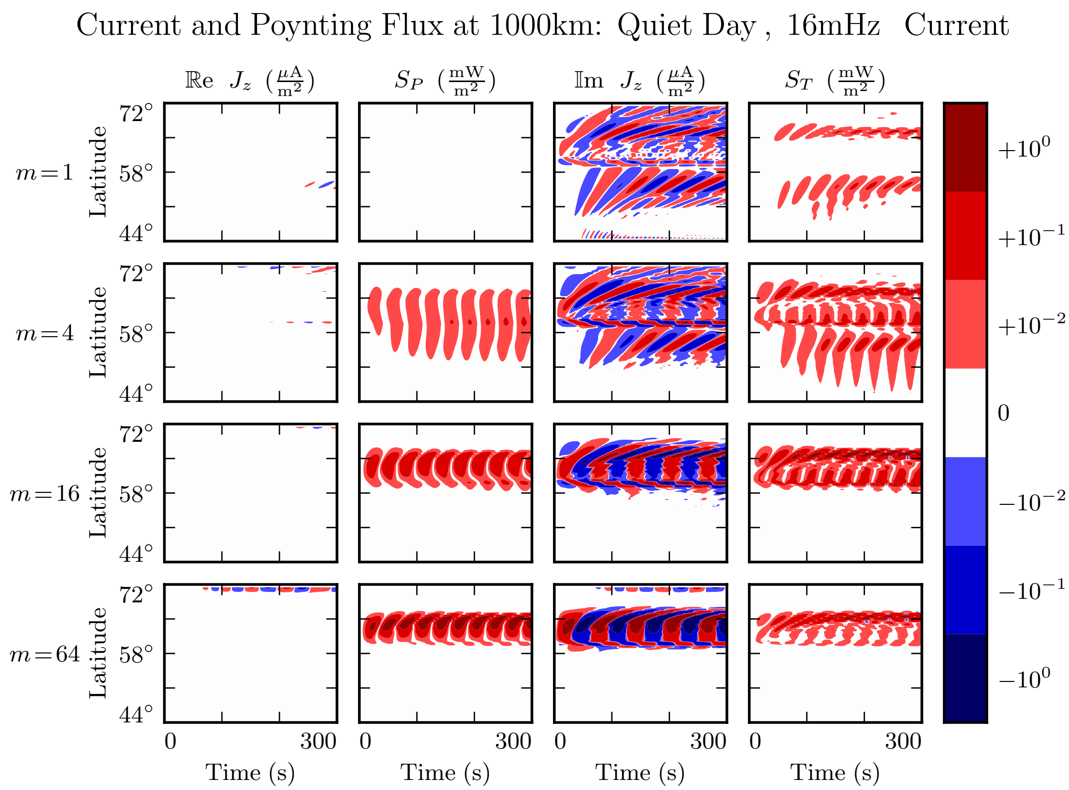

Figure 6.3: Parallel current and Poynting flux is shown for four runs, one per row, measured at an altitude of 1000 km. The parallel current is overwhelmingly imaginary, which implies a connection to the toroidal mode. Appropriately enough, the structure of the parallel current (particularly at low modenumber) seems to resemble the structure of the toroidal mode more than it does that of the poloidal mode. This is likely because the toroidal mode, with its sharp gradients across L-shells, dominates $(\nabla \times \underline{B})_z$.

Poloidal and toroidal fields are overwhelmingly real and imaginary respectively, because they are separated from one another by an azimuthal derivative (which carries a factor of i). However, when a wave's polarization is rotated by the Hall conductivity, there is no accompanying rotation in the complex plane — this gives rise to an imaginary component of the poloidal wave and a real component of the toroidal wave.

In Figure 6.3, the ionospheric conductivity is small, so the imaginary component of the parallel current dominates. This implies a connection between the parallel current and the toroidal mode, and indeed, the two do exhibit qualitatively similarities. At $m = 4$ in particular, the poloidal and toroidal Poynting fluxes are similar in strength much of the time, yet the form of the parallel current strongly resembles that of the toroidal Poynting flux over the poloidal.

The toroidal mode's dominant effect on the parallel current at small m is not surprising. As shown in Figure 6.2, toroidal waves vary sharply in L[5]. When the poloidal and toroidal magnetic fields are comparable in magnitude, $\frac{\partial}{\partial x} B_y$ typically exceeds $\frac{\partial}{\partial y} B_x$ (at least for $m \lesssim 32$).

Whereas the imaginary component of the parallel current corresponds to that carried into the ionosphere by Alfvén waves, its real component comes from electric fields rotated by the Hall conductivity. Figure 6.4 shows the same four runs as Figure 6.3, but measured at 100 km, the Earthward boundary of the simulation. At that point, the real and imaginary components are similar in magnitude.

In Figure 6.4, as in Figure 6.3, the imaginary component of the parallel current preferentially follows the toroidal Poynting flux. This is particularly apparent at $m = 16$, where the poloidal Poynting flux is clearly stronger, yet the structure of the imaginary current resembles that of the toroidal Poynting flux. The real parallel current, on the other hand, appears to follow the poloidal Poynting flux.

Put another way, low-m poloidal waves seem to primarily give rise to field-aligned currents only after being rotated to the toroidal mode by the Hall conductivity. At high modenumber, the two modes contribute comparably to the formation of parallel currents.

It's also possible to consider the effect of parallel currents and electric fields on the ionosphere's energy budget, per Poynting's theorem:

$$\frac{\partial}{\partial t} u = -\nabla \cdot \underline{E} - \underline{J} \cdot \underline{E} \tag{6.7}$$

[5]The sharp definition in L of the toroidal mode compared to the poloidal mode is also the topic of significant discussion in Chapter 7.

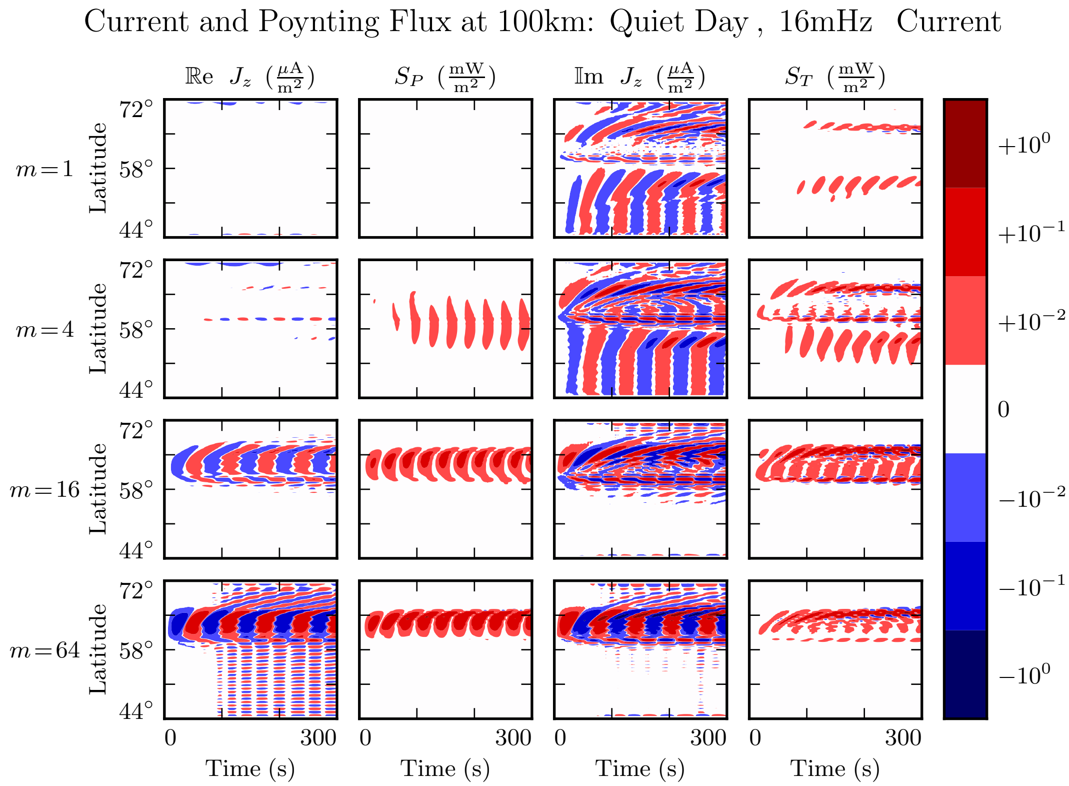

Figure 6.4: The above slices are taken from the same runs shown in Figure 6.3, but at an altitude of 100 km instead of 1000 km. The primary difference between the two altitudes is the strength of the ionospheric Hall conductivity, which directly couples the poloidal and toroidal modes. The Hall-rotated fields give rise to a real component of the parallel current, the structure of which follows the poloidal Poynting flux (as it rotates to the toroidal mode).

The magnitude of the parallel current tops out over 1 $\mu\mathrm{A}/\mathrm{m}^2$, just shy of the up-to-tens of $\mu\mathrm{A}/\mathrm{m}^2$ inferred from ground observations and seen in situ[8, 45, 80]. However, this current is not a significant contributor to ionospheric Joule dissipation. As shown in Figure 6.5, the energy deposited in the ionosphere by the Poynting flux matches closely with the energy lost to Joule dissipation — as it should, to conserve energy. But, according to the model, Pedersen and Hall are dominant. The parallel component of $\underline{J} \cdot \underline{E}$ is smaller by several orders of magnitude.

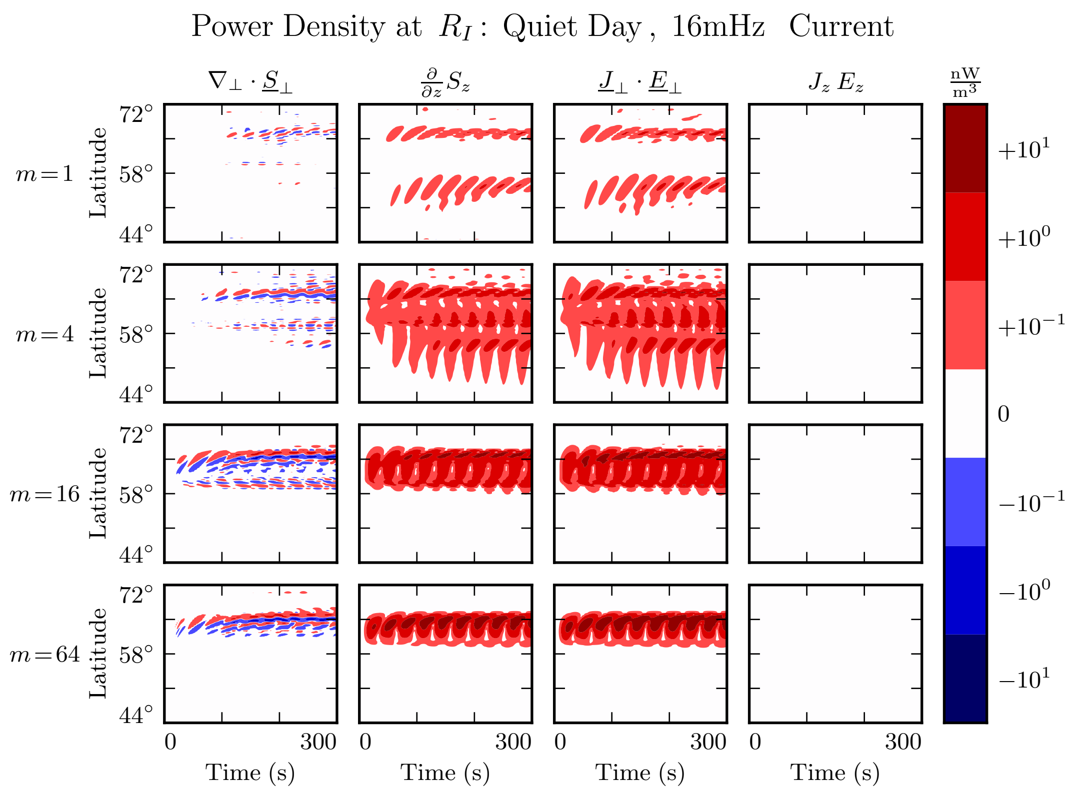

Figure 6.5: While field-aligned currents can be of significant size, they are not particularly good at depositing energy in the ionosphere. Energy deposited by the Poynting flux matches closely with Joule dissipation from the perpendicular currents, while $J_z E_z$ is smaller by several orders of magnitude.

6.3 Inertial Length Scales

It's not quite fair to compare the parallel and perpendicular contributions to $\nabla \times \underline{E}$ as is done in Section 6.2. Perpendicular electric fields are on the order of $1\,\text{mV/m}$, with wavelengths on the order of $10^5\,\text{km}$; they cause magnetic fields to change at a rate of around $0.1\,\text{nT/s}$. Parallel electric fields, closer to $10^{-6}\,\text{mV/m}$, would need to vary over length scales of $0.1\,\text{km}$ to match with that.

Such scales are believable. The characteristic length scale of the plasma oscillation is the electron inertial length, $\frac{c}{\omega_P}$, which is on the order of $1\,\text{km}$ in the auroral ionosphere and

0.1 km in the low-altitude plasmasphere. However, Tuna's grid out bottoms out closer to 10 km. That is, with the inclusion of electron inertial effects, the grid is too coarse to resolve all of the waves expected to be present. The model is prone to instability as a result — for example, "wigglies" are visible in the bottom-left subplot of Figure 6.4.

Figure 6.6 shows a run with perpendicular resolution smaller than the electron inertial length, side by side with an analogous run on the typical grid described in Chapter 5. In order to carry out the inertial-scale run, several concessions were made to computational cost. The run simulates only a duration of 100 s (other figures in the present chapter, and those in Chapter 7, show 300 s), and the grid covers only the auroral latitudes from $L = 5$ to $L = 7$.

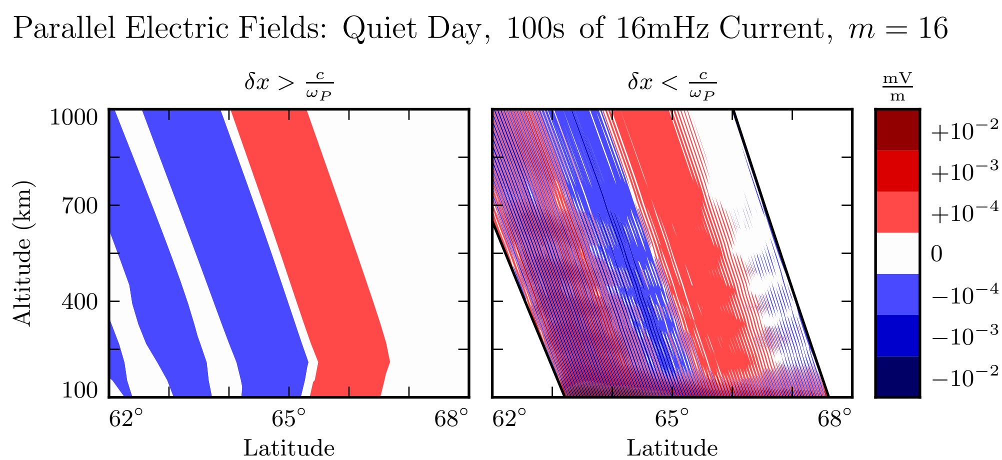

Figure 6.6: The parallel electric field develops significant structure when the perpendicular grid resolution is smaller than the electron inertial length. Unfortunately, such runs are prohibitively expensive. The subplot on the right — which still fails to resolve wave structure properly — represents a 100-fold increase in computational time compared to that on the left.

Even so, the run presents a significant computational expense. Spread over 16 cores, a 100 s run on Tuna's usual grid takes well under an hour. The inertial-scale run barely finished in 96 hours, the cutoff at the Minnesota Supercomputing Institute. This is because runtime goes as the inverse square of grid resolution; not only does finer resolution require more grid cells, but it also gives rise to proportionally smaller crossing times, imposing a smaller time step.

The snapshot shown in Figure 6.6 uses a perpendicular grid resolution of 0.7 km at the Earthward edge, which just satisfies the Nyquist rate for the minimum inertial length of 1.7 km. It's still too coarse. There is clearly some small-scale structure developing in the ionosphere, but it's not well resolved. The large number of "wigglies" portends an imminent crash.

6.4 Discussion

The present chapter is a proof of concept: the addition of electron inertial effects to Tuna presents a promising first-principles-based approach to the investigation of parallel currents and electric fields associated with field line resonances. Electric fields arise which are consistent in magnitude with those predicted by the dispersion relation, and parallel currents fall within an order of magnitude or so of observed values, even when inertial length scales are not properly resolved.

Results in Section 6.2 suggest a disparity between low-m poloidal and toroidal FLRs in terms of the parallel current response. At low altitude, where the two modes are directly coupled by the Hall conductivity, both seem to be accompanied by parallel currents. However, in regions of low Hall conductivity, parallel currents appear to preferrentially accompany toroidal waves. This is likely a result of the toroidal mode's sharp gradients across L-shells.

Future work could consider the relationship between the dynamic height-integrated potentials and the accompanying parallel currents, specifically with respect to the Knight relation[50]. Inertial effects could also be accompanied by test particles, in order to gauge the precipitation that would be expected to accompany global Alfvénic potential structures.

Unfortunately, simulations are prone to instability when inertial length scales are not properly resolved. And, at least at present, resolving those scales poses a prohibitive computational expense. For this reason, the consideration of inertial effects is limited to the present chapter; results in Chapter 7 make use of the core version of Tuna presented in Chapter 5, which does not include the effects of electron inertia.

Notably, the addition or omission of parallel currents and electric fields does not appear to significantly alter the behavior of perpendicular electric fields or magnetic fields. Because the parallel electric fields are relatively small, $\nabla \times \underline{E}$ is essentially unaffected by their inclusion. Joule dissipation from parallel currents also does not seem to be a significant in comparison to that from Pedersen and Hall currents.

Chapter 7

Numerical Results

A primary motivation for the development of Tuna is the fact that FLRs vary in interesting ways as a function of azimuthal modenumber, and that existing numerical models are limited in their ability to examine such behaviors. The present chapter discusses the core results that the model has so far produced.

7.1 Modenumber and Compression

It's well known that the poloidal FLR mode is compressional at low modenumber, but guided at high modenumber. However, the relationship is not well quantified. Theoretical work has historically been concerned with the limits $m \to 0$ and $m \to \infty$[14, 76], and only a handful of satellite observations have explicitly considered an event's azimuthal modenumber[17, 68, 88]. Using results from Tuna, the present section examines the strength of the poloidal wave's compressional component at an ensemble of finite modenumbers.

Figures 7.1 and 7.2 show magnetic field snapshots taken from a pair of runs; the first uses a small azimuthal modenumber, and the second uses a large one. The runs are otherwise identical: both simulations use the quiet dayside ionospheric profile, and both are driven at 22 mHz.

The differences between the two runs are striking. At low modenumber, wave activity is visible throughout the simulation domain. Structure in the poloidal magnetic field is only vaguely governed by the dipole geometry, and the compressional magnetic field is comparably strong to the two perpendicular components.

In contrast, at high modenumber, the poloidal magnetic field is localized to $L \sim 5$, where the driving is delivered. The compressional field is weaker than the poloidal field by at least an order of magnitude. A third-harmonic poloidal mode is visible at the outer boundary — its magnitude is just barely large enough to be visible on the logarithmic scale. The gap between $L \sim 5$ (where 22 mHz matches a first-harmonic FLR) and $L \sim 10$ (where 22 mHz matches a third-harmonic FLR) speaks to the evanescence of non-guided waves above the compressional Alfvén cutoff frequency[1].

In both the low-m and high-m runs, toroidal activity is more or less coincident with poloidal activity — as is to be expected, since the driving is purely poloidal, and so the poloidal mode must be the source of the toroidal mode. It is further notable that the toroidal mode is sharply guided. Particularly in Figure 7.2, strong, narrow, toroidal FLRs of opposite phase can be seen oscillating very close to one another. Strong poloidal waves, in contrast, are smeared in L.

Snapshots are not shown for runs carried out using the other ionospheric profiles (active day, quiet night, and active night). The morphology of their waves is qualitatively similar. The differences between the profiles is considered in Sections 7.2 to 7.4.

Figure 7.3 quantifies the compressional component of the poloidal mode as a function of modenumber. Each subplot corresponds to a different run of Tuna; the runs shown in Figures 7.1 and 7.2 are in the rightmost column, second from the top and second from the bottom respectively. The red line indicates the ratio between the RMS compressional magnetic field and the RMS poloidal magnetic field; both averages are taken over the entire simulation “volume” each time step. Mean values are shown in black.

At $m = 1$, the compressional and poloidal magnetic fields are comparable in magnitude. As m increases, however, the compressional component quickly falls off. The compressional component is half the strength of the poloidal component at $m \sim 5$, and a quarter

[1] See Section 4.4.

by $m \sim 10$. Similar behavior is seen using the active dayside and active nightside profiles (not shown). On the quiet nightside (not shown), the compressional component of the poloidal mode does not fall off quite as sharply; $\left|\frac{B_z}{B_x}\right|$ falls to 50 % at $m \sim 8$ and to 25 % at $m \sim 16$.

A slight frequency dependence is apparent across each row in Figure 7.3. Compressional coupling falls off slower for waves at higher frequency. This is because higher-frequency waves are that much closer to the cutoff frequency, and so their propagation across L-shells is that much less evanescent.

Notably, the waves considered in the present work are fundamental harmonics. The compressional behavior of the poloidal mode may vary for the (more-common) second harmonic: Radoski suggests that the asymptotic value of $\left|\frac{B_z}{B_x}\right|$ is inversely proportional to the harmonic number[76].

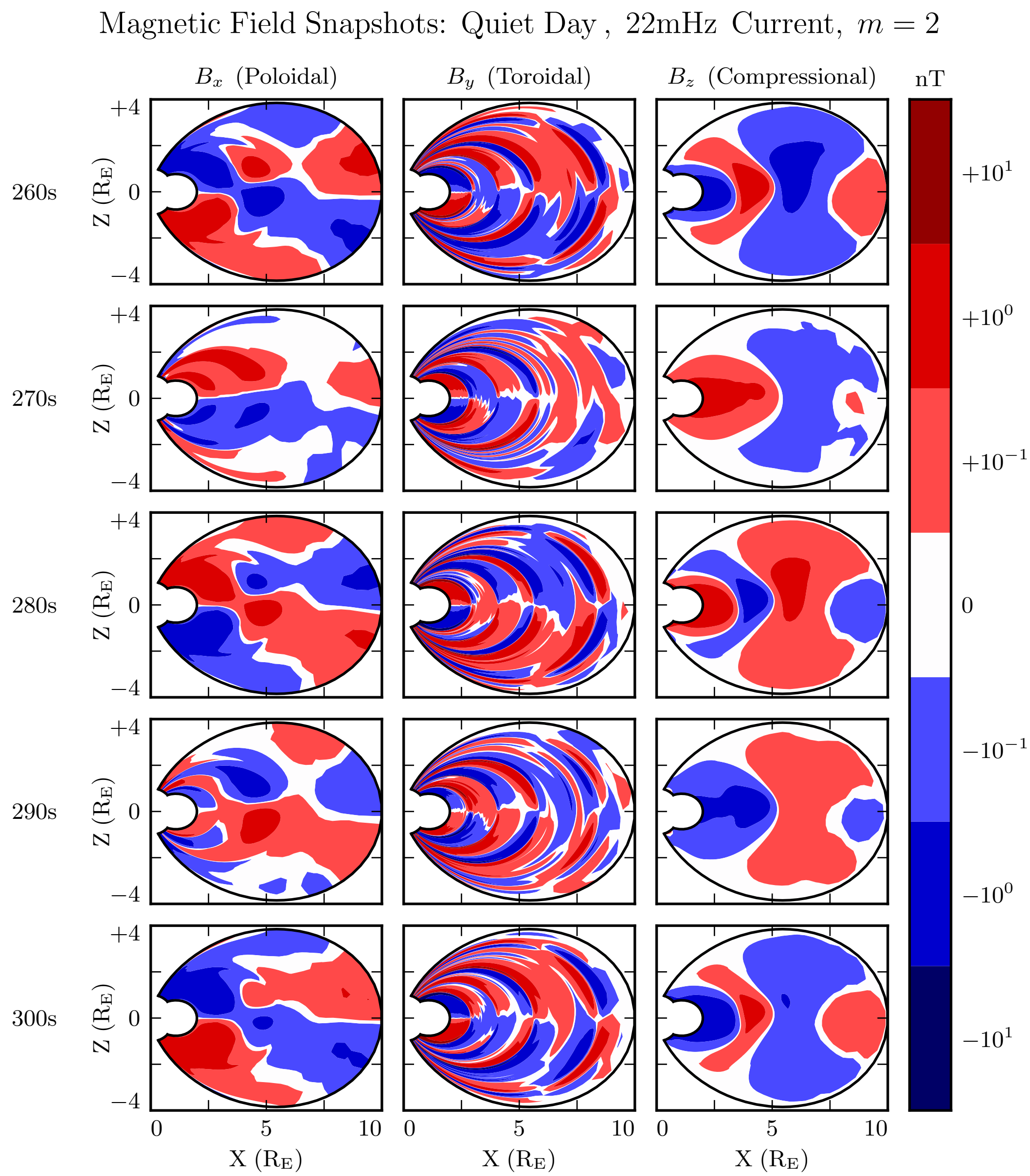

Figure 7.1: Each row in the above figure is a snapshot in time. The three columns show the simulated poloidal, toroidal, and compressional magnetic fields. Due to the run's low azimuthal modenumber, the poloidal mode has a significant compressional component. This is visible both in the fact that B_z is comparable in size to B_x, and in that structure in B_x is only vaguely guided by the geometry of the magnetic field. Toroidal waves, in contrast, are sharply guided.

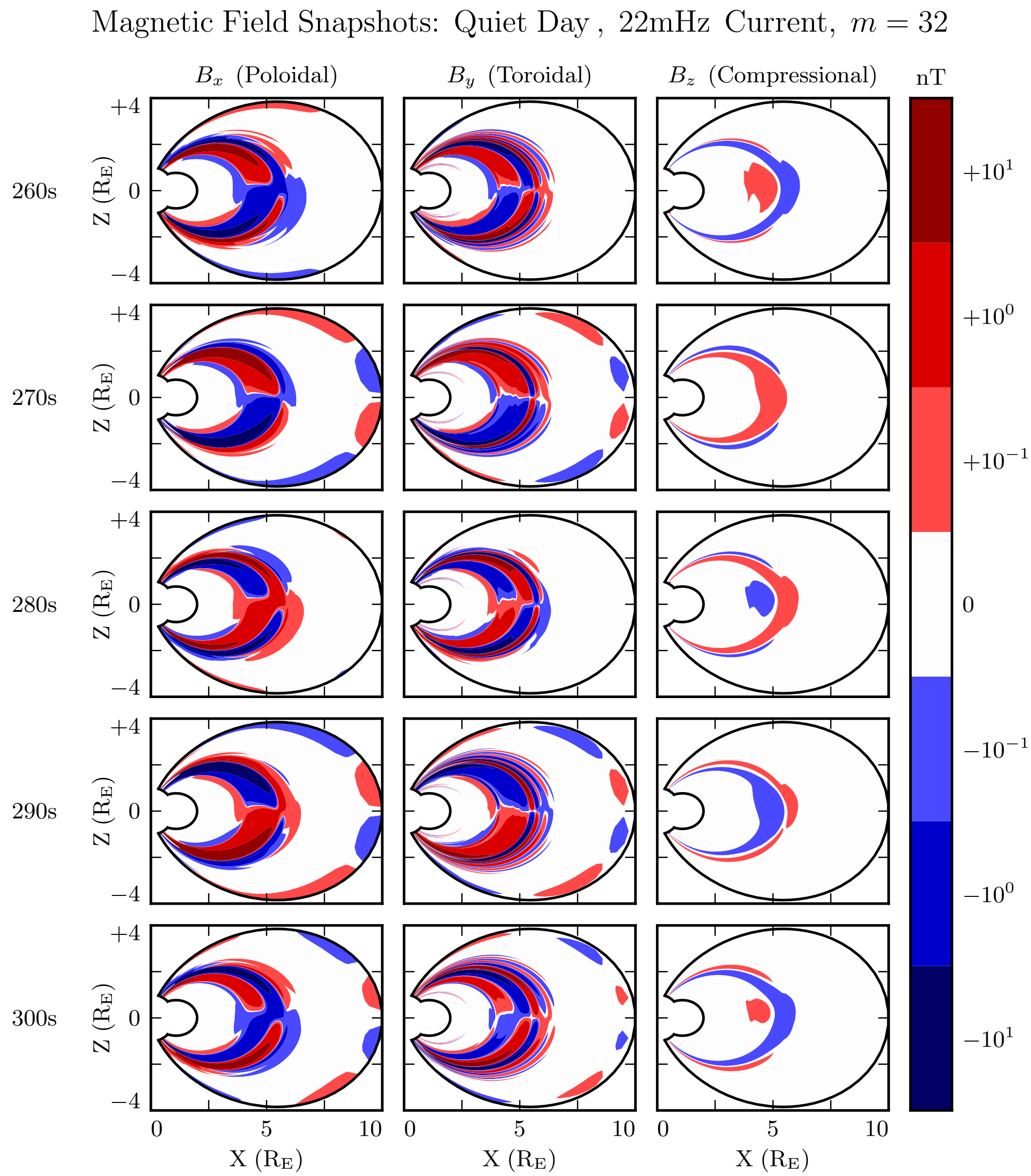

Figure 7.2: The above figure is analogous to Figure 7.1, but the run uses a large azimuthal modenumber. The change has a dramatic effect. The poloidal wave is concentrated much more sharply in L, and its compressional component is weakener by an order of magnitude. Regardless of modenumber, toroidal waves exist at a range of L shells similar to poloidal waves, and show sharp definition across L-shells.

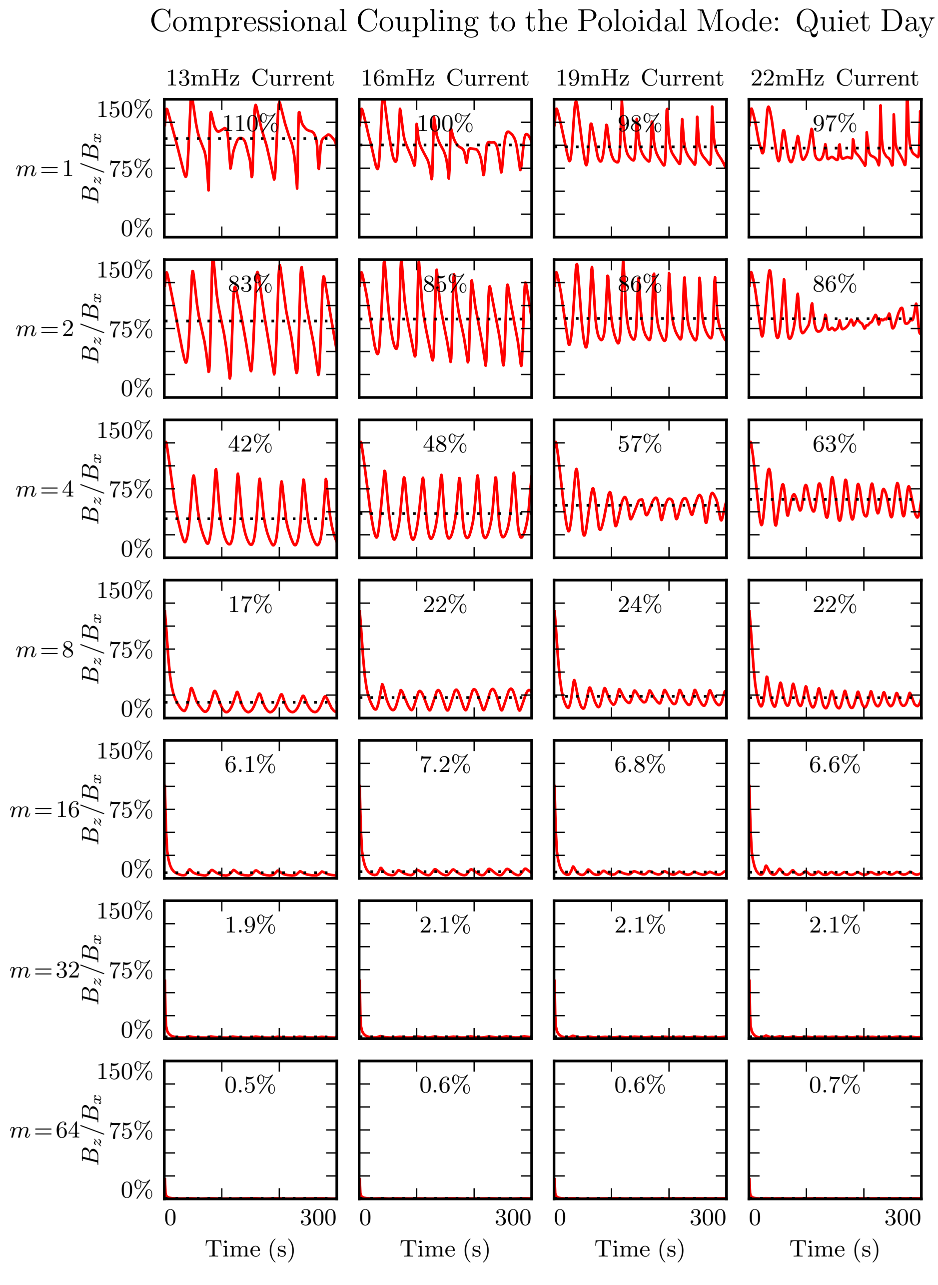

Figure 7.3: Each subplot above corresponds to a different run; the runs shown in Figures 7.1 and 7.2 are in the rightmost column, second from the top and second from the bottom respectively. Red lines indicate the ratio between the RMS compressional and poloidal magnetic fields. Mean values are shown in black. The compressional field is comparable to the poloidal field at $m = 1$, but falls quickly.

7.2 Resonance and Rotation on the Dayside

In his 1974 paper, Radoski argues that a poloidally-polarized wave should asymptotically rotate to the toroidal polarization[76] as a result of the curved derivative in the meridional plane. The question of finite poloidal lifetimes is considered further in a 1995 paper by Mann and Wright[64], using a straightened field line and an Alfvén speed gradient in the "radial" direction. They also found a rotation over time from poloidal to toroidal polarization, with the characteristic time proportional to the azimuthal modenumber.

The present section builds on the aforementioned results by relaxing several of their non-physical assumptions. Tuna's geometry is more realistic than Radoski's half-cylinder or the box model usede by Mann and Wright. Previous work has considered the evolution of an initial condition, while the simulations shown below include driving delivered over time. In addition, Tuna features a finite, height-resolved ionospheric conductivity profile, rather than the perfectly-reflecting boundaries used in the past.

Each subplot in Figure 7.4 is analogous to Figure 3 in Mann and Wright's paper[64]. Blue lines show the total energy in the poloidal mode as a function of time. Red lines show toroidal energy. Runs are organized analogous to those in Figure 7.3: drive frequency is constant down each column, and azimuthal modenumer is constant across each row. Axis bounds are held constant across all subplots. The poloidal and toroidal energy are computed by integrating over the electromagnetic energy density, per Poynting's theorem:

$$U_P = \int \frac{dV}{2\mu_0}\left(B_x^2 + \frac{1}{v_A^2}E_y^2\right) \qquad\qquad U_T = \int \frac{dV}{2\mu_0}\left(B_y^2 + \frac{1}{v_A^2}E_x^2\right) \tag{7.1}$$

Where the differential volume dV is computed using the Jacobian[2] to account for Tuna's unusual geometry. The integral is evaluated in u^1 and u^3 but not u^2 (Tuna's missing half-dimension), which gives energy in units of gigajoule per radian. More than anything else, this serves as a reminder that Pc4 pulsations are localized in MLT.

[2]See Section 5.1.

The 28 runs shown in Figure 7.4 use an ionospheric profile corresponding to the dayside during times of low solar activity, where the conductivity is relatively high. The active and quiet dayside profiles are briefly contrasted in Section 7.4; for the most part, the focus of the present work is on the difference between the dayside and the nightside (Section 7.3). Differences between the two dayside profiles are small in comparison.

The fact that red (toroidal) lines appear at all in Figure 7.4 speaks to a net rotation of energy from the poloidal mode to the toroidal. As discussed in Section 5.3, Tuna's driving is delivered purely into the poloidal electric field, reflecting a perturbation in the magnitude of the ring current.

As expected, the rotation from poloidal to toroidal is slowest at large azimuthal modenumbers. The toroidal energy overtakes the poloidal energy within a single drive period at small m; at $m = 64$, the most of the energy is in the poloidal mode for $\sim$10 periods. However, the relationship between azimuthal modenumber and rotation timescale is not linear, as was suggested by Mann and Wright. Instead, in a practical setting, the rotation is fastest at $m \sim 4$.

This is explained by the compressional character of the poloidal mode. At very low modenumber, energy in the poloidal mode moves readily across L-shells. A significant fraction of that energy is lost to the outer boundary before rotating to the toroidal mode. At high modenumber, compressional propagation is evanescent, so all energy in the poloidal mode must ultimately rotate to the toroidal mode or be lost to Joule dissipation.

Joule dissipation is a major player in the system's energy economy. However, due to the highly conductive dayside ionosphere, dissipation timescales are in the tens of Pc4 wave periods. Energy loss through Joule dissipation asymptotically balances energy input from driving, but most of that energy is not lost until after it has rotated from the poloidal mode to the toroidal. As such, in most runs shown in Figure 7.4, the energy content of the toroidal mode asymptotically exceeds that of the poloidal mode.

The asymptotic energy content of the system also depends on how well the drive frequency matches the local eigenfrequency. If the two do not match, energy is lost to destructive interference between the standing wave and the driving.

In principle, energy moves between the poloidal and toroidal modes due to their direct coupling through the ionospheric Hall conductivity. In practice, this effect does not move large amounts of energy. When the runs shown in Figure 7.4 are repeated with the Hall conductivity set to zero, the resulting energy curves are not visibly different (not shown).

The low-m runs at 19 mHz merit additional discussion. These runs accumulate energy over a large number of wave periods, while the low-m waves at 13 mHz, 16 mHz, and 22 mHz do not. This effect is likely nonphysical. At 19 mHz, a third-harmonic resonance forms very close to the outer boundary, and is likely enhanced by nonphysical reflections against the simulation boundary.

The presence of individual harmonics can be seen in the contours shown in Figures 7.5 and 7.6. These figures show the same runs as Figure 7.4, arranged in the same way on the page. However, instead of showing the total energy integrated over the simulation domain, the energy densities are averaged over the volume of each flux tube individually. Figure 7.5 shows contours of poloidal energy density and Figure 7.6 shows toroidal energy density.

The top few rows of Figure 7.5 confirm that the poloidal mode's compressional nature is to blame for its failure to accumulate energy at low modenumber. Waves move so readily across field lines that no visible amount of energy builds up at $L \sim 5$, the location of the driving. Some energy moves inward, and is trapped by the peak in Alfvén speed just inside the plasmapause, while the rest moves to the outer boundary. The time spent moving across field lines counts against the poloidal mode's finite lifetime, inhibiting the buildup of poloidal energy density even at L-shells where the wave matches the local eigenfrequency.

As m increases, the energy distribution becomes more concentrated in L, though individual features remain fairly broad. At $m = 8$, runs at 13 mHz and 16 mHz are inclined to build up energy just inside the plasmapause, while those at 19 mHz and 22 mHz resonate just outside the plasmapause; in all four cases, the energy is spread over a range of at least 1 in L.

The peak energy density in the bottom-right run (22 mHz driving, $m = 64$) is by far the largest of any run in Figure 7.5. The azimuthal modenumber is large, so the poloidal mode is purely guided; energy is not smeared across multiple L-shells. And, crucially, the frequency of the driving matches closely with the Alfvén frequency at $L \sim 5$. Other runs on the bottom row are also guided, but they reach lower asymptotic energy densities because of a mismatch between the drive frequency and the local eigenfrequency — resulting in destructive interference between the standing wave and its driver.

Giant pulsations are typically seen at ∼10 mHz, well below the 22 mHz poloidal peak shown in Figure 7.5. Part of the discrepancy is likely due to the position of the driving. Pgs are most common at latitudes of ∼66°, which maps out to $L \sim 6$, whereas these runs are driven at $L \sim 5$. The size of the plasmapause also has a significant effect. When the runs in Figure 7.5 are repeated with the plasmapause at $L = 5$ instead of $L = 4$, the strongest resonance (driven at $L \sim 5$) drops from 22 mHz to 16 mHz (not shown).

Whereas the poloidal contours are smeared over a swath of L-shells (though the high-m runs less so), the toroidal contours in Figure 7.6 appear only where the wave frequency matches the local eigenfrequency. A horizontal line drawn through the Alfvén speed frequency profiles (recall Figure 3.1) intersects the profile up to three times: once as the Alfvén frequency drops through the Pc4 range from its low-latitude peak, again as the Alfvén frequency rises sharply at the plasmapause, and a third time as the Alfvén frequency drops asymptotically. Toroidal waves can be seen resonating at all three of these locations in the $m = 4$, 22 mHz run in Figure 7.6, along with a third harmonic at large L. This is consistent with observations: toroidal resonances are noted for having frequencies which depend strongly on L, in contrast to the poloidal mode's less-strict relationship between frequency and location.

In only one of the runs shown in Figure 7.5 does the poloidal mode attain an energy density on the order of $10^{-1}\,\mathrm{nJ/m^3}$. On the other hand, the toroidal mode reaches $\sim 10^{-1}\,\mathrm{nJ/m^3}$ in six of the runs in Figure 7.6. That is, the poloidal mode only exhibits a high energy density on the dayside only when conditions are ideal; the toroidal mode isn't nearly so particular.

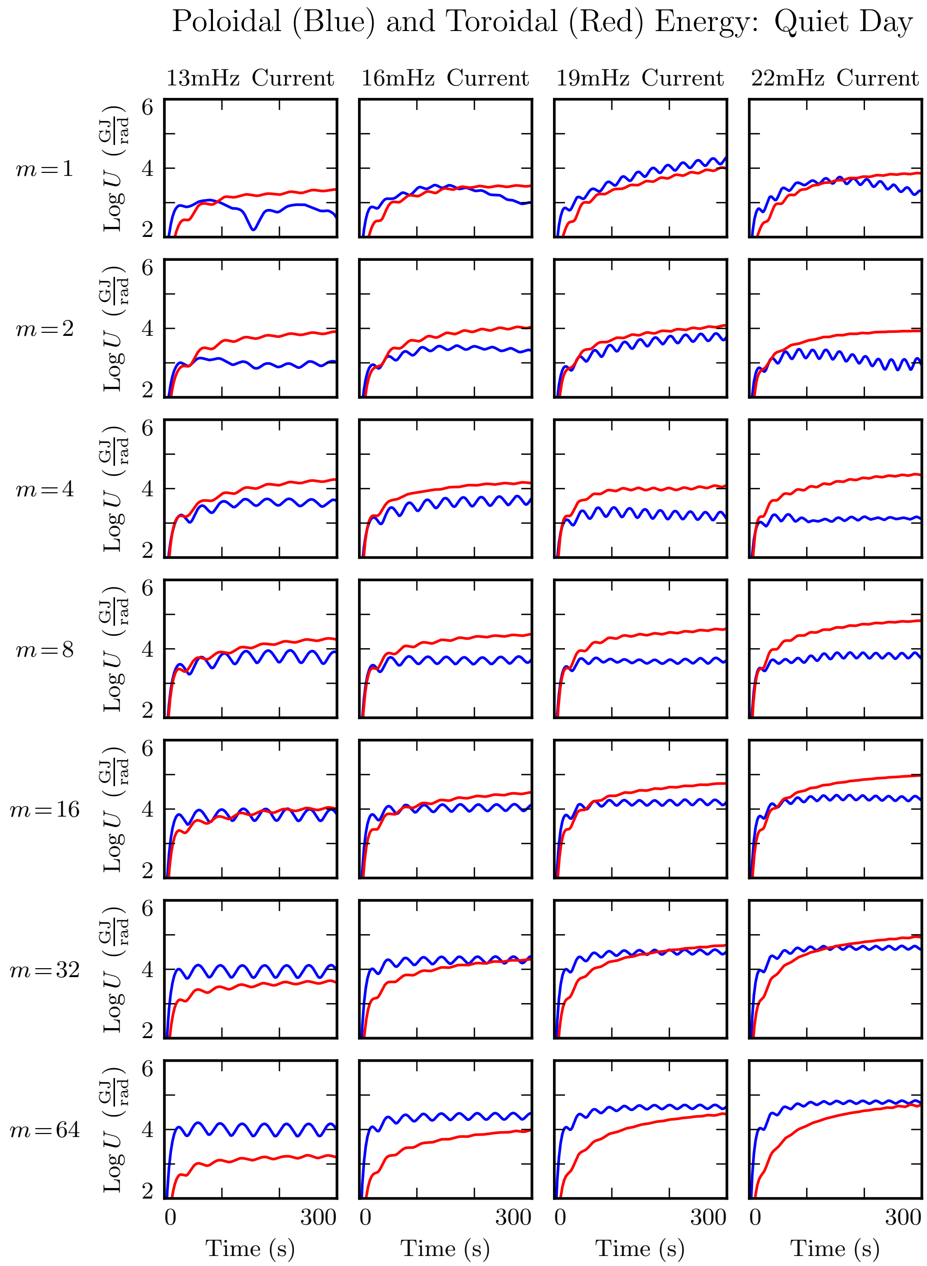

Figure 7.4: Each subplot above shows the poloidal (blue) and toroidal (red) energy for a simulation as a function of time. Each row contains four simulations, each with the same azimuthal modenumber; the seven rows in each column share a drive frequency. Driving is purely poloidal, but energy rotates asymptotically to the toroidal mode, and rotation is slowest at high modenumber.

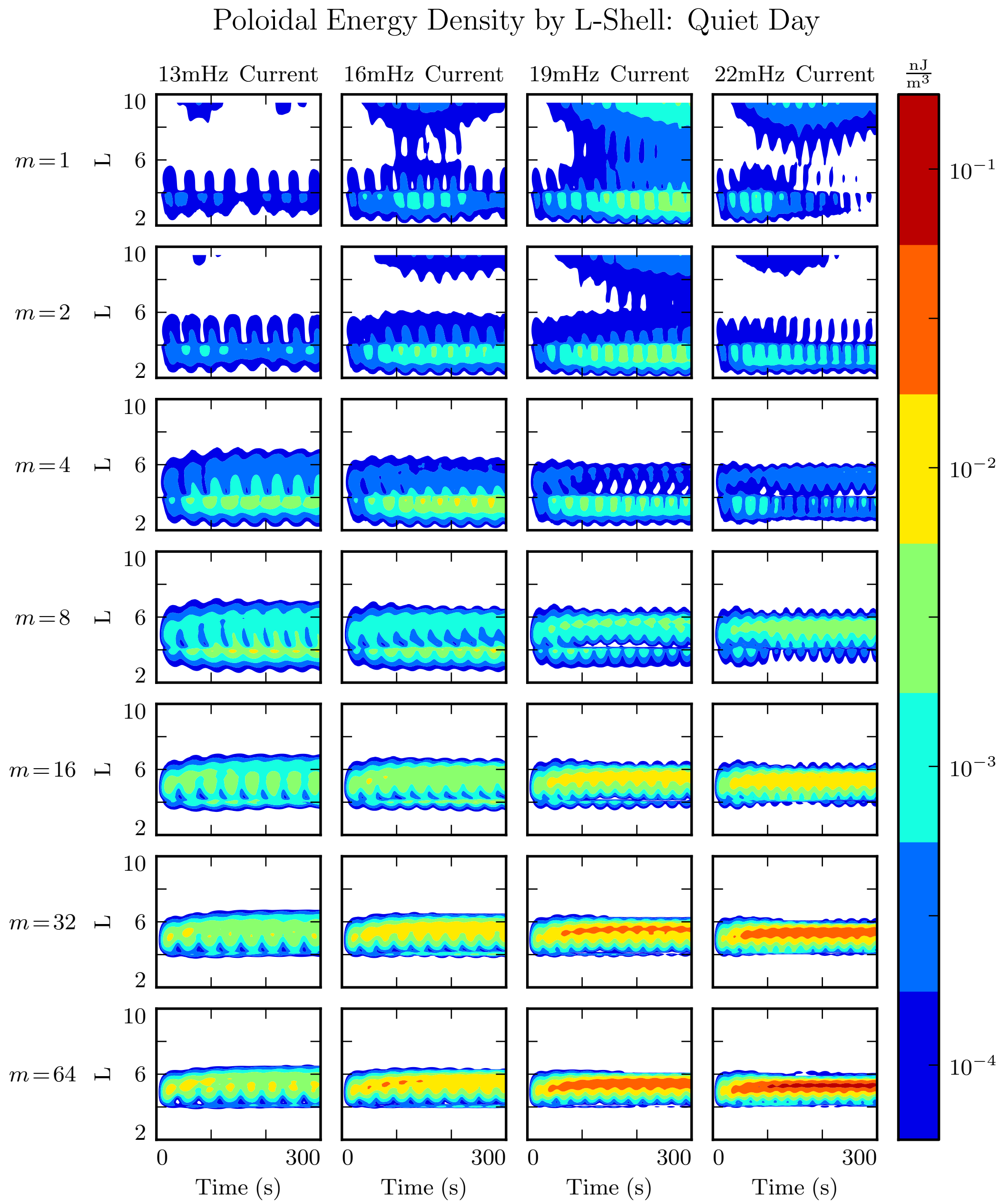

Figure 7.5: At low modenumber (top rows), the compressional nature of the poloidal mode allows energy to escape the simulation. At high modenumber (lower rows), the poloidal mode is guided; energy is trapped at the L-shell where it's injected, and rotation to the toroidal mode is slow — ideal conditions for resonance. But energy buildup is lackluster except where the drive frequency matches the local eigenfrequency (best in the rightmost row).

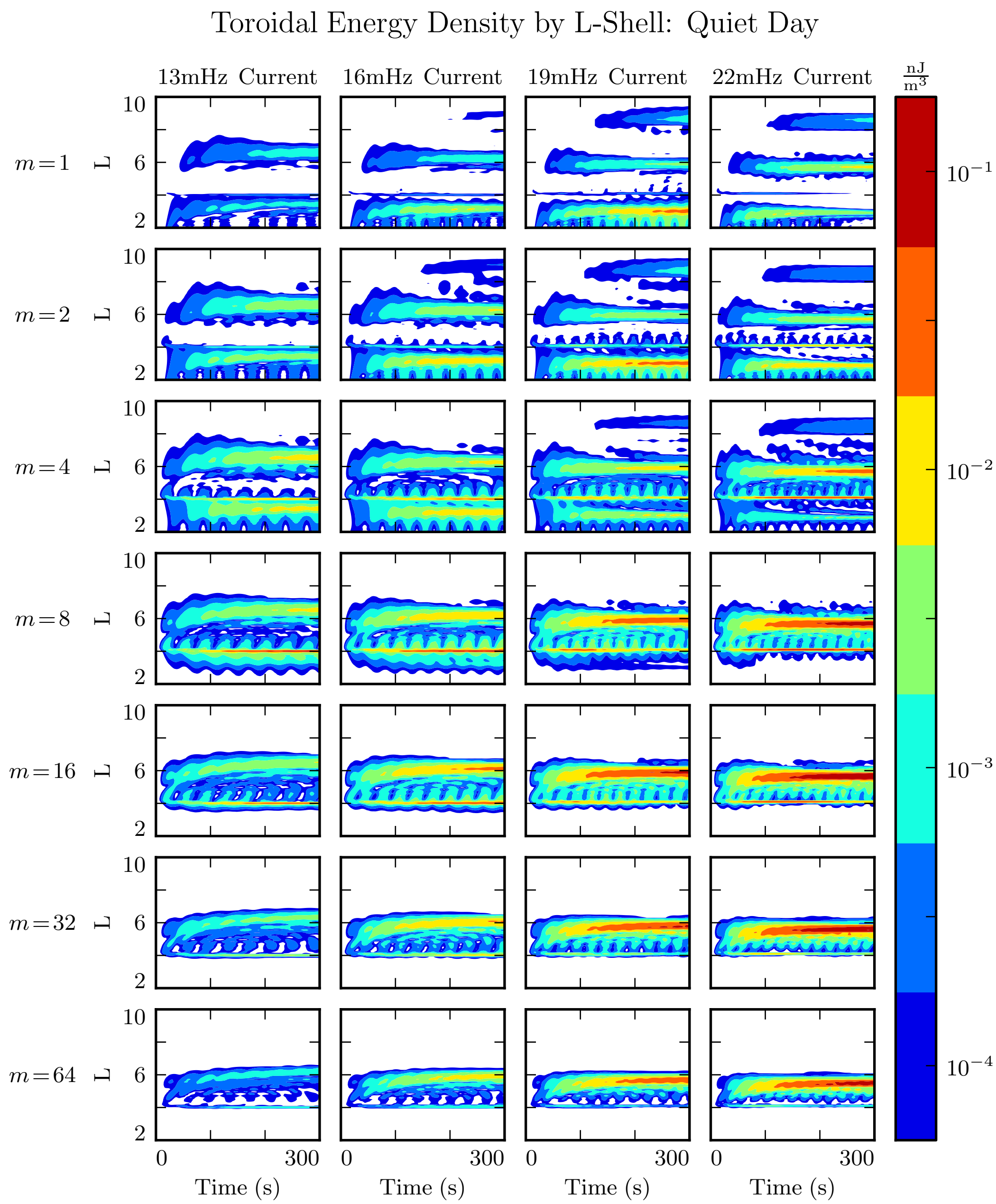

Figure 7.6: Whereas the poloidal mode is smeared in L due to its compressional nature, the toroidal mode is focused at L shells where it's resonant. In general, when the conductivity is high, the toroidal mode also exhibits a higher asymptotic energy density than the poloidal mode (Figure 7.5).

7.3 Resonance and Rotation on the Nightside

Compared to the dayside ionosphere employed in Section 7.2, conductivity on the nightside is much lower. Runs in the present section use Tuna's ionospheric profile corresponding to the nightside during quiet solar conditions. The two nightside profiles are briefly compared in Section 7.4, but for the most part the present work is concerned with the behavior of the nightside compared to that on the dayside.

Other than the change in ionospheric profile, Figures 7.7 to 7.9 are analogous to Figures 7.4 to 7.6. Each subplot corresponds to a different 300 s run of Tuna. Drive frequency is constant down each column, and azimuthal modenumber is constant across each row.

The low conductivity on the nightside gives rise to strong Joule dissipation. Waves are damped out in just a few bounces, so asymptotic energy values are reached quickly. No combination of frequency and modenumber gives rise to the accumulation of energy over multiple drive periods.

As on the dayside, rotation of energy from the poloidal to toroidal mode is fastest at $m \sim 4$. Unlike the dayside, however, dissipation on the nightside is fast compared to the rotation of energy to the toroidal mode. Toroidal energy does not asymptotically exceed the poloidal energy by a significant margin in any run shown in Figure 7.7. At $m = 64$, where the rotation timescale is slowest, no more than $10\,\%$ of the energy in the poloidal mode rotates to the toroidal mode before being lost.

Also similar to the dayside, low-m runs driven at 19 mHz and 22 mHz resonate very close to the outer boundary. As before, the buildup of energy is likely nonphysical.

Poloidal contours on the nightside (Figure 7.8) are weaker than those on the dayside, and build up energy over less time, but otherwise similar. At low modenumber, poloidal energy propagates across L-shells, preventing the significant accumulation of energy anywhere. As the modenumber increases, energy is contained near the driving at $L \sim 5$. The strongest response is seen at 13 mHz on the bottom row, where the modenumber is at its largest and the frequency matches closest with the local eigenfrequency. Even in that case, dissipation timescales are comparable to the oscillation period, so the wave only persists in the presence of continuous driving.

Toroidal energy contours on the nightside exhibit significantly different behavior from those on the dayside.

At low modenumber, the nightside toroidal mode (Figure 7.9) contains less energy than on the dayside, but it still shows some preference for sharp resonances where the drive frequency matches the local Alfvén frequency. At moderate modenumbers, as on the dayside, the toroidal mode is more or less comparable in strength to its poloidal counterpart. It's only at high modenumber that the difference between the dayside and nightside toroidal contours become truly dramatic. Whereas on the dayside, most energy is asymptotically deposited in the toroidal mode, on the nightside most poloidal energy is dissipated faster than the poloidal-to-toroidal rotation timescale. At $m = 64$, where the poloidal mode is at its strongest, the toroidal mode is at its weakest; it barely registers, even on Figure 7.9's log scale.

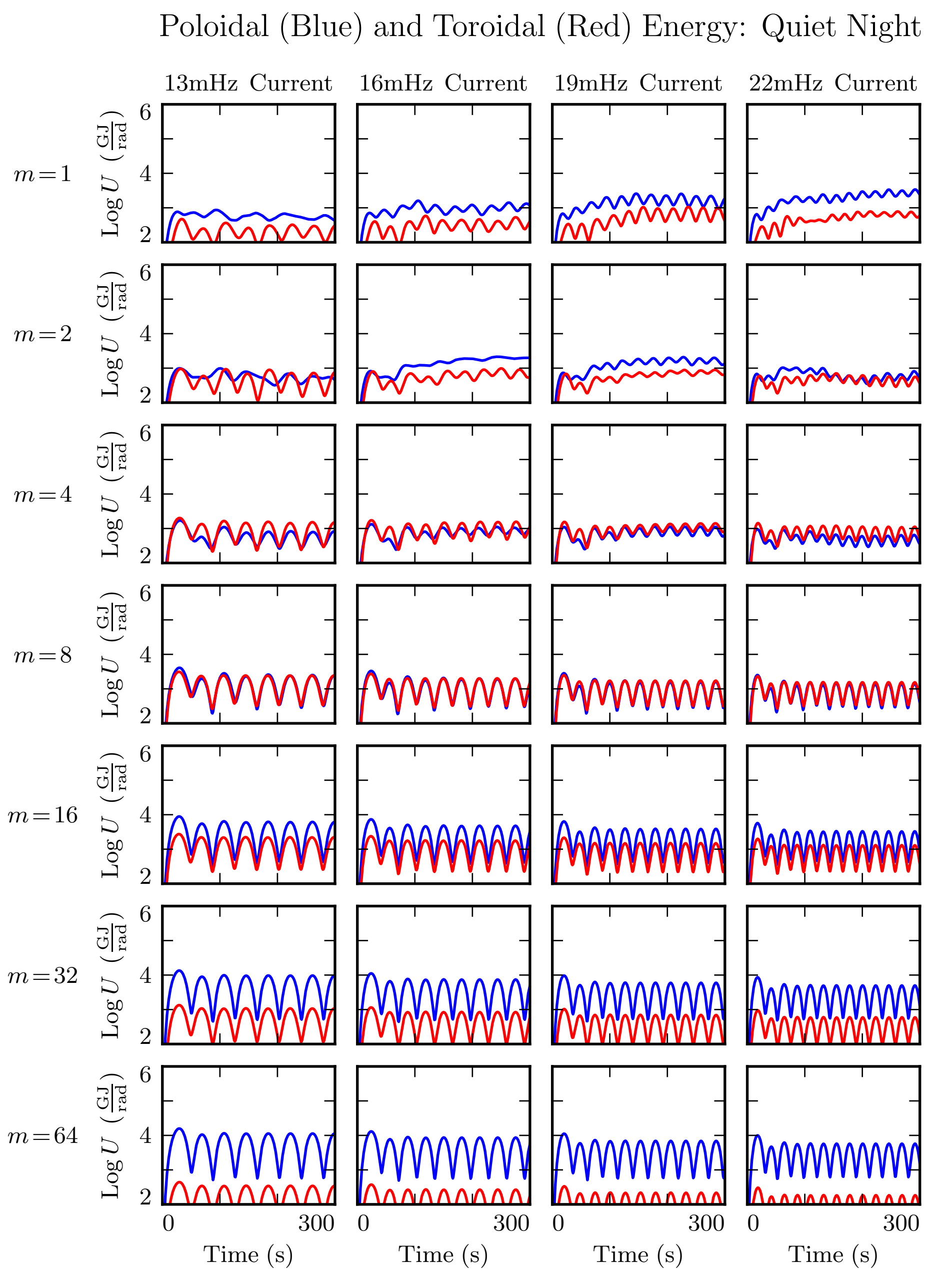

Figure 7.7: The energy content of each FLR on the nightside resembles that of a damped, driven oscillator. Energy is periodically added to the system, but most is lost too fast to rotate to the toroidal mode, particularly at high modenumber. There is no significant buildup of energy over multiple periods. Runs at $m = 1$ (top row) are an apparent exception, likely due to a nonphysical interaction with the boundary.

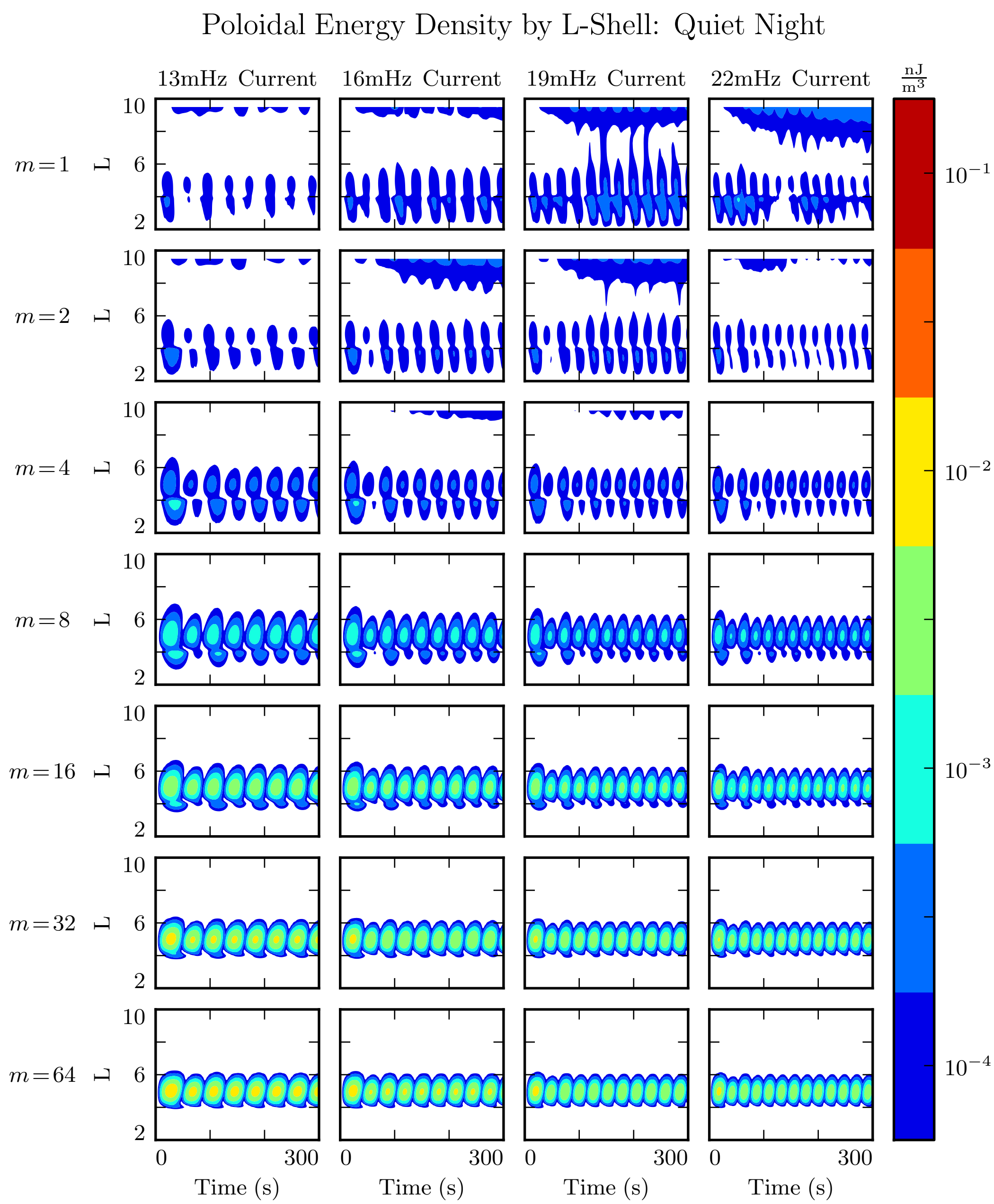

Figure 7.8: As on the dayside (Figure 7.5), low-modenumber poloidal waves (top rows) readily propagate across L-shells and escape the simulation domain. Energy density builds up most effectively at high modenumber, where the poloidal mode is guided, and poloidal-to-toroidal rotation is slow. Even in this case, however, dissipation is fast enough to prevent energy from accumulating over multiple drive periods.

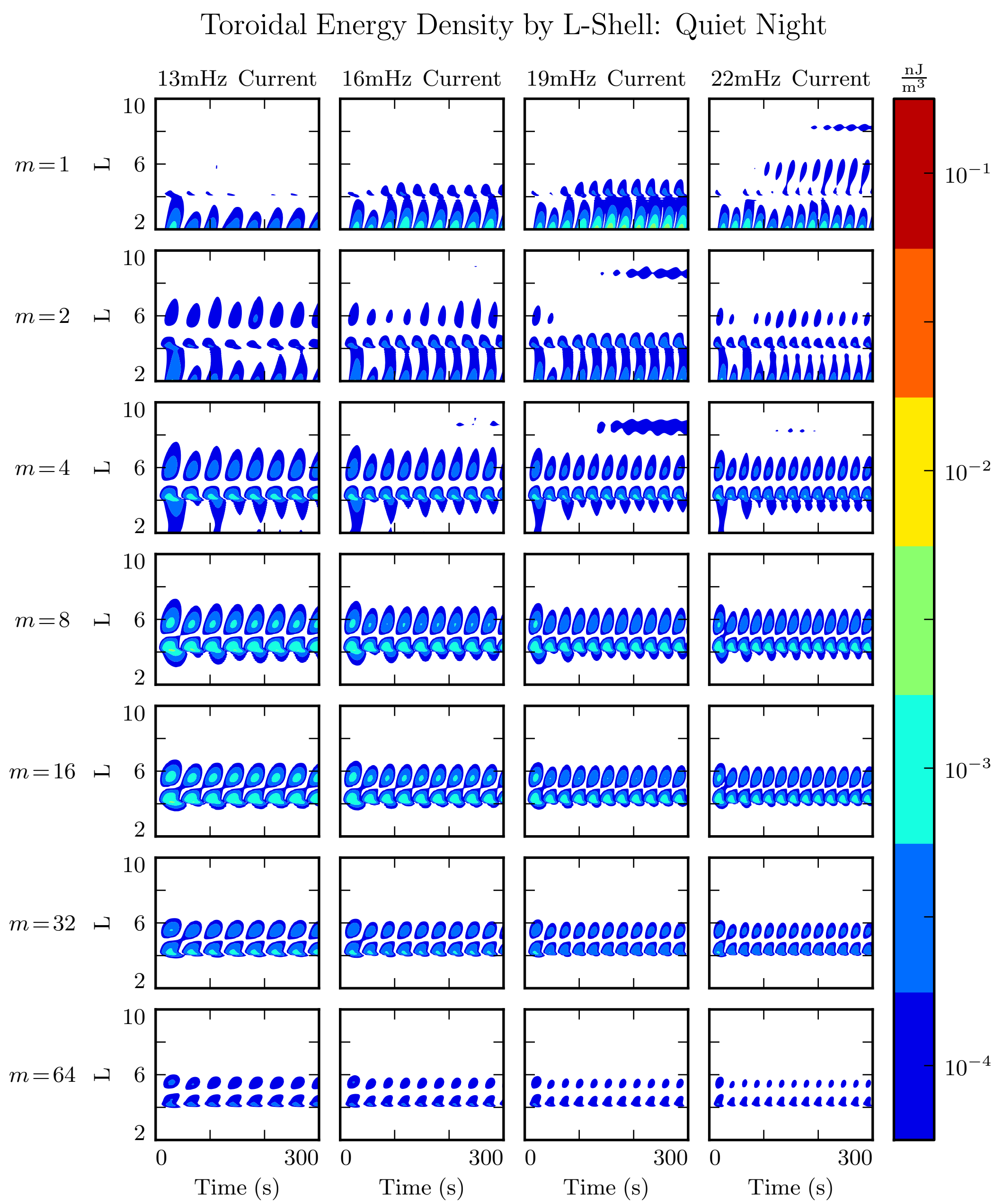

Figure 7.9: On the dayside (Figure 7.6), most energy rotates asymptotically to the toroidal mode. On the night side, the same is not true, since the poloidal mode quickly loses energy to Joule dissipation. At high modenumber, where the poloidal-to-toroidal rotation timescale is in the tens of wave periods, almost all of the energy is dissipated from the poloidal mode rather than rotating to the toroidal mode.

7.4 Ground Signatures and Giant Pulsations

While the majority of the action is in space, the majority of FLR observations have historically been ground-based. The present section explores simulations (including those discussed in Sections 7.2 and 7.3) in terms of their ground signatures rather than their integrated energy distributions.

Figures 7.10 and 7.11 show fourteen runs each, two per row. Contours give magnetic fields at the ground, plotted against time on the horizontal axis and latitude on the vertical axis. Modenumber is held constant across each row, as in the above sections; columns show north-south and east-west ground signatures using an ionospheric profile for active (first and second columns respectively) and quiet (third and fourth columns).

As noted in Chapter 3, the magnetic polarization of a low frequency Alfvén wave is rotated by $\sim 90^\circ$ as it passes through the ionosphere. The east-west field on the ground (B_ϕ) corresponds to the poloidal polarization in space, and the north-south field on the ground (B_θ) corresponds to the toroidal mode.

The most striking feature of Figures 7.10 and 7.11 is the modenumber dependence. As modenumber increases, the magnetic field signatures become sharply localized in latitude. At high m, ground signatures are concentrated between 60° and 70°, peaking near 64°, roughly coincident with the foot point of the $L = 5$ field line; ionospheric ducting is not significant in the Pc4 regime.

At low modenumber, magnetic signatures are weak on the ground because the waves in space are also weak. At high modenumber, waves in space are strong, but so is the attenuation of magnetic signatures by the atmosphere[3]. The "sweet spot" at which magnetic ground signatures are maximized falls at $m = 16$ to $m = 32$.

Tuna shows stronger ground signatures on the dayside than on the nightside, more or less in proportion with the difference in magnitude in space. Energy on the dayside (which depends on field magnitude squared) peaks an order of magnitude larger than that on the nightside. Peak ground signatures on the dayside are larger by a factor of four: 45 nT compared to 11 nT. On both the dayside and the nightside, peak ground

[3] See Equation (3.3).

signatures are in B_ϕ, the east-west magnetic field component; both peaks are also at $m = 16$, and both are seen in runs using the ionospheric profile for quiet solar activity.

It's further notable that the ground signatures — particularly those on the nightside — exhibit a change in chirality based on latitude. At low latitude, B_θ leads B_ϕ, which creates a counterclockwise signature on the ground (in the northern hemisphere). At high latitude, the phase is reversed, resulting in a clockwise ground signature.

These results match well with the properties associated with Pgs: east-west polarization, latitude-dependent chirality, peak latitude of $\sim 66^\circ$, and azimuthal modenumber of 16 to 35. Just about the only properties missing are the azimuthal drift (which is beyond the scope of the present model) and the distribution in MLT. Pgs are most commonly observed pre-dawn, but morning and evening ionospheric profiles are not presently implemented for Tuna.

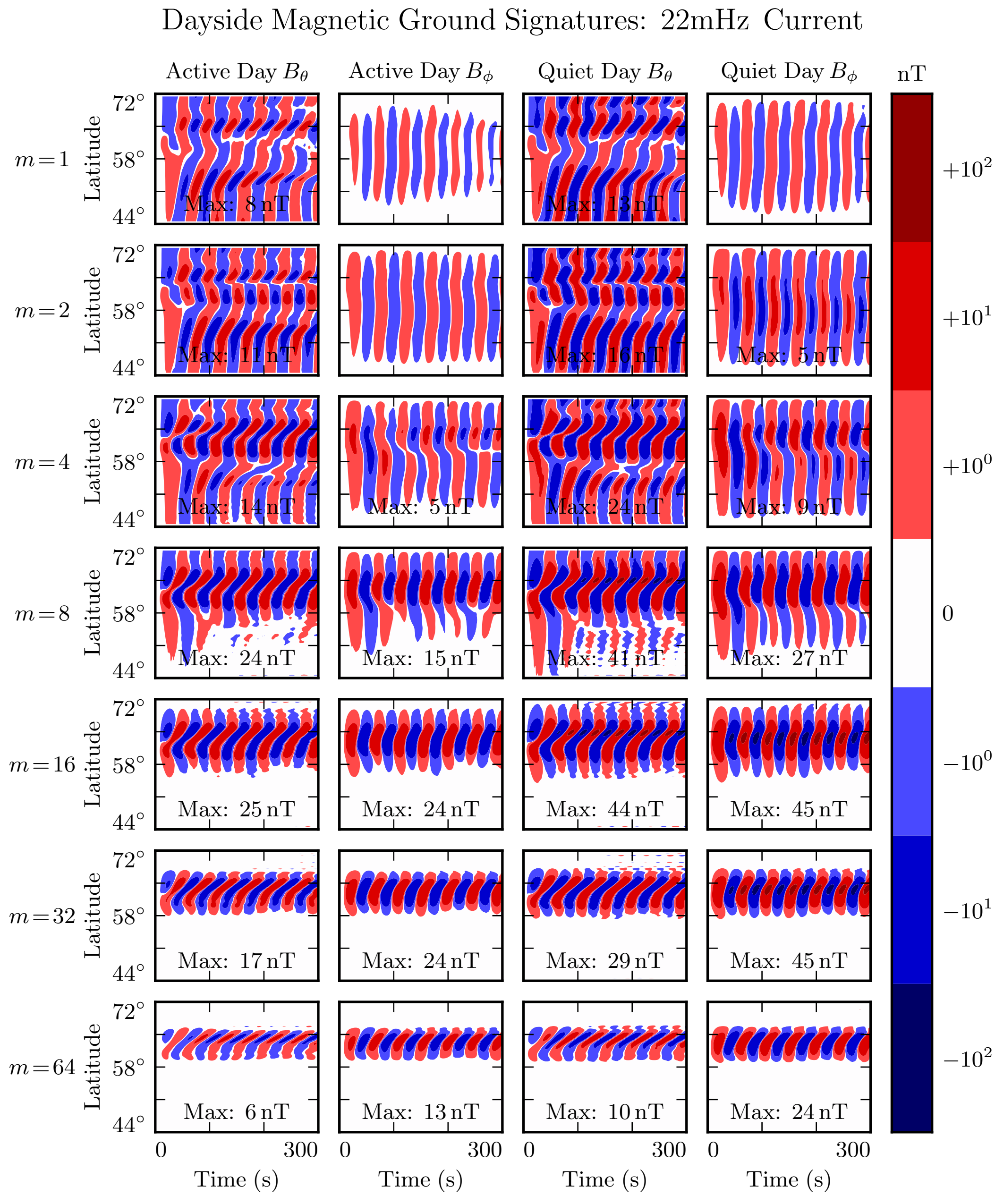

Figure 7.10: The magnetic ground signatures are shown for fourteen runs, two per row. Azimuthal modenumber is constant across each row. Polarization and ionospheric profile vary by column, per the headers. Ground signatures at low modenumber are weak because the waves in space are weak, while those at high modenumber are attenuated by the atmosphere. Considering both effects, ground signatures seem to be maximized at $m = 16$ to $m = 32$. Peak amplitudes above 3 nT are marked.

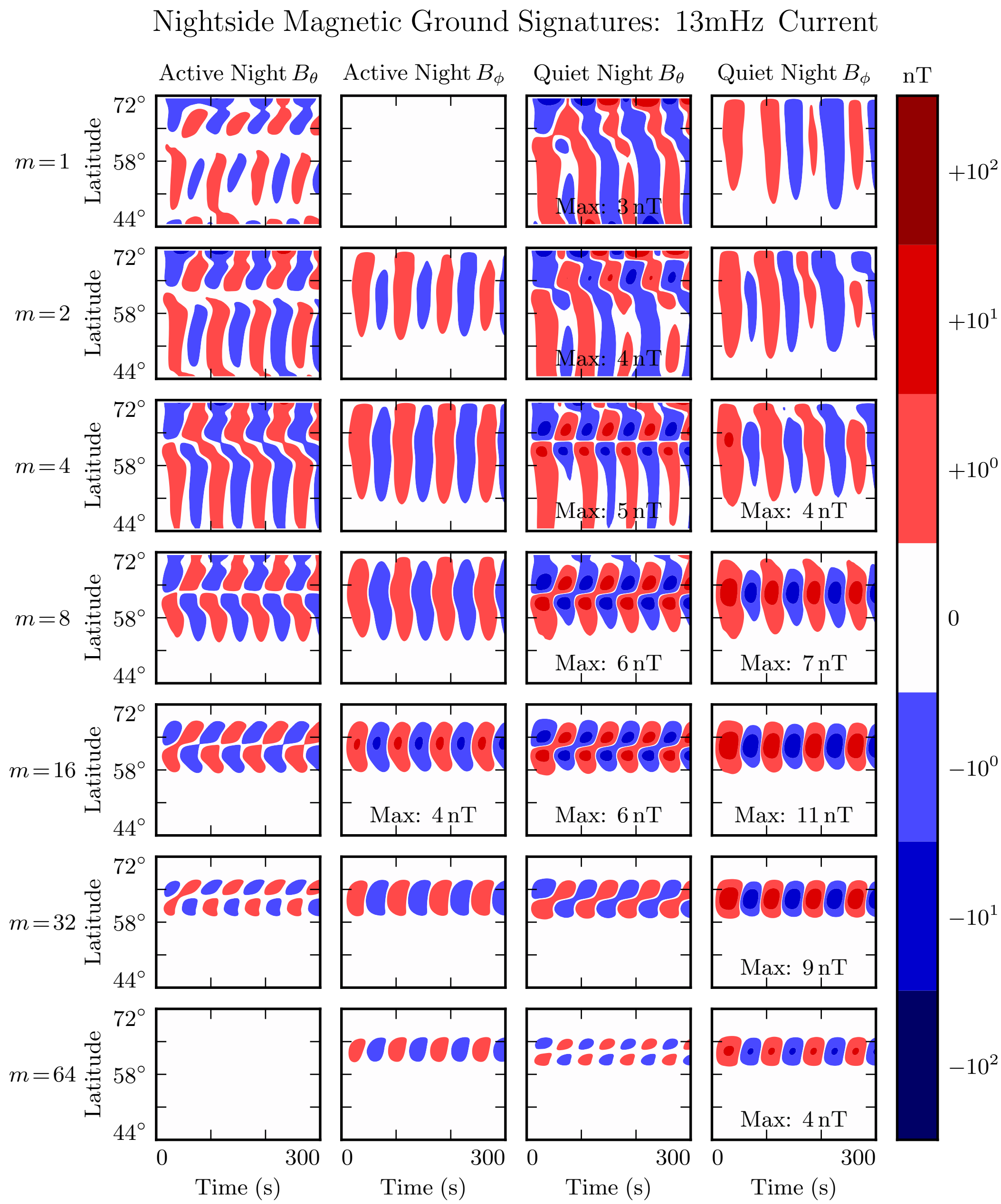

Figure 7.11: Nightside ground signatures are less strongly peaked than those on the dayside, but qualitative features are the same: the strongest signals are in B_ϕ, peaked over just a few degrees in latitude, at a modenumber of 16 or 32, under quiet ionospheric conditions.

7.5 Discussion

The above results show agreement with a number of past FLR studies. In addition, several novel connections are suggested between known properties of FLRs.

The compressibility of poloidal FLRs at low modenumber, but not high modenumber, is reproduced and quantified. At $m \sim 1$, the poloidal and compressional components of an FLR in the Pc4 range are comparable in magnitude. At $m \gtrsim 6$, $\left|\frac{B_z}{B_x}\right| \lesssim \frac{1}{2}$, and at $m \gtrsim 12$, $\left|\frac{B_z}{B_x}\right| \lesssim \frac{1}{4}$.

The present results also suggest that compressional character of poloidal Pc4s is to blame for the weak relationship between L and frequency, compared to that seen in toroidal events. Toroidal resonances are defined sharply in L regardless of modenumber, while poloidal resonances are smeared in L — particularly at low m, but to some degree at high m as well.

The asymptotic rotation of energy from the poloidal mode to the toroidal mode is reproduced; at small m, the rotation timescale is comparable to a wave period, while at large modenumber it's on the order of 10 periods. On the dayside, little energy is lost to Joule dissipation on rotation timescales. In contrast, on the nightside, dissipation timescales are comparable to wave periods. In high-m nightside runs, even in the case of continuous driving near the local eigenfrequency, the movement of energy from the poloidal mode to the toroidal mode is vanishingly small.

Ground signatures at low modenumber are shown to be weak because waves in space are weak; this is particularly true for poloidal waves — a non-guided wave can't very well resonate along a field line — but also true of toroidal waves insomuch as poloidal waves are their source. FLRs resonate most strongly at high m, but high-m signatures are also attenuated by the atmosphere. The balance between the two effects falls around m of 16 to 32. It's further suggested that a high-m driver will cause a weak resonance in place rather than tunneling across field lines to a matching eigenfrequency, and that the same driving should give rise to stronger ground signatures during times of low solar activity, on both the dayside and the nightside.

The findings together suggest, awkwardly, that the morphology of giant pulsations reveals relatively little about their origins.

One can consider a hypothetical magnetosphere subject to constant driving: broadband in frequency, broadband in modenumber, just outside the plasmapause. Low-m poloidal waves will quickly rotate to the toroidal mode (and/or propagate away). High-m waves will resonate in place, accumulating energy over time, and giving rise to "multiharmonic toroidal waves"[87]; Fourier components that do not match the local eigenfrequency will quickly asymptote. Waves with very high modenumbers will be attenuated by the ionosphere. The response on the ground will be counterclockwise at low latitude, clockwise at high latitude, peaked at $16 \lesssim m \lesssim 32$, mostly east-west polarized, and notably stronger during quiet solar conditions. In other words, the measurements will look very much like a giant pulsation.

The present results offer no explanation as to the tendency of giant pulsations to drift azimuthally, or to appear pre-dawn in MLT — though the latter is addressed by the observational results in Chapter 8.

Chapter 8

Van Allen Probe Observations

The results presented in Chapter 7 are interesting on their own, but become particularly valuable when combined with observational data. Unfortunately, only a small number of studies to date have explored how Pc4 observation rate is affected by the harmonic and polarization structure of those waves. While Pc4 pulsations have previously been studied in terms of both harmonic[4, 14, 26, 43, 81, 90] and polarization[2, 16, 17, 52, 56], no past survey has characterized each event in terms of both properties.

This has largely been due to observational constraints. The classification of a wave's harmonic is best carried out by computing the phase offset of the magnetic and electric field waveforms, simultaneous in situ measurements of which have only recently become available since the launch of THEMIS[3] in 2007 and the Van Allen Probes[84] in 2012. The Van Allen Probes are particularly well-suited to the study of Pc4 pulsations as their apogee of $L \sim 6$ coincides closely with eigenfrequencies in the Pc4 range.

The present chapter uses data from the Van Allen Probes mission to survey the occurrence rate of FLRs in the Pc4 range as a function of parity and polarization, as well as magnitude, frequency, and phase. The tools used to perform the present analysis — SPEDAS and the SPICE kernel — are publicly available. They, along with the Python routines used to download, filter, and plot the data, can be found at `https://github.com/UMN-Space-Physics`.

8.1 Sampling Bias and Event Selection

The present analysis makes use of Van Allen Probe data from October 2012 to August 2015 — the entire range available at the time of writing. Between the two probes, that's just over 2000 days of observation.

For the purposes of the present work, the two probes are taken to be independent observers. A preliminary estimate shows that Pc4 events are sufficiently narrow in MLT that they are rarely ($\sim$1 %) seen by both probes simultaneously. The events are also short-lived enough that they are rarely seen by the two probes passing through the same region of space, no more than a few hours apart. That said, a future investigation into the few events that are seen by both probes could offer significant insight into the structure and behavior of these waves.

Electric and magnetic field data are collected using the probes' EFW[100] and EMFISIS instruments respectively. Level 3 values are used, averaged over the ten-second probe spin period. Three-dimensional electric field data is obtained by using the $\underline{E} \cdot \underline{B} = 0$ assumption; at such low frequencies, this is more accurate than measurements taken using the spin-axis boom. Notably, this assumption is taken only when the probe's spin plane is offset from the magnetic field by at least 15°. The rest of the data — about half — is discarded, potentially introducing a sampling bias in MLT.

A further bias is introduced by the probes' non-integer number of precessions around Earth. As of July 2014, apogee had completed one fill precession[16]. The present work considers roughly one and a half precessions; the nightside has been sampled at apogee twice as often as the dayside.

The spatial distribution of usable data — that is, data for which three-dimensional electric and magnetic fields are available at the desired accuracy — is shown in Figure 8.1. Bins are unitary in L and in MLT. The distribution of the data in magnetic latitude is not shown; the Van Allen Probes are usually localized to within 10° of the equatorial plane.

Field measurements are transformed into the same dipole coordinates used in Chapters 5 and 7. The background magnetic field is estimated using a ten-minute running average

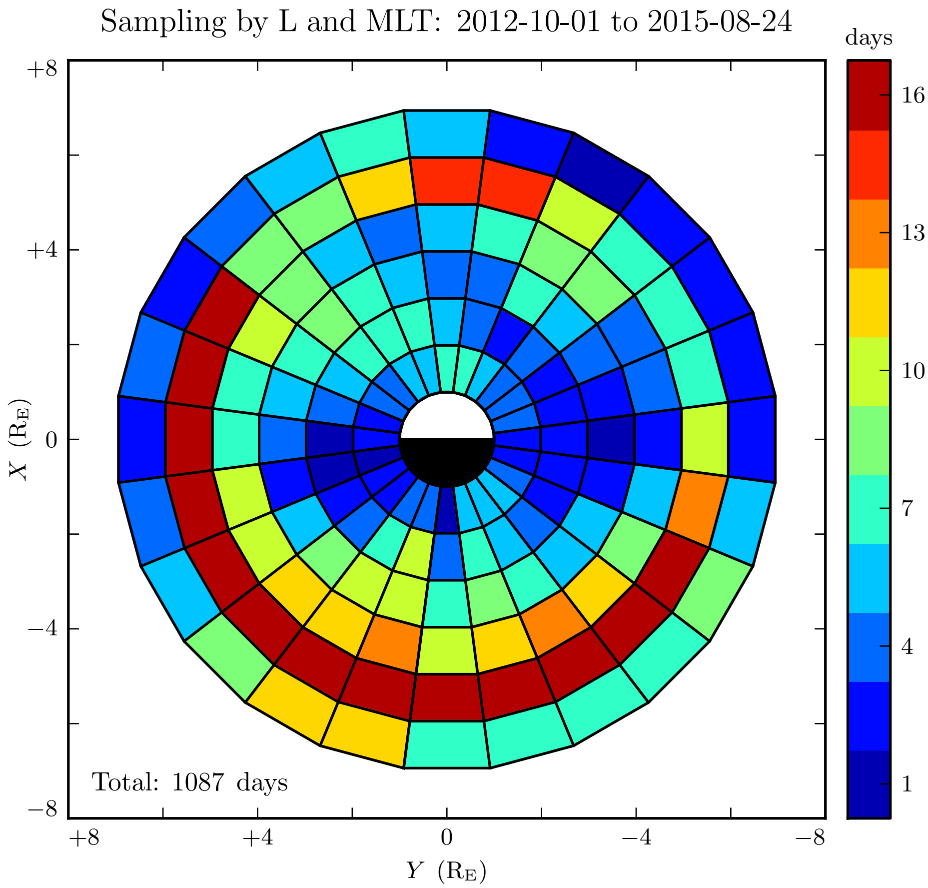

Figure 8.1: The above figure shows the spatial distribution of sampling by the Van Allen Probes. Bins are unitary in the polar coordinates L and MLT; the spatial scale is indicated by the SM X and Y axes. The Van Allen Probes have precessed one and a half times around Earth, so the nightside has been double-sampled at apogee, resulting in a significant sampling bias.

of the magnetic field measurements; that defines the z axis. The y axis is set parallel to $\hat{z} \times \underline{r}$, where $\underline{r}$ is the probe's geocentric position vector. The x axis is then defined per $\hat{x} \equiv \hat{y} \times \hat{z}$. This scheme guarantees that the axes are right-handed and pairwise orthogonal[56].

The ∼1000 days of usable data are considered half an hour at a time, which gives a frequency resolution of ∼0.5 mHz in the discrete Fourier transform. Spectra are computed for all six field components: $\widetilde{B}_x$, $\widetilde{B}_y$, $\widetilde{B}_z$, $\widetilde{E}_x$, $\widetilde{E}_y$, and $\widetilde{E}_z$. The background magnetic field is subtracted before transforming the magnetic field components, leaving only the perturbation along each axis[1]. Each waveform is also shifted vertically so that its mean over the thirty minute event is zero.

Poynting flux along the field is computed from the electric and magnetic field transforms. A factor of $\left(\frac{r}{R_I}\right)^3$ compensates the compression of the flux tube, so that the resulting values are effective at the ionosphere. Poloidal and toroidal Poynting flux, respectively, are given by:

$$\widetilde{S}_P \equiv -\left(\frac{r}{R_I}\right)^3 \frac{1}{\mu_0}\widetilde{E}_y\widetilde{B}_x^* \qquad\qquad \widetilde{S}_T \equiv \left(\frac{r}{R_I}\right)^3 \frac{1}{\mu_0}\widetilde{E}_x\widetilde{B}_y^* \tag{8.1}$$

The poloidal and toroidal channels are independently checked for Pc4 waves. For each channel, a Gaussian profile is fit to the magnitude of the Poynting flux, $|\widetilde{S}(\omega)|$. If the fit fails to converge, or if the peak of the Gaussian does not fall within 5 mHz of the peak value of $\widetilde{S}$, the event is discarded. Events are also discarded if their frequencies fall outside the Pc4 frequency range (7 mHz to 25 mHz) or if their amplitudes fall below $0.005\,\mathrm{mW/m^2}$ (out of consideration for instrument sensitivity).

Poynting flux magnitude is used rather than magnetic field magnitude (as is more typical) to avoid a bias against the detections of odd harmonics, which exhibit a magnetic field node at the equator.

Events are discarded if their parity is ambiguous. The electric field and the magnetic field must be coherent at a level of 0.9 or better (judged at the discrete Fourier transform point closest to the peak of the Gaussian fit). Any event within 3° of the magnetic equator is also not used; as discussed in Chapter 3, in order to distinguish an odd mode from an even mode, it's necessary to know whether the observation is made north or south of the equator.

A visual inspection of events shows that those with broad "peaks" in their spectra are typically not peaked at all — they are noisy spectra with several spectral features

[1] As in Chapters 4 to 7, B_x, refers not to the full magnetic field in the x direction, but to the perturbation in the x direction from the zeroth-order magnetic field. The same is true for B_y and B_z.

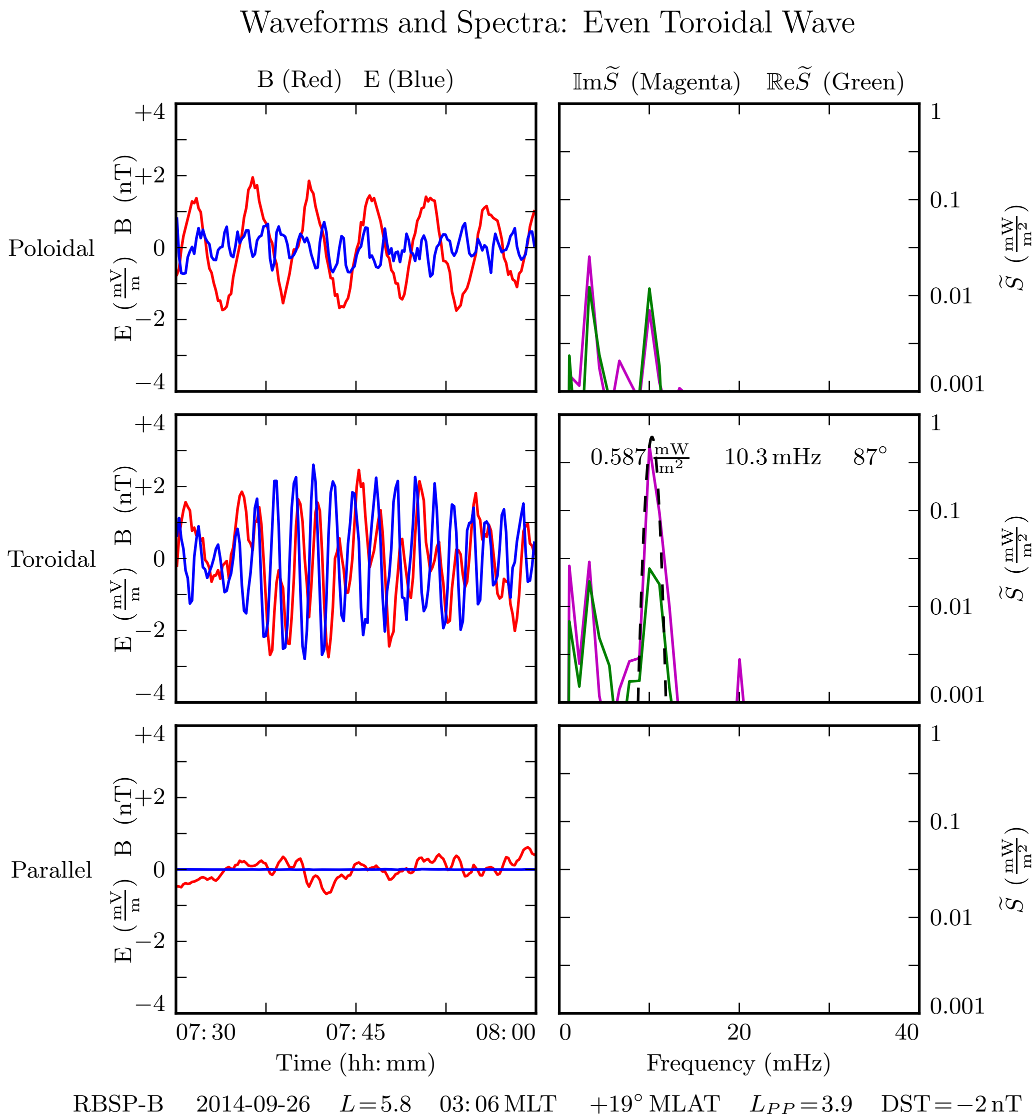

Figure 8.2: ...

grouped just closely enough to trick the fitting routine. A threshold is set at a FWHM of 3 mHz (equally, a standard deviation of 1.27 mHz). Any event with a Gaussian fit broader than that is discarded.

Notably, events are not filtered on their phase — that is, on the division of their energy between standing and traveling waves. This is the topic of Section 8.5.

8.2 Events by Mode

The filters described in Section 8.1 yield 762 half-hour Pc4 events, the spatial distribution of which is shown in Figure 8.3. In each bin, the event count is normalized to the amount of usable data (Figure 8.1). Bins shown in white contain zero events. The rate in the bottom corner is an overall mean; it's an estimate of how often Pc4 events would be observed if the sampling were distributed uniformly in space.

Consistent with previous work[2, 16, 52, 56], Pc4 events peak on the dayside and are rarely observed at $L < 4$. Nearly 30 % of the usable data shown in Figure 8.1 is taken at $L < 4$, yet only 16 of the 762 events (2 %) appear there.

On the other hand, the present work runs contrary to recent results by Dai et al in terms of Pc4 event rates with respect to the plasmapause (not shown). Their analysis found (poloidal) Pc4 pulsations to be comparably common inside and outside the plasmapause[16]. In the present work, only 40 of the 762 events (5 %) fall inside the plasmasphere, despite the fact that 40 % of the available data falls within the plasmasphere. It's possible that the discrepancy is due to differing definitions of the location of the plasmapause; Dai et al identify the plasmapause by the maximum gradient in electron number density, while the present work takes an electron density of $100\,/\mathrm{cm}^3$ to mark the plasmapause[2]. Event selection criteria also vary significantly between the present survey and that conducted by Dai et al — their work shows poloidal events located based on high-cadence magnetic field data only, while the present work also considers toroidal waves and electric fields, but at lower cadence.

The same events in Figure 8.3 are shown again in **??**, partitioned by polarization and parity.

The distribution of even poloidal events in Figure 8.4 is consistent with that reported by Dai et al[16]: the observation rate is peaked at noon, and extends across the dusk

[2] Per ongoing work by Thaller.

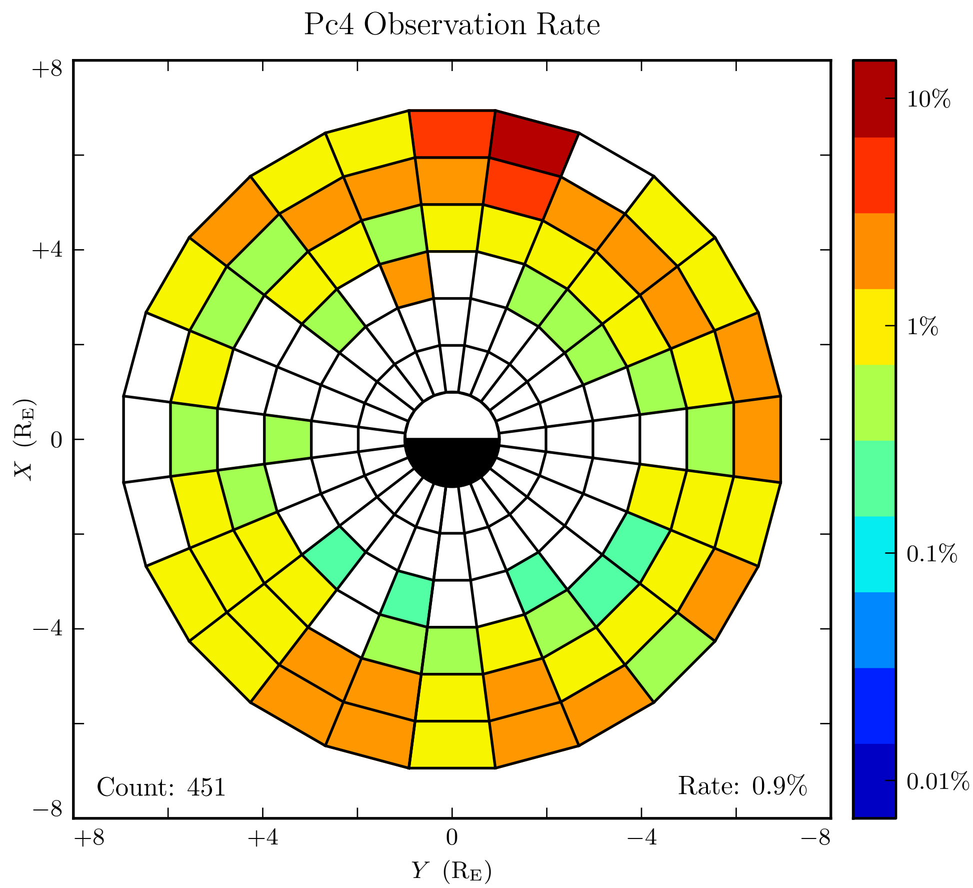

Figure 8.3: The above figure shows the spatial distribution of all 762 observed Pc4 events. Counts are normalized by the amount of usable data in each bin. The value in the bottom-right corner is the mean of the rate in each bin, with the rate in each bin weighed by the area of that bin. Events where the poloidal and toroidal channel both trigger (∼10 % of events) are counted as only a single event. Bins shown in white contain zero events.

side. Notably, Dai et al focused on even poloidal waves. While they did not explicitly remove odd events from the sample, they did introduce a threshold in the magnetic field. This threshold is preferrentially satisfied by even waves (which have a magnetic field antinode near the equator) compared to odd waves (which have a magnetic field node). Dai et al characterized the parity of only a quarter of his events; among those, they found even harmonics to outnumber odd harmonics ten-to-one.

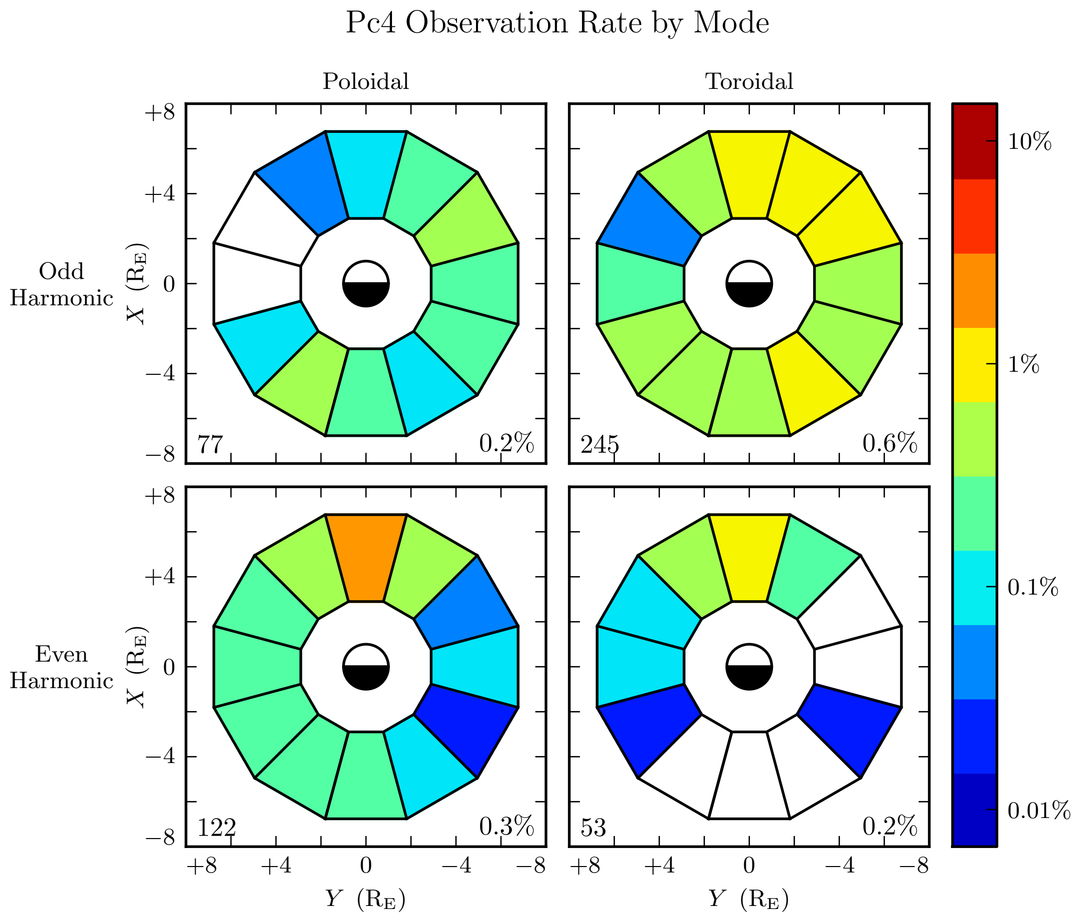

Figure 8.4: The above figure shows the spatial distribution for the same 762 events shown in Figure 8.3, partitioned by polarization and parity. The selection criteria described in Section 8.1 ensure that both properties are known for all events. Event counts are normalized by the time spent by the amount of usable data in each bin. Counts shown in the bottom-left corners do not sum to 762 because some events trigger on both the poloidal channel and the toroidal channel.

In fact — to the degree that they can be straightforwardly compared — the distributions in **??** also show agreement with work by Anderson et al[2] (using AMPTE/CCE), Kokubun et al[52] (using ATS6), Liu et al[56] (using THEMIS), and Motoba at al[68] (using GOES). Toroidal events dominate overall, and are primarily seen on the morning side. Poloidal events are spread broadly in MLT, with a peak near noon and odd harmonics in the early morning.

Crucially, the present work can offer insight into how previous results fit together. Unlike events considered in previous works, those shown in **??** have all been categorized in terms of both polarization and parity. And, crucially, the selection process has not introduced a bias with respect to polarization or parity (at least not an obvious one).

The even events shown in Figure 8.4 show good agreement with the numerical results in Chapter 7. The even poloidal and even toroidal distributions are qualitatively similar, as might be expected if even poloidal waves served as a source for even toroidal waves. Even poloidal waves are more prevalent, suggesting a typical event duration comparable to the poloidal-to-toroidal rotation timescale. And even toroidal events are skewed dayward compared to even poloidal events, suggesting that poloidal-to-toroidal rotation is inhibited by increased Joule dissipation on the nightside.

The same can be said to some extent for the odd events in Figure 8.4, though the trends are less strong. Odd poloidal and odd toroidal events are both scarce on the dusk flank. On the dawn flank, poloidal events skew nightward, while toroidal events are spread broadly — that is, they are skewed dayward compared to the poloidal events. However, it's unclear why odd toroidal events outnumber odd poloidal events to such a degree.

When the 762 events are broken down by mode in Figure 8.4, the result is 124 odd poloidal events, 214 even poloidal events, 415 odd toroidal events, and 83 even toroidal events — a total of 836 events. The total is greater than 762 because in $\sim$10 % of events, the poloidal and toroidal channels trigger independently. Such cases are marked as a single event in Figure 8.3, but the toroidal and poloidal events are both shown in Figure 8.4.

Double-triggering can be taken as a crude proxy for event quality. When the channels both trigger independently, the two events almost always (71 of 74 events) exhibit the same parity. This suggests a poloidal wave with suffient power, and a sufficient narrow spectral peak, that it can still be seen after much of its energy has rotated to the toroidal mode.

The spatial distribution of double events is shown in **??**. The left column shows events observed with DST $\geq -30\,\mathrm{nT}$, normalized by the amount of usable data at DST $\geq -30\,\mathrm{nT}$. The right column shows events at DST $< -30\,\mathrm{nT}$, normalized by the amount of data with DST $< -30\,\mathrm{nT}$.

Odd double-triggering events are spread broadly in MLT. They rarely occur twice on the same day; the 23 events shown take place over 20 different dates. Odd double events occur at similar rates regardless of DST.

Even-harmonic double-triggering events, on the other hand, are mostly seen near noon, and are significantly more common during geomagnetically active times. Even events are also more concentrated than odd ones. The 48 even-harmonic double-events shown in the bottom row of **??** are spread over 20 days, and 35 of them are spread over just 7 days. This clustering — where the poloidal and toroidal channel both trigger for five to ten half-hour events in the same day — is prevalent regardless of DST.

8.3 Events by Amplitude

One might reasonable be concerned that the spatial distributions presented in **??** are dominated by these small events, while Pc4 events large enough to be noteworthy follow a different distribution entirely.

The distribution of event magnitudes is presented in Figure 8.5, graded based on the peak of the Gaussian fit of each event's Poynting flux, $|\widetilde{S}(\omega)\,|$. Mean and median values are listed for each mode. Most events are small, with Poynting flux well below $0.1\,\mathrm{mW/m^2}$ when mapped to the ionosphere. Only a handful of events — 3 out of 762 — exceed $1\,\mathrm{mW/m^2}$.

Perhaps the most notable feature of Figure 8.5 is the relative uniformity of the distribution of even poloidal events. If a higher magnitude threshold is imposed, as shown in Figure 8.6, the proportion of even poloidal events rises.

The spatial bins in Figure 8.6 are larger than those in Section 8.2; this change reflects an effort to keep the number of events large compared to the number of bins, even when

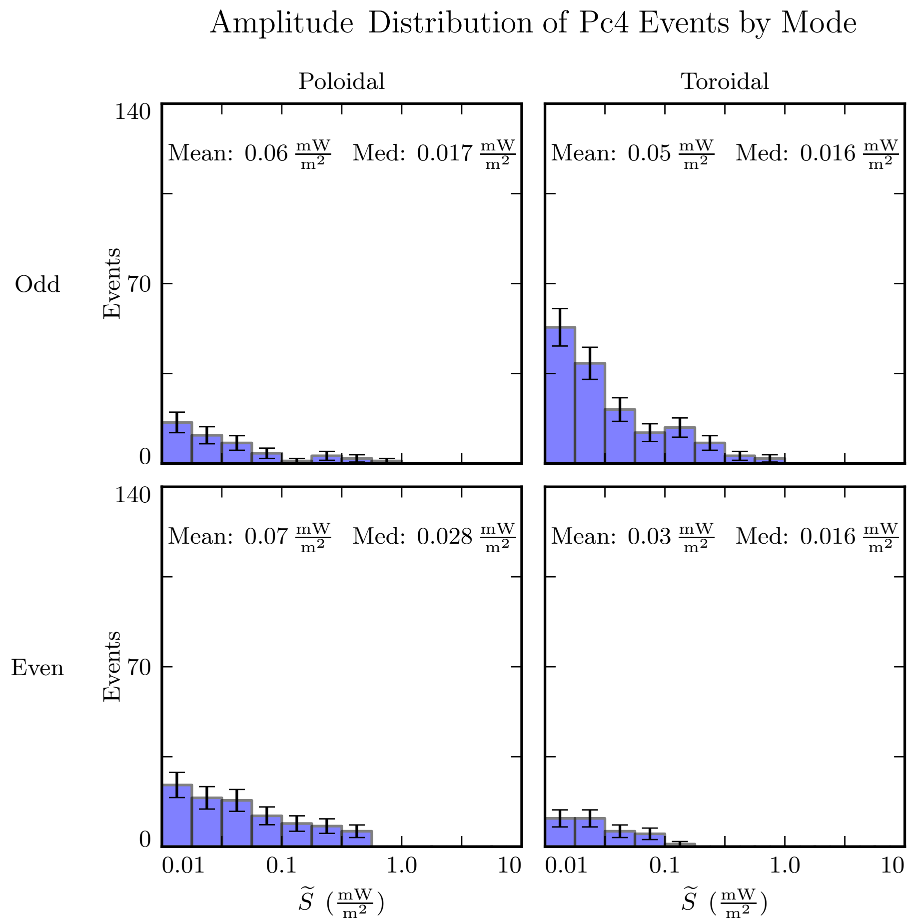

Figure 8.5: Amplitude distribution is shown for Pc4 events by parity and polarization, based on the peak of the spectrum's Gaussian fit. Odd poloidal events, odd toroidal events, and even toroidal events fall off sharply with increasing amplitude, while the even poloidal events are distributed more broadly — the mean and median of the even poloidal distribution are twice as large as those of the others.

considering relatively small subsets of the data. The larger bins — two hours wide in MLT and divided at $L = 5$ radially — are also used in Sections 8.4 and 8.5. All of the large-binned bullseye plots also share a common logarithmic color bar.

All else being equal, one might expect the amplitude distribution of even toroidal events to mimic that of even poloidal events, since poloidal waves asymptotically rotate to toroidal waves. However, this does not seem to be the case. The mean and median magnitudes are more or less consistent for even toroidal events, odd toroidal events, and odd poloidal events, while even poloidal events are twice as large by those metrics. This would seem to imply that large even poloidal modes have disproportionately high modenumbers, and thus deliver energy to the toroidal mode less efficiently. This explanation is unsatisfying, however; Figure 8.6 shows that even poloidal and toroidal modes both become more concentrated near noon at high amplitude, suggesting a common origin.

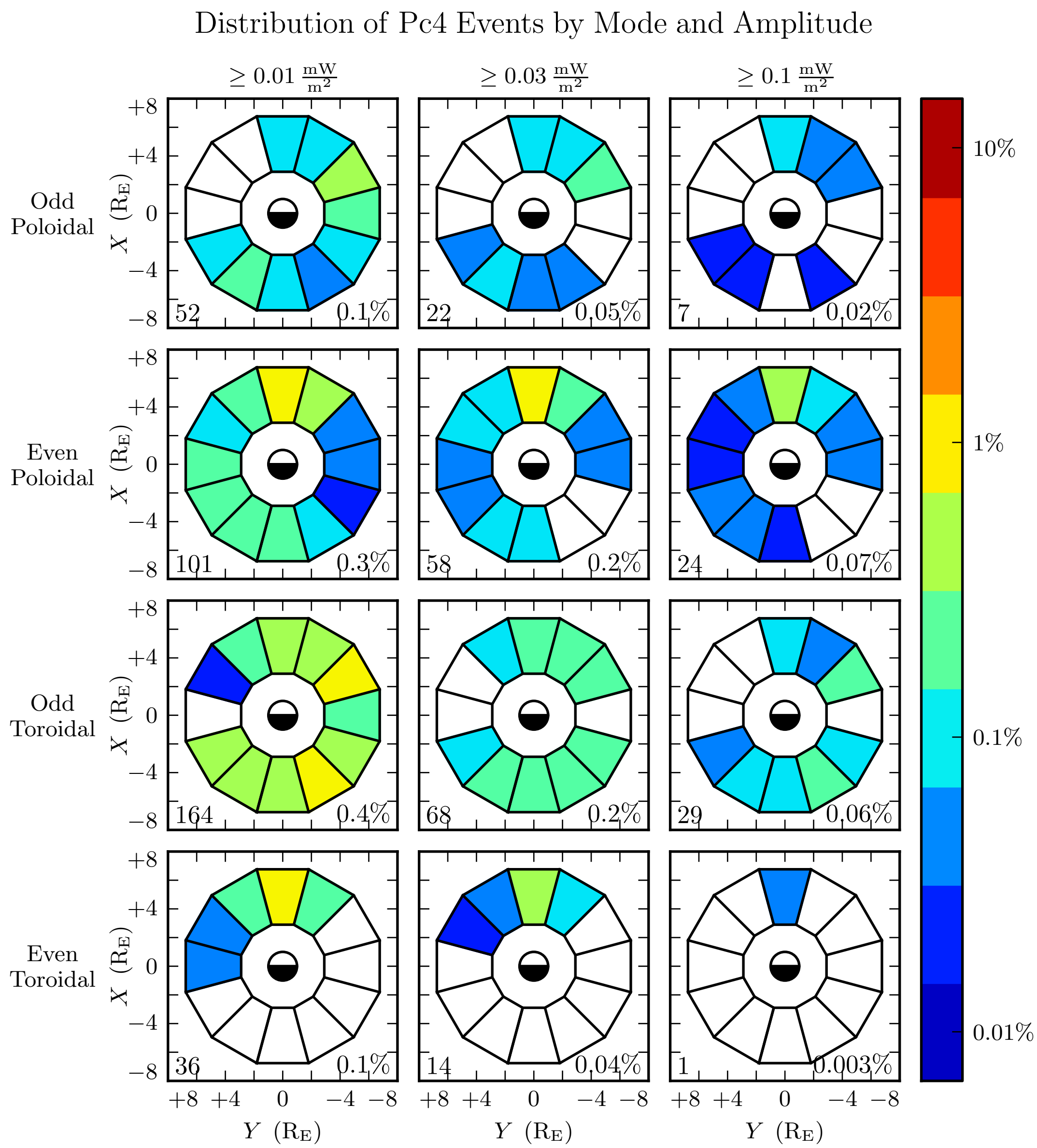

Figure 8.6: The above figure shows the distribution of Pc4 event observations by mode. Event magnitude cutoff is constant down each column, and increases from left to right. Stronger even events appear to become more concentrated on the dayside as the amplitude increases. Even poloidal events also become significantly more numerous relative to the other three modes, from 26 % at a cutoff of $0.01\,\mathrm{mW/m^2}$ to 41 % above $0.1\,\mathrm{mW/m^2}$.

8.4 Events by Frequency

The difference in magnetospheric conditions between the dayside and the nightside suggest that different eigenfrequencies should arise between dayside and nightside resonances at the same L-shell. In fact, this phenomenon has been observed directly; the frequencies of azimuthally-drifting FLRs have been shown to change over time[68]. The effect is attributed to the difference in mass loading (and thus Alfvén speed) as a function of MLT.

This effect was furthermore apparent in the numerical results shown in Chapter 7, where Alfvén speeds on the dayside (based on empirical profiles) gave rise to significantly higher eigenfrequencies than those on the nightside.

In Figure 8.7, events at 11 mHz to 17 mHz (center column) do seem to be shifted nightward compared to those at 7 mHz to 11 mHz (left column), but the effect is far less pronounced than what is suggested by Sections 7.2 and 7.3.

As might be expected, even events are more prevalent than (mostly fundamental) odd events higher in the Pc4 range. Events at 7 mHz to 11 mHz (left column) outnumber those at 17 mHz to 25 mHz (right column) ten-to-one or more for odd events. Among even events, the comparison is more like three-to-one.

The spatial distribution of odd toroidal events above 17 mHz warrants specific consideration. Whereas odd toroidal events overall show an overwhelming preference for the morning side, those at the top of the Pc4 frequency band instead appear from noon to dusk. It's possible that this distribution is a consequence of the small number of events (25). More likely, however, is that these are third-harmonic events, and that their source more closely resembles the source for second-harmonic waves than it does first harmonics.

The frequency distribution for each mode is shown in Figure 8.8. The most distinctive feature, certainly, is the frequency peak in the odd toroidal mode near 9 mHz. This is in line with the idea that toroidal waves exhibit frequencies that depend sharply on L, as discussed in Chapter 7. While the Van Allen Probes' orbits do cover a large range of

L-shells, their observations (and thus the selected events) are concentrated near apogee at $L \sim 6$.

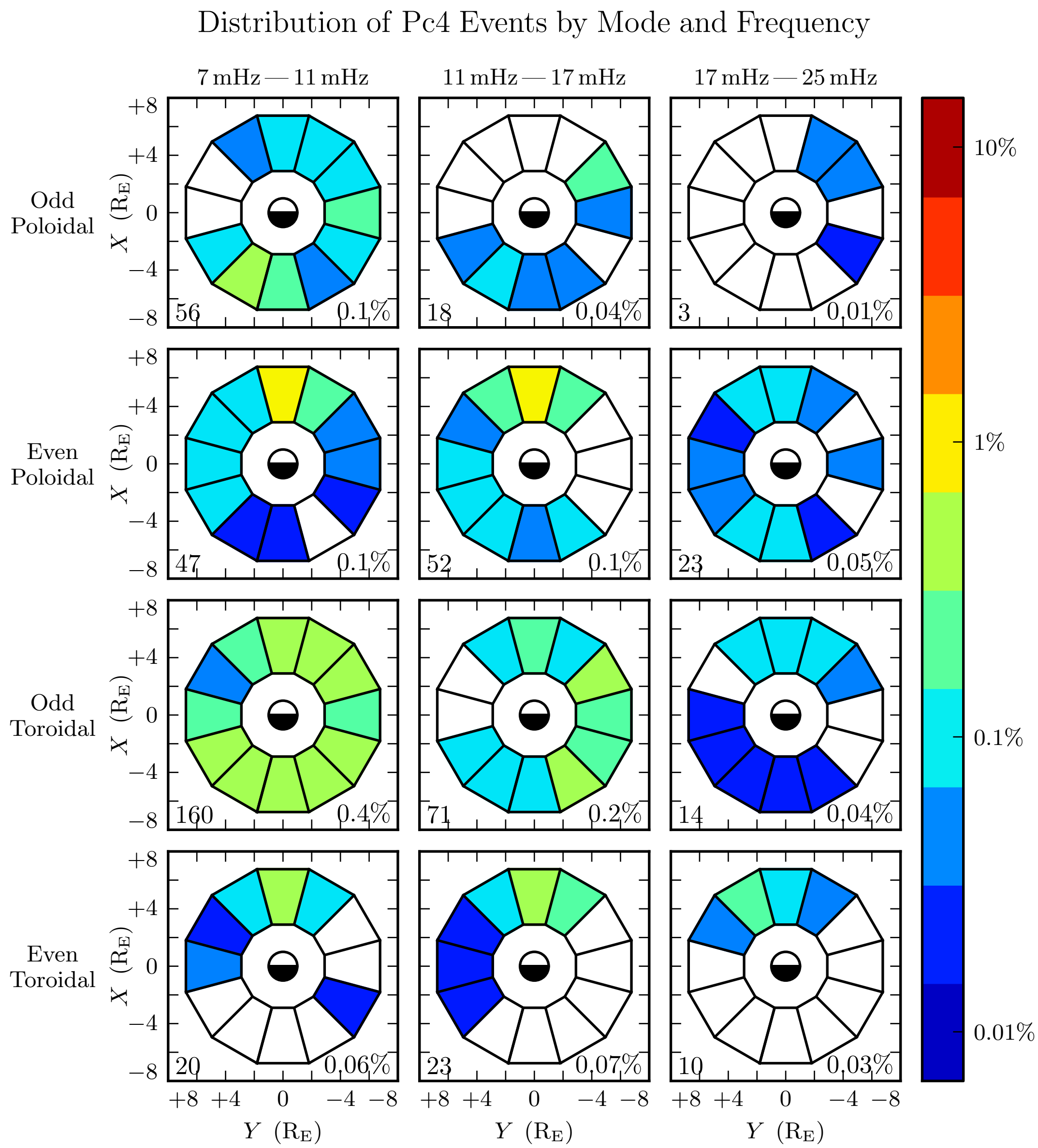

Figure 8.7: Event distributions above are shown in terms of mode (row) as well as event frequency (column). Mid-frequency Pc4 events are shifted somewhat nightward compared to low-frequency Pc4 events, as might be expected from the dayside's faster Alfvén speed. At the top of the Pc4 band, the distribution of odd toroidal events takes on a decidedly different character; this is likely because these events are third harmonics rather than first harmonics.

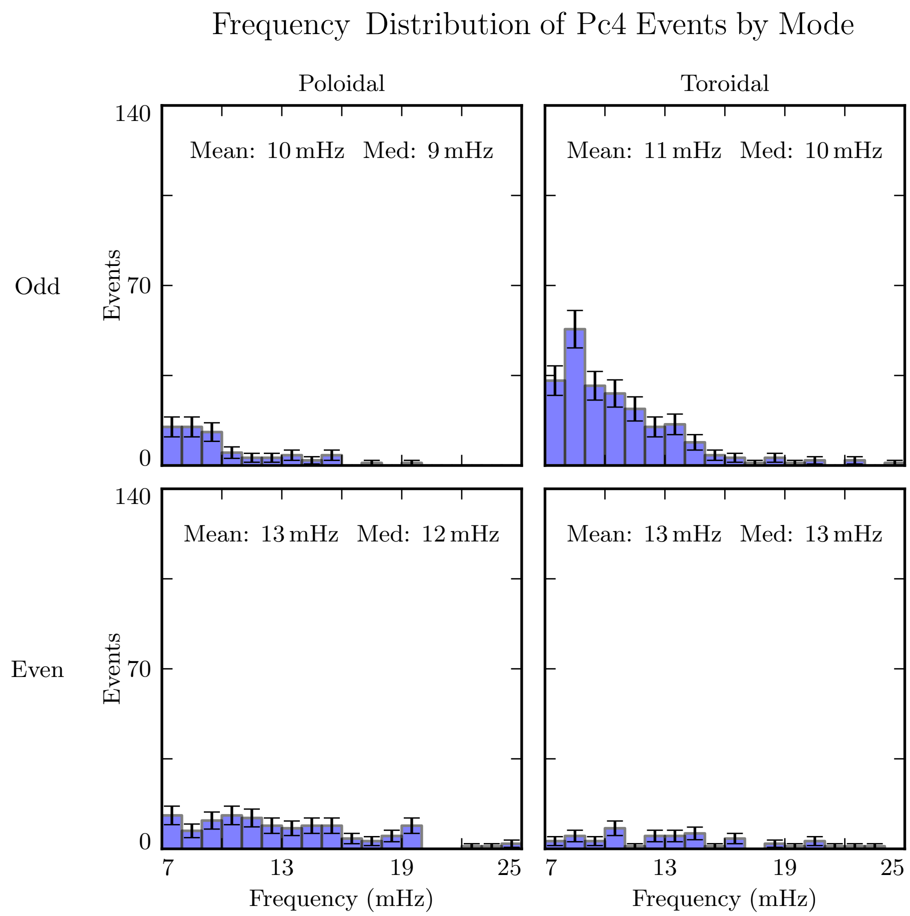

Figure 8.8: Frequency distributions are shown for all events, divided by harmonic and polarization. Odd toroidal events exhibit a particularly sharp peak in frequency, which is consistent with the toroidal mode's strong correlation with the local eigenfrequency. Poloidal modes appear more spread out in frequency, which is also consistent with past observations and with the numerical results in Chapter 7.

8.5 Events by Phase

The phase of a wave — that is, the phase offset between a wave's electric and magnetic fields — indicates how its energy is partitioned between the standing and traveling wave modes. An ideal standing wave has a phase of $\pm 90°$, and thus its Poynting flux is completely imaginary. A traveling wave, on the other hand, has electric and magnetic fields in phase (or in antiphase), and is associated with a net movement of energy, usually toward the ionosphere.

Wave phase is a topic of significant interest, since it allows an estimate to be made of the wave's lifetime. And, because phase can only be determined using simultaneous electric and magnetic field measurements, it has only recently become observable.

The energy per unit volume, and the rate at which energy is carried out of that volume by Poynting flux, are respectively given by:

$$U = \frac{R^3}{2\mu_0} B^2 \qquad\qquad \frac{\partial}{\partial t} U = \frac{R^2}{\mu_0} EB \cos\varphi \tag{8.2}$$

Where B, E, and R are the characteristic magnetic field magnitude, electric field magnitude, and length scale. The phase, $\varphi \equiv \arctan \frac{\mathbb{I}\mathrm{m}\widetilde{S}}{\mathbb{R}\mathrm{e}\widetilde{S}}$, enters because only real Poynting flux carries energy.

The ratio of the two quantities in Equation (8.2) gives a characteristic timescale over which energy leaves the system

$$\tau \equiv \frac{BR}{2E\cos\varphi} \tag{8.3}$$

In the present case, magnetic fields are on the order of $1\,\mathrm{nT}$ and electric fields are on the order of $1\,\mathrm{mV/m}$. A reasonable scale length might be $10^4\,\mathrm{km}$, the distance traversed by the probe over the course of a half-hour event near apogee (notably, back-to-back events are unusual).

At a phase of $80°$, this timescale is comparable to a Pc4 wave period. At $135°$, where energy is divided evenly between the standing and traveling wave, the timescale is just

7 seconds. A wave with a phase so far from 90° would quickly vanish unless it were constantly being replenished.

An example of just such an event is shown in Figure 8.9. The left column shows electric and magnetic field waveforms in blue and red respectively. The right shows the corresponding spectra: imaginary Poynting flux in magenta (corrresponding to the strength of the standing wave) and real Poynting flux in green (for the traveling wave). The black line is a Gaussian fit to the magnitude of the Poynting flux.

The poloidal channel shows a mostly-standing wave, with a phase of 79°. The coherent activity in the compressional magnetic field implies a low azimuthal modenumber, and thus a fast rotation of energy from the poloidal mode to the toroidal mode. It's likely the rotation of energy from the poloidal mode contributes significantly to the toroidal mode's lifetime; the toroidal wave's phase is 130°, so its energy should be carried away quickly by Poynting flux.

The selection process described in Section 8.1 does not explicitly consider phase. However, the discrete Fourier transform is performed over a half-hour time span. An event with a comparatively short lifetime would be unlikely to register. It's unsurprising to see the events in Figure 8.10 are tightly clustered near 90°.

It's further notable in Figure 8.10 that the odd events are more spread out in phase than the even events. Near the equator, odd modes have an electric field antinode and a magnetic field node; per Equation (8.3), an odd mode's lifetime should be longer than that of an even mode with the same phase.

Unlike amplitude (Section 8.3) and frequency (Section 8.4), events of different phase do not seem to exhibit different spatial distributions, as shown in Figure 8.11. Comparisons are limited by the small event counts in several of the subplots; however, coarsely speaking, events with phases of 75° and worse (left column) show spatial distributions more or less in proportion with events phased 85° or better (right column). Figure 8.10 uses the absolute value of each event's phase, as does Figure 8.11.

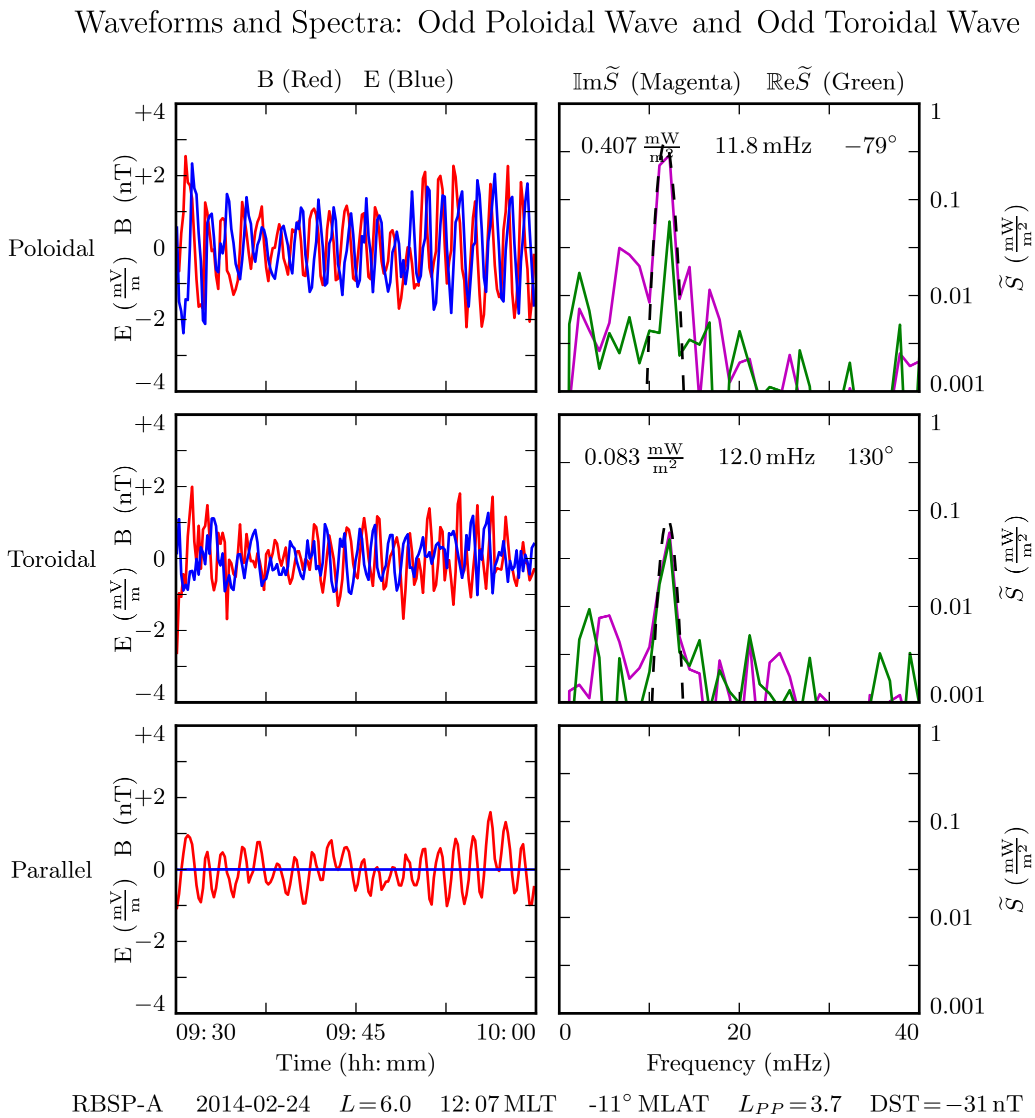

Figure 8.9: The above is a double event, where the poloidal and toroidal channels have been independently selected as events. The poloidal channel shows a wave with most of its energy in the standing wave (phase of 79°). The toroidal mode has a significant traveling component (phase of 130°). The compressional activity implies a low modenumber, which would cause energy to rotate quickly from the poloidal mode to the toroidal mode — evidently at a sufficient rate to replenish the losses due to the traveling mode's real Poynting flux.

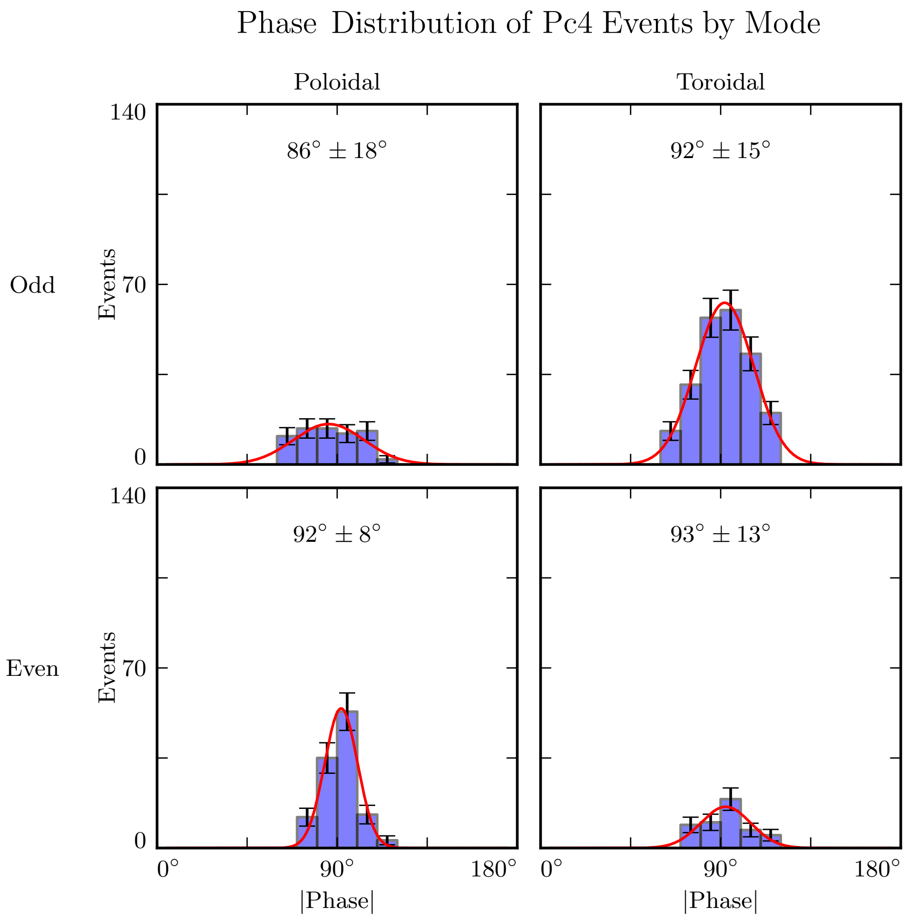

Figure 8.10: The (absolute) phase of the selected Pc4 events is shown above. All modes show phase distributions peaked around 90°. This reflects the fact that a significant traveling wave component quickly carries energy away from an FLR. Odd events are spread more broadly in phase than even events. This is consistent with the odd modes' electric field antinode near the equator, where events are observed; the characteristic loss timescale depends on $\frac{B}{E}$ per Equation (8.3).

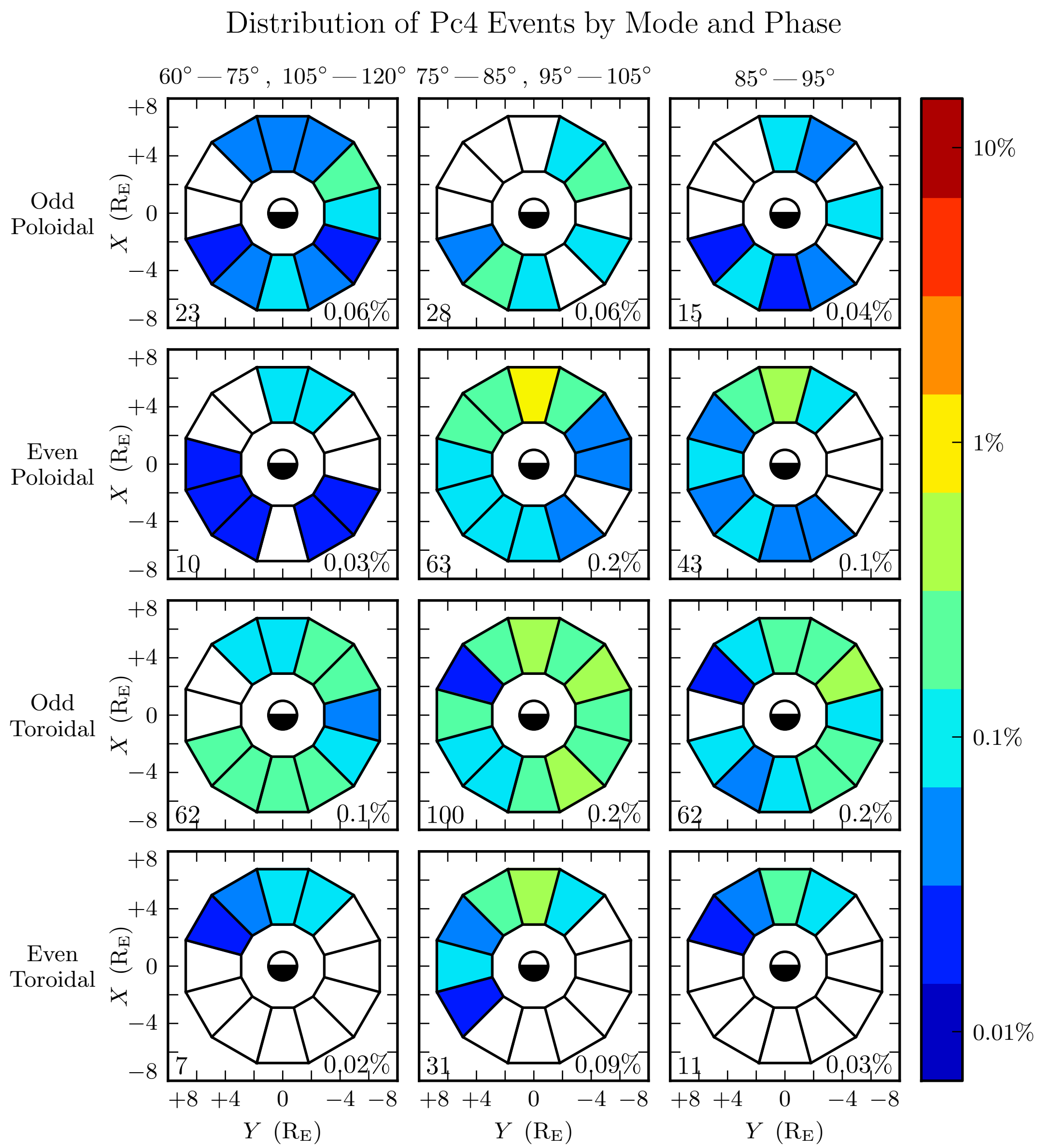

Figure 8.11: The observation rate of events is shown above, divided by (absolute) phase as well as mode. The closer a phase to 90°, the more of an event's energy is in the standing wave, rather than the traveling wave. The spatial distribution of events is more or less consistent between waves with phases very close to 90° and those with a significant traveling wave component.

8.6 Discussion

The present chapter gives a survey of ∼800 thirty-minute Pc4 events, each characterized in terms of both parity and polarization, and selected in a way that does not introduce an apparent bias in either property. No past study has so thoroughly disentangled the parity and polarization of these waves.

Coarsely speaking, event distributions are found to be consistent with past surveys. Toroidal events dominate overall, and are primarily seen on the morning side. Poloidal events are spread broadly in MLT, with a peak near noon and distinctive odd harmonics in the early morning. From there, the simultaneous consideration of harmonic and polarization, combined with the numerical results from Chapter 7, offers significant insight.

The near-noon peak of poloidal Pc4 events is shown to be due to even events (a majority subset). Odd poloidal events occur preferrentially near midnight and across the morning side. Similarly, toroidal events are mostly odd, and it is specifically the odd toroidal events which occur on the morningside, while even toroidal events peak near noon.

The spatial distribution of even poloidal events looks much like the spatial distribution of even toroidal events, except that the toroidal distribution is skewed dayward compared to the poloidal. The same can be said of the odd events. This is consistent (per Chapter 7) with poloidal events as an effective source for (same-parity) toroidal events on the dayside, and a less-effective source on the nightside.

Curiously, only a small minority (17 %) of toroidal events are found to be odd, while a majority (63 %) of poloidal events are even. This disparity may offer clues to the source of these waves.

All events are found to follow a similar amplitude distribution, except for even poloidal events, which are notably larger. The cause is unclear.

The ∼6 % of odd toroidal Pc4s at the top of the frequency range (17 mHz to 25 mHz) are found to exhibit a qualitatively different spatial distribution from the rest. It's likely that these waves are third harmonics, and that their excitation mechanism more closely resembles that of second harmonics than it does first harmonics.

Event phase is also considered. Most events of both polarizations are shown to have absolute phase in the range 80° to 100°, indicating that the traveling component of Pc4 pulsations is small compared to the standing component. Odd events are found to be spread more broadly in phase; this is likely a consequence of being measured near the equator, where (due to the electric field antinode) the lifetime of an odd event is significantly larger than that of an even event with the same phase.

Chapter 9

Conclusion

TODO: $\cdots$

9.1 Code Development

9.2 Numerical Work

9.3 Van Allen Probe Pc4 Survey

References

[1] H. Alfvén. On the cosmogony of the solar system III. *Stockholms Observatoriums Annaler*, 14:9.1–9.29, 1946.

[2] B. J. Anderson, M. J. Engebretson, S. P. Rounds, L. J. Zanetti, and T. A. Potemra. A statistical study of Pc 3-5 pulsations observed by the AMPTE/CCE magnetic fields experiment, 1. occurrence distributions. *J. Geophys. Res.*, 95(A7):10495, 1990.

[3] V. Angelopoulos. The THEMIS mission. *Space Science Reviews*, 141(1-4):5–34, 2008.

[4] C. W. Arthur and R. L. McPherron. The statistical character of Pc 4 magnetic pulsations at synchronous orbit. *J. Geophys. Res.*, 86(A3):1325, 1981.

[5] K. Birkeland. Expédition norvégienne de 1899-1900 pour l'étude des aurores boréales. *Mat. Naturvidensk. Kl.*, KI(I), 1901.

[6] J. P. Boris. A physically motivated solution of the Alfvén problem. *NRL Memorandum Report*, 2167, 1970.

[7] A. Brekke, T. Feder, and S. Berger. Pc4 giant pulsations recorded in Tromsø, 1929-1985. *Journal of Atmospheric and Terrestrial Physics*, 49(10):1027–1032, 1987.

[8] C. W. Carlson, R. F. Pfaff, and J. G. Watzin. The fast auroral SnapshoT (FAST) mission. *Geophys. Res. Lett.*, 25(12):2013–2016, 1998.

[9] A. A. Chan, M. Xia, and L. Chen. Anisotropic alfvén-ballooning modes in Earth's magnetosphere. *J. Geophys. Res. Space Physics*, 99(A9):17351–17366, 1994.

[10] L. Chen and A. Hasegawa. A theory of long-period magnetic pulsations: 1. steady state excitation of field line resonance. *J. Geophys. Res.*, 79(7):1024–1032, 1974.

[11] L. Chen and A. Hasegawa. Kinetic theory of geomagnetic pulsations: 1. internal excitations by energetic particles. *J. Geophys. Res.*, 96(A2):1503, 1991.

[12] C. Z. Cheng and Q. Qian. Theory of ballooning-mirror instabilities for anisotropic pressure plasmas in the magnetosphere. *J. Geophys. Res.*, 99(A6):11193, 1994.

[13] G. Chisham and D. Orr. Statistical studies of giant pulsations (pgs): Harmonic mode. *Planetary and Space Science*, 39(7):999–1006, 1991.

[14] W. D. Cummings, R. J. O'Sullivan, and P. J. Coleman. Standing Alfvén waves in the magnetosphere. *J. Geophys. Res.*, 74(3):778–793, 1969.

[15] L. Dai. Collisionless magnetic reconnection via Alfvén eigenmodes. *Phys. Rev. Lett.*, 102(24), 2009.

[16] L. Dai, K. Takahashi, R. Lysak, C. Wang, J. R. Wygant, C. Kletzing, J. Bonnell, C. A. Cattell, C. W. Smith, R. J. MacDowall, S. Thaller, A. Breneman, X. Tang, X. Tao, and L. Chen. Storm time occurrence and spatial distribution of Pc4 poloidal ULF waves in the inner magnetosphere: A Van Allen Probes statistical study. *J. Geophys. Res. Space Physics*, 120:4748–4762, 2015.

[17] L. Dai, K. Takahashi, J. R. Wygant, L. Chen, J. Bonnell, C. A. Cattell, S. Thaller, C. Kletzing, C. W. Smith, R. J. MacDowall, D. N. Baker, J. B. Blake, J. Fennell, S. Claudepierre, H. O. Funsten, G. D. Reeves, and H. E. Spence. Excitation of poloidal standing Alfvén waves through drift resonance wave-particle interaction. *Geophys. Res. Lett.*, 40:4127–4132, 2013.

[18] A. W. Degeling, R. Rankin, and Q.-G. Zong. Modeling radiation belt electron acceleration by ULF fast mode waves, launched by solar wind dynamic pressure fluctuations. *J. Geophys. Res. Space Physics*, 119(11):8916–8928, 2014.

[19] W. D. D'haeseleer, W. N. G. H. J. D. Callen, and J. L. Shohet. *Flux Coordinates and Magnetic Field Structure*. Springer-Verlag, New York, 1991.

[20] J. W. Dungey. The attenuation of Alfvén waves. *J. Geophys. Res.*, 59(3):323–328, 1954.

[21] J. W. Dungey. Interplanetary magnetic field and the auroral zones. *Phys. Rev. Lett.*, 6(2):47–48, 1961.

[22] A. Einstein. Die grundlage der allgemeinen relativitätstheorie. *Ann. Phys.*, 354:769–822, 1916.

[23] S. R. Elkington, M. K. Hudson, and A. A. Chan. Acceleration of relativistic electrons via drift-resonant interaction with toroidal-mode Pc-5 ULF oscillations. *Geophys. Res. Lett.*, 26(21):3273–3276, 1999.

[24] M. J. Engebretson, D. L. Murr, K. N. Erickson, R. J. Strangeway, D. M. Klumpar, S. A. Fuselier, L. J. Zanetti, and T. A. Potemra. The spatial extent of radial magnetic pulsation events observed in the dayside near synchronous orbit. *J. Geophys. Res.*, 97(A9):13741, 1992.

[25] M. J. Engebretson, L. J. Zanetti, T. A. Potemra, and M. H. Acuna. Harmonically structured ulf pulsations observed by the ampte cce magnetic field experiment. *Geophysical Research Letters*, 13(9):905–908, 1986.

[26] M. J. Engebretson, L. J. Zanetti, T. A. Potemra, D. M. Klumpar, R. J. Strangeway, and M. H. Acuña. Observations of intense ULF pulsation activity near the geomagnetic equator during quiet times. *J. Geophys. Res.*, 93(A11):12795, 1988.

[27] S. Fujita and T. Tamao. Duct propagation of hydromagnetic waves in the upper ionosphere, 1, electromagnetic field disturbances in high latitudes associated with localized incidence of a shear Alfvén wave. *J. Geophys. Res.*, 93(A12):14665, 1988.

[28] K.-H. Glassmeier. Magnetometer array observations of a giant pulsation event. *J. Geophys.*, 48:127–138, 1980.

[29] K.-H. Glassmeier. On the influence of ionospheres with non-uniform conductivity distribution on hydromagnetic waves. *J. Geophys.*, 54(2):125–137, 1984.

[30] K.-H. Glassmeier, S. Buchert, U. Motschmann, A. Korth, and A. Pedersen. Concerning the generation of geomagnetic giant pulsations by drift-bounce resonance ring current instabilities. *Ann. Geophysicae*, 17:338–350, 1999.

[31] C. Goertz. Kinetic alfvén waves on auroral field lines. *Planetary and Space Science*, 32(11):1387–1392, 1984.

[32] C. K. Goertz and R. W. Boswell. Magnetosphere-ionosphere coupling. *J. Geophys. Res.*, 84(A12):7239, 1979.

[33] J. Goldstein. Plasmasphere response: Tutorial and review of recent imaging results. *Space Science Reviews*, 124(1-4):203–216, 2006.

[34] C. A. Green. Giant pulsations in the plasmasphere. *Planetary and Space Science*, 33(10):1155–1168, 1985.

[35] J. L. Green and S. Boardsen. Duration and extent of the great auroral storm of 1859. *Advances in Space Research*, 38(2):130–135, 2006.

[36] C. Greifinger and P. S. Greifinger. Theory of hydromagnetic propagation in the ionospheric waveguide. *J. Geophys. Res.*, 73(23):7473–7490, 1968.

[37] B. C. Hall. *Lie Groups, Lie Algebras, and Representations.* Graduate Texts in Mathematics. Springer, New York, second edition, 2015.

[38] Y. X. Hao, Q.-G. Zong, Y. F. Wang, X.-Z. Zhou, H. Zhang, S. Y. Fu, Z. Y. Pu, H. E. Spence, J. B. Blake, J. Bonnell, J. R. Wygant, and C. A. Kletzing. Interactions of energetic electrons with ULF waves triggered by interplanetary shock: Van allen probes observations in the magnetotail. *J. Geophys. Res. Space Physics*, 119(10):8262–8273, 2014.

[39] L. Harang. *Pulsations in the terrestrial magnetic records at high latitude stations.* Grondahl, 1942.

[40] O. Hillebrand, J. Muench, and R. L. McPherron. Ground-satellite correlative study of a giant pulsation event. *Journal of Geophysics Zeitschrift Geophysik*, 51:129–140, 1982.

[41] W. J. Hughes. Magnetospheric ULF waves: A tutorial with a historical perspective. In M. J. Engebretson, K. Takahashi, and M. Scholer, editors, *Solar Wind Sources of Magnetospheric Ultra-Low-Frequency Waves*, volume 81 of *Geophys. Monogr.*, pages 1–12. American Geophysical Union, Washington, DC, 1994.

[42] W. J. Hughes and D. J. Southwood. The screening of micropulsation signals by the atmosphere and ionosphere. *J. Geophys. Res.*, 81(19):3234–3240, 1976.

[43] W. J. Hughes, D. J. Southwood, B. Mauk, R. L. McPherron, and J. N. Barfield. Alfvén waves generated by an inverted plasma energy distribution. *Nature*, 275(5675):43–45, 1978.

[44] J. A. Jacobs, Y. Kato, S. Matsushita, and V. A. Troitskaya. Classification of geomagnetic micropulsations. *J. Geophys. Res.*, 69(1):180–181, 1964.

[45] T. Karlsson and G. T. Marklund. A statistical study of intense low-altitude electric fields observed by freja. *Geophys. Res. Lett.*, 23(9):1005–1008, 1996.

[46] Y. Kato and T. Tsutomu. Hydromagnetic oscillations in a conducting medium with hall couduct-ivity under the uniform magnetic field. *Science reports of the Tohoku University. Ser. 5, Geophysics*, 7(3):147–164, 1956.

[47] M. C. Kelley. *The Earth's Ionosphere*. Academic Press, San Diego, second edition, 1989.

[48] R. L. Kessel. Solar wind excitation of pc5 fluctuations in the magnetosphere and on the ground. *J. Geophys. Res.*, 113(A4), 2008.

[49] D. Y. Klimushkin, P. N. Mager, and K.-H. Glassmeier. Toroidal and poloidal Alfvén waves with arbitrary azimuthal wavenumbers in a finite pressure plasma in the earth's magnetosphere. *Annales Geophysicae*, 22(1):267–287, 2004.

[50] S. Knight. Parallel electric fields. *Planetary and Space Science*, 21:741–750, 1973.

[51] S. Kokubun. Observations of Pc pulsations in the magnetosphere: Satellite-ground correlation. *J. Geomagn. Geoelec*, 32(Supplement2):SII17–SII39, 1980.

[52] S. Kokubun, K. N. Erickson, T. A. Fritz, and R. L. McPherron. Local time asymmetry of Pc 4-5 pulsations and associated particle modulations at synchronous orbit. *J. Geophys. Res.*, 94(A6):6607–6625, 1989.

[53] D.-H. Lee and K. Kim. Compressional MHD waves in the magnetosphere: A new approach. *J. Geophys. Res.*, 104(A6):12379–12385, 1999.

[54] A. S. Leonovich and V. A. Mazur. Structure of magnetosonic eigenoscillations of an axisymmetric magnetosphere. *J. Geophys. Res.*, 105(A12):27707–27715, 2000.

[55] W. Liu, J. B. Cao, X. Li, T. E. Sarris, Q.-G. Zong, M. Hartinger, K. Takahashi, H. Zhang, Q. Q. Shi, and V. Angelopoulos. Poloidal ULF wave observed in the plasmasphere boundary layer. *J. Geophys. Res. Space Physics*, 118(7):4298–4307, 2013.

[56] W. Liu, T. E. Sarris, X. Li, S. R. Elkington, R. Ergun, V. Angelopoulos, J. Bonnell, and K. H. Glassmeier. Electric and magnetic field observations of Pc4 and Pc5 pulsations in the inner magnetosphere: A statistical study. *J. Geophys. Res.*, 114(A12), 2009.

[57] W. Liu, T. E. Sarris, X. Li, Q.-G. Zong, R. Ergun, V. Angelopoulos, and K. H. Glassmeier. Spatial structure and temporal evolution of a dayside poloidal ULF wave event. *Geophys. Res. Lett.*, 38(19), 2011.

[58] R. L. Lysak. Magnetosphere-ionosphere coupling by Alfvén waves at midlatitudes. *J. Geophys. Res.*, 109, 2004.

[59] R. L. Lysak and D. hun Lee. Response of the dipole magnetosphere to pressure pulses. *Geophys. Res. Lett.*, 19(9):937–940, 1992.

[60] R. L. Lysak and Y. Song. A three-dimensional model of the propagation of Alfvén waves through the auroral ionosphere: first results. *Adv. Space Res.*, 28:813–822, 2001.

[61] R. L. Lysak, C. L. Waters, and M. D. Sciffer. Modeling of the ionospheric Alfvén resonator in dipolar geometry. *J. Geophys. Res. Space Physics*, 118, 2013.

[62] P. N. Mager and D. Y. Klimushkin. Giant pulsations as modes of a transverse Alfvénic resonator on the plasmapause. *Earth, Planets and Space*, 65(5):397–409, 2013.

[63] I. R. Mann, E. A. Lee, S. G. Claudepierre, J. F. Fennell, A. Degeling, I. J. Rae, D. N. Baker, G. D. Reeves, H. E. Spence, L. G. Ozeke, R. Rankin, D. K. Milling, A. Kale, R. H. W. Friedel, and F. Honary. Discovery of the action of a geophysical synchrotron in the Earth's Van Allen radiation belts. *Nature Communications*, 4, 2013.

[64] I. R. Mann and A. N. Wright. Finite lifetimes of ideal poloidal Alfvén waves. *J. Geophys. Res.*, 100:23677–23686, 1995.

[65] I. R. Mann, A. N. Wright, and A. W. Hood. Multiple-timescales analysis of ideal poloidal Alfvén waves. *J. Geophys. Res.*, 102(A2):2381–2390, 1997.

[66] T. Maynard, N. Smith, S. Gonzalez, et al. Solar storm risk to the North American electric grid. 2013.

[67] R. L. McPherron. The role of substorms in the generation of magnetic storms. *Washington DC American Geophysical Union Geophysical Monograph Series*, 98:131–147, 1997.

[68] T. Motoba, K. Takahashi, J. V. Rodriguez, and C. T. Russell. Giant pulsations on the afternoonside: Geostationary satellite and ground observations. *J. Geophys. Res. Space Physics*, 120:8350–8367, 2015.

[69] NASA. Coordinated data analysis (workshop) web.

[70] NASA. Near miss: The solar superstorm of july 2012.

[71] M. Nicolet. The collision frequency of electrons in the ionosphere. *Journal of Atmospheric and Terrestrial Physics*, 3(4):200–211, 1953.

[72] L. G. Ozeke and I. R. Mann. Energization of radiation belt electrons by ring current ion driven ULF waves. *J. Geophys. Res.*, 113(A2), 2008.

[73] E. M. Poulter, W. Allan, E. Nielsen, and K.-H. Glassmeier. Stare radar observations of a PG pulsation. *J. Geophys. Res.*, 88(A7):5668, 1983.

[74] J. A. Proehl, W. Lotko, I. Kouznetsov, and S. D. Geimer. Ultralow-frequency magnetohydrodynamics in boundary-constrained geomagnetic flux coordinates. *J. Geophys. Res.*, 107(A9):1225, 2002.

[75] H. R. Radoski. A note on oscillating field lines. *J. Geophys. Res.*, 72(1), 1967.

[76] H. R. Radoski. A theory of latitude dependent geomagnetic micropulsations: The asymptotic fields. *J. Geophys. Res.*, 79, 1974.

[77] R. Rankin, J. C. Samson, and V. T. Tikhonchuk. Parallel electric fields in dispersive shear alfvén waves in the dipolar magnetosphere. *Geophys. Res. Lett.*, 26(24):3601–3604, 1999.

[78] B. Rolf. Giant micropulsations at abisko. *J. Geophys. Res.*, 36(1):9, 1931.

[79] G. Rostoker, H.-L. Lam, and J. V. Olson. PC 4 giant pulsations in the morning sector. *J. Geophys. Res.*, 84(A9):5153, 1979.

[80] J. C. Samson, L. L. Cogger, and Q. Pao. Observations of field line resonances, auroral arcs, and auroral vortex structures. *J. Geophys. Res.*, 101(A8):17373–17383, 1996.

[81] H. J. Singer, W. J. Hughes, and C. T. Russell. Standing hydromagnetic waves observed by ISEE 1 and 2: Radial extent and harmonic. *J. Geophys. Res.*, 87(A5):3519, 1982.

[82] D. J. Southwood. Some features of field line resonances in the magnetosphere. *Planetary and Space Science*, 22(3):483–491, 1974.

[83] D. J. Southwood. A general approach to low-frequency instability in the ring current plasma. *J. Geophys. Res.*, 81(19):3340–3348, 1976.

[84] J. Stratton and N. J. Fox. Radiation belt storm probes (RBSP) mission overview. In *2012 IEEE Aerospace Conference*. Institute of Electrical & Electronics Engineers (IEEE), 2012.

[85] E. Sucksdorff. Giant pulsations recorded at sodankyl during 19141938. *Terrestrial Magnetism and Atmospheric Electricity*, 44(2):157–170, 1939.

[86] K. Takahashi, J. Bonnell, K.-H. Glassmeier, V. Angelopoulos, H. J. Singer, P. J. Chi, R. E. Denton, Y. Nishimura, D.-H. Lee, M. Nosé, and W. Liu. Multipoint observation of fast mode waves trapped in the dayside plasmasphere. *J. Geophys. Res.*, 115(A12), 2010.

[87] K. Takahashi, K.-H. Glassmeier, V. Angelopoulos, J. Bonnell, Y. Nishimura, H. J. Singer, and C. T. Russell. Multisatellite observations of a giant pulsation event. *J. Geophys. Res.*, 116:A11223, 2011.

[88] K. Takahashi, M. D. Hartinger, V. Angelopoulos, K.-H. Glassmeier, and H. J. Singer. Multispacecraft observations of fundamental poloidal waves without ground magnetic signatures. *J. Geophys. Res. Space Physics*, 118:4319–4334, 2013.

[89] K. Takahashi, R. W. McEntire, A. T. Y. Lui, and T. A. Potemra. Ion flux oscillations associated with a radially polarized transverse Pc 5 magnetic pulsation. *J. Geophys. Res.*, 95(A4):3717, 1990.

[90] K. Takahashi and R. L. McPherron. Standing hydromagnetic oscillations in the magnetosphere. *Planetary and Space Science*, 32:1343–1359, 1984.

[91] K. Takahashi, N. Sato, J. Warnecke, H. Ĺuhr, H. E. Spence, and Y. Tonegawa. On the standing wave mode of giant pulsations. *J. Geophys. Res. Space Physics*, 97(A7):10717–10732, 1992.

[92] B. J. Thompson and R. L. Lysak. Electron acceleration by inertial alfvén waves. *J. Geophys. Res.*, 101(A3):5359–5369, 1996.

[93] V. T. Tikhonchuk and R. Rankin. Electron kinetic effects in standing shear alfvén waves in the dipolar magnetosphere. *Physics of Plasmas*, 7(6):2630, 2000.

[94] B. T. Tsurutani, W. D. Gonzalez, G. S. Lakhina, and S. Alex. The extreme magnetic storm of 12 september 1859. *Journal of Geophysical Research: Space Physics*, 108(A7), 2003. 1268.

[95] A. Y. Ukhorskiy. Impact of toroidal ULF waves on the outer radiation belt electrons. *J. Geophys. Res.*, 110(A10), 2005.

[96] J. A. Wanliss and K. M. Showalter. High-resolution global storm index: Dst versus sym-h. *Journal of Geophysical Research: Space Physics*, 111(A2):n/a–n/a, 2006. A02202.

[97] C. L. Waters, R. L. Lysak, and M. D. Sciffer. On the coupling of fast and shear Alfvén wave modes by the ionospheric Hall conductance. *Earth Planets Space*, 65:385–396, 2013.

[98] C. L. Waters and M. D. Sciffer. Field line resonant frequencies and ionospheric conductance: Results from a 2-d MHD model. *J. Geophys. Res.*, 113(A5), 2008.

[99] D. M. Wright and T. K. Yeoman. High-latitude HF doppler observations of ULF waves: 2. waves with small spatial scale sizes. *Ann. Geophys.*, 17(7):868–876, 1999.

[100] J. R. Wygant, J. W. Bonnell, K. Goetz, R. E. Ergun, F. S. Mozer, S. D. Bale, M. Ludlam, P. Turin, P. R. Harvey, R. Hochmann, K. Harps, G. Dalton, J. McCauley, W. Rachelson, D. Gordon, B. Donakowski, C. Shultz, C. Smith, M. Diaz-Aguado, J. Fischer, S. Heavner, P. Berg, D. M. Malsapina, M. K. Bolton, M. Hudson, R. J. Strangeway, D. N. Baker, X. Li, J. Albert, J. C. Foster, C. C. Chaston, I. Mann, E. Donovan, C. M. Cully, C. A. Cattell, V. Krasnoselskikh, K. Kersten, A. Brenneman, and J. B. Tao. The electric field and waves instruments on the radiation belt storm probes mission. *Space Science Reviews*, 179(1):183–220, 2013.

[101] J. R. Wygant, A. Keiling, C. A. Cattell, R. L. Lysak, M. Temerin, F. S. Mozer, C. A. Kletzing, J. D. Scudder, V. Streltsov, W. Lotko, and C. T. Russell. Evidence for kinetic alfvn waves and parallel electron energization at 46 re altitudes in the plasma sheet boundary layer. *Journal of Geophysical Research: Space Physics*, 107(A8):SMP 24–1–SMP 24–15, 2002.

[102] K. Yee. Numerical solution of initial boundary value problems involving maxwell's equations in isotropic media. *IEEE Trans. Antennas Propagat.*, 14(3), 1966.

[103] T. K. Yeoman and D. M. Wright. ULF waves with drift resonance and drift-bounce resonance energy sources as observed in artificially-induced HF radar backscatter. *Ann. Geophys.*, 19(2):159–170, 2001.

[104] Q.-G. Zong, X.-Z. Zhou, X. Li, P. Song, S. Y. Fu, D. N. Baker, Z. Y. Pu, T. A. Fritz, P. Daly, A. Balogh, and H. Réme. Ultralow frequency modulation of energetic particles in the dayside magnetosphere. *Geophys. Res. Lett.*, 34(12), 2007.

[105] Q.-G. Zong, X.-Z. Zhou, Y. F. Wang, X. Li, P. Song, D. N. Baker, T. A. Fritz, P. W. Daly, M. Dunlop, and A. Pedersen. Energetic electron response to ULF waves induced by interplanetary shocks in the outer radiation belt. *J. Geophys. Res.*, 114(A10), 2009.